



저작자표시-비영리-변경금지 2.0 대한민국

이용자는 아래의 조건을 따르는 경우에 한하여 자유롭게

- 이 저작물을 복제, 배포, 전송, 전시, 공연 및 방송할 수 있습니다.

다음과 같은 조건을 따라야 합니다:



저작자표시. 귀하는 원저작자를 표시하여야 합니다.



비영리. 귀하는 이 저작물을 영리 목적으로 이용할 수 없습니다.



변경금지. 귀하는 이 저작물을 개작, 변형 또는 가공할 수 없습니다.

- 귀하는, 이 저작물의 재이용이나 배포의 경우, 이 저작물에 적용된 이용허락조건을 명확하게 나타내어야 합니다.
- 저작권자로부터 별도의 허가를 받으면 이러한 조건들은 적용되지 않습니다.

저작권법에 따른 이용자의 권리는 위의 내용에 의하여 영향을 받지 않습니다.

이것은 [이용허락규약\(Legal Code\)](#)을 이해하기 쉽게 요약한 것입니다.

[Disclaimer](#)

이학박사 학위논문

**Discovery of bioactive small molecules
for metabolic diseases *via* phenotype-
based approach**

표현형 기반 접근법을 통한
생리활성 저분자 화합물의 발굴 및 이를 이용한
대사성질환에 관한 연구

2017년 8월

서울대학교 대학원

화학부

조아라

**Discovery of bioactive small molecules for
metabolic diseases via phenotype-based approach**

지도교수 박 승 범

이 논문을 조아라의 박사학위논문으로 제출함

2017 년 6 월

서울대학교 대학원

화학부

조 아 라

조아라의 박사학위 논문을 인준함

2017 년 6 월

위 원 장	이 남 기	(인)
부 위 원 장	박 승 범	(인)
위 원	김 병 문	(인)
위 원	김 재 범	(인)
위 원	이 준 석	(인)

Abstract

Discovery of bioactive small molecules for metabolic diseases *via* phenotype-based approach

Ala Jo

Department of Chemistry
College of Life Sciences
Seoul National University

Phenotype-based approach in drug discovery has emerged as a promising approach to discover new bioactive small molecules. Unlike the conventional target-based approach that selects specific target protein based on an understanding of the molecular mechanism about pathogenesis of certain disease, the phenotype-based approach focuses on phenotypic changes in cells or organisms as a final outcome of perturbation in interconnected multiple pathways. Compared with the target-based approach, the main strength of the phenotype-based approach is that it has a high potential for discovering new therapeutic target that its biological role in managing disease is unrevealed. In this context, the phenotype-based approach is most powerful when applied to disease in which the therapeutic target is not thoroughly defined.

In this study, I describe the systematic studies to discover bioactive small molecules for metabolic diseases *via* phenotype-based approach.

In **chapter 2**, I discuss the construction of phenotypic screening for monitoring cellular glucose uptake to discover bioactive small molecules for hyperglycemia and Type 2 Diabetes Mellitus (T2DM). In this chapter, I explored the biophysical properties of the fluorescence glucose bioprobe, GB2-Cy3. Based on the understanding of biophysical properties of GB2-Cy3, I developed the first image-based high-throughput screening (HTS) system to monitor the glucose uptake in living cells with robustness and accuracy. From the screening of compound library in living cells, I could successfully discover the new glucose uptake enhancers has anti-diabetic potential. In addition, I investigated an impact of molecular charge of fluorescence glucose bioprobes on their GLUT-specific cellular uptake. I synthesized charge derivatives of GB2-Cy3, and demonstrated that zwitterionic and anionic charge diminish GLUT-specificity of fluorescent glucose bioprobes. In conclusion, I demonstrated the superiority of GB2-Cy3 as a GLUT-specific fluorescent glucose bioprobe. Moreover, I validated the *in vivo* applicability of GB2-Cy3 in zebra fish larvae *in vivo* system. This *in vivo* imaging system of GB2-Cy3 will be an important method to validate the therapeutic potential of glucose uptake enhancers in the anti-diabetic drug discovery process.

In **chapter 3**, I describe an approach using fluorescence imaging for monitoring dynamic GLUT4 translocation in living cells. I developed a novel imaging system, EGFP-GLUT4-SNAP, based on genetically encoded SNAP tag and EGFP into GLUT4. EGFP-GLUT4-SNAP is a novel imaging system for monitoring GLUT4 trafficking in a real-time and quantitative manner. This novel approach enables the determination of the quantity and kinetics of GLUT4 translocation to the PM. Using this novel GLUT4 monitoring system, I could reveal the insulin action on the regulation of intracellular distribution of GLUT4. I anticipate that this approach allows us to understand the mechanism of GLUT4 regulation, and to study mechanism-of-action of chemical compounds which increase cellular glucose uptake by regulating GLUT4 trafficking.

In **chapter 4**, discovery of novel anti-obesity small molecule, named as SB1501, *via* phenotype-based approach is described. I performed image-based phenotypic screening by monitoring cellular lipid droplets using fluorescent lipid droplets bioprobe, SF44. From the screening of small molecule library, I discovered SB1501 that reduces cellular lipid droplets in adipocytes. Mode-of-action study of SB1501 revealed that SB1501 decreases lipid droplets by inducing PGC-1 α regulatory cellular processes involving mitochondrial biogenesis, fatty acid oxidation (FAO) and adaptive thermogenesis in 3T3-L1 adipocytes. Moreover, SB1501 showed *in vivo* efficacy by reducing the size of adipocytes in adipose tissue, the

body weight and the fat mass in *db/db* mice. In addition, administration of SB1501 ameliorated insulin resistance. Taken together, novel small molecule, SB1501, has therapeutic potential for combating obesity and obesity-associated insulin resistance. In conclusion, I suggest the utility of image-based phenotype-based approach for discovering novel anti-obesity agents.

In summary, this study is consisted of 1) exploration of fluorescence bioprobe for monitoring the cellular phenotype such as cellular glucose uptake and lipid droplet organelles, 2) construction of image-based phenotypic screening system using fluorescence bioprobe, 3) discovery of bioactive compounds *via* practical HTS, and 4) following mechanism-of-action study of bioactive compounds. Based on these studies, I suggest that phenotype-based approach is a promising approach to discover novel bioactive small molecules. In the present study, it is of major interest to discover new bioactive small molecules for metabolic disease, because a crucial therapeutic target of metabolic diseases has not been thoroughly understood. Although this dissertation focus on the metabolic disease, I anticipate that this approach will shed light on the diseases in which the therapeutic target is not thoroughly defined.

Key words: chemical biology, phenotype-based approach, high-throughput screening, high-content screening, fluorescent bioprobe, fluorescence microscopy imaging, target identification, metabolic syndrome, hyperglycemia, type 2 diabetes mellitus, obesity

Student number: 2011-20305

Table of contents

Abstract	i
Table of contents	vi
List of figures	viii
Chapter 1. Introduction	1
1.1. Phenotype-based approach in drug discovery	1
1.2. Metabolic syndrome	4
1.3. Glucose transporter 4	6
1.4. Purpose	8
1.5. References	10
Chapter 2. Construction of image-based high-throughput screening to discover novel glucose uptake enhancers	12
2.1. Introduction	12
2.2. Material and methods	16
2.3. Results and discussion	25
2.3.1. Exploiting the mechanism of cellular uptake of the fluorescent glucose bioprobe, GB2-Cy3	25
2.3.2. Impact of molecular charge on GLUT-specific cellular uptake	32
2.3.3. Construction of image-based high-throughput screening	39
2.3.4. <i>In vivo</i> application of GB2-Cy3 in zebrafish larvae	47
2.4. Conclusion	53
2.5. References	55

Chapter 3. Development of novel real-time assay system for monitoring dynamic GLUT4 trafficking in living cells	58
3.1. Introduction	58
3.2. Materials and methods	61
3.3. Results and discussion	67
3.4. Conclusion	89
3.5. References	92
Chapter 4. Discovery of anti-obesity small molecule via monitoring cellular lipid droplets	94
4.1. Introduction	94
4.2. Materials and methods	96
4.3. Results and discussion	102
4.4. Conclusion	123
4.5. References	124
Conclusion	127
Abstract in Korean	131
Appendix	135

List of figures

- Figure 1.1 Schematic diagrams of approaches in drug discovery.
- Figure 1.2 General process of image-based phenotypic screening to identify novel hits and lead compounds from small molecule compound library.
- Figure 1.3 Risk factors for the occurrence of metabolic syndrome.
- Figure 1.4 Schematic diagram of dynamic GLUT4 trafficking.
- Figure 2.1 (A) Structure of 2-NBDG. (B) Structure of GB2-Cy3.
- Figure 2.2 (A) Structure of L-GB2-Cy3. (B) Glucose competition assay with GB2-Cy3 and L-GB2-Cy3 in C2C12 myoblast cell line.
- Figure 2.3 Suppression of endocytosis and its influence on GB2-Cy3/L-GB2-Cy3 cellular uptake.
- Figure 2.4 Schematic diagram of the physiological behavior of D-glucose and GB2-Cy3.
- Figure 2.5 (A) Time-dependent signal loss of GB2-Cy3 within the cytoplasm of C2C12 myoblasts. (B) Continuous monitoring of the time-dependent signal in living C2C12 myoblasts upon treatment with DNP.
- Figure 2.6 Schematic of the physiological behavior of GB2-Cy3 in the presence or absence of phloretin, with its chemical structure.

- Figure 2.7 (A) Fluorescence microscopic images of cells obtained after washing with cold PBS in the presence and absence of phloretin. (B) Fluorescence intensities were determined from the ROI and the data are the average values obtained in measurements performed on 40–50 cells.
- Figure 2.8 (A) Chemical structure of GB2-Cy3, GB2-Cy3-S1, and GB2-Cy3-S2. (B) Molecular charge calculation and surface charge area modeling of three glucose bioprobes using Marvin sketch 6.1.6.
- Figure 2.9 (A) Fluorescence emission spectra and (B) absolute quantum yields of GB2-Cy3, GB2-Cy3-S1, and GB2-Cy3-S2 in methanol and water.
- Figure 2.10 (A) Fluorescence microscopic images after cellular uptake of GB2-Cy3, GB2-Cy3-S1, and GB2-Cy3-S2 in HeLa cells. (B) Dose-dependent cellular uptake of GB2-Cy3-S1 and GB2-Cy3-S2. (C) Glucose competition assay with GB2-Cy3, and GB2-Cy3-S1 with 55 mM D-glucose.
- Figure 2.11 Chemical structures of the previously reported glucose bioprobes and their molecular charges and biophysical properties. Cellular uptake of neutral and cationic charged glucose bioprobes are GLUT-specific as previously reported, but that of anionic and zwitterionic charged glucose bioprobes are not.
- Figure 2.12 Effect of phloretin on the quantitative analysis of cellular fluorescence intensity in the high-throughput screening system.
- Figure 2.13 Continuous monitoring of GB2-Cy3 fluorescence intensity within the cytoplasm in the presence and absence of phloretin.

- Figure 2.14 Linearity between the two independent assays in the presence or absence of phloretin.
- Figure 2.15 Screening protocol for image-based HTS using GB2-Cy3 to monitor cellular glucose uptake.
- Figure 2.16 Comparison of GB2-Cy3 and 6-NBDG with our image-based HTS assay system.
- Figure 2.17 (A) Chemical structure of primary hit compounds. (B) Fluorescence images of C2C12 myoblasts. (C) Cell viability test of primary hit compounds in C2C12 myoblasts.
- Figure 2.18 (A) RFU was determined from the ROI. C2C12 myoblasts were treated with DMSO and 4 of the primary hits, P33A04, P33D04, P33F06 and P33G07 for 24 h. (B) Radioisotope-based measurement of ¹⁴C-labeled 2-DG uptake. (C) Commercial enzyme-based measurement of cellular glucose uptake using non-radiolabeled 2-DG.
- Figure 2.19 Time dependent uptake of GB2-Cy3 in zebrafish.
- Figure 2.20 Dose dependent uptake of 2-NBDG and GB2-Cy3 in zebrafish.
- Figure 2.21 (A) Glucose competition assay of GB2-Cy3 in zebrafish. (B) Fluorescence intensities of zebrafish larval eyes. (C) GB2-Cy3 uptake was deteriorated by the GLUT inhibitor, 4,6-EDG (4,6-*O*-ethylidene- α -D-glucose), in zebrafish. (D) Fluorescence intensities of GB2-Cy3 uptake into the zebrafish larval eye.
- Figure 2.22 (A) GB2-Cy3 uptake increases in zebrafish after treatment with glucose uptake enhancers, ampknone and rosiglitazone. (B) GB2-Cy3 uptake quantification of lysed

larvae using a plate reader. (C) GB2-Cy3 uptake quantification by measuring fluorescence intensities of the zebrafish larval eye.

- Figure 2.23 Glucose uptake enhancers (insulin, GAPDS and emodin) increased GB2- Cy3 uptake in zebrafish.
- Figure 3.1 Schematic diagram of EGFP-GLUT4-SNAP.
- Figure 3.2 (A) In-gel fluorescence analysis of EGFP-GLUT4-SNAP expressing cells after labeling with SNAP tag probes. (B) Structures of membrane-impermeable SNAP tag probes.
- Figure 3.3 Live cell fluorescence imaging of EGFP-GLUT4-SNAP expressing cells after labeling with SNAP tag probes.
- Figure 3.4 Quantitative monitoring of GLUT4 translocation to the PM.
- Figure 3.5 (A) Relative fluorescence intensities of cell images from EGFP channel. (B) Relative fluoresce intensities of cell images from Cy5 channel. (C) Calculated relative Cy5/EGFP fluorescence intensities.
- Figure 3.6 Real-time imaging of GLUT4 translocation in live cells.
- Figure 3.7 (A) Calculated TRITC/EGFP fluorescence intensities from cell images from TRITC channel (*Figure 3.6B*) and EGFP channel. (B) Fluorescence intensities at each time point.
- Figure 3.8 Models of Insulin-stimulated GLUT4 translocation (ISGT).

- Figure 3.9 Insulin actions on the control of intracellular distribution of GLUT4. Time-lapse fluorescence images after stimulated with insulin or not.
- Figure 3.10 Immunofluorescence imaging of SNAP tag-labeled GLUT4 with early endosome marker (EEA-1).
- Figure 3.11 High-content screening (HCS) platform with EGFP-GLUT4-SNAP.
- Figure 3.12 (A) Representative images of single vesicle detection in basal or insulin-stimulated cells. (B) Time-dependent increase in number of SNAP tag- labeled GLUT4 versus total number of GLUT4. (C),(D) Intracellular distribution of SNAP tag-labeled GLUT4 between perinuclear region, cytosol and plasma membrane over time.
- Figure 3.13 Effect of rosiglitazone co-treatment on intracellular GLUT4 distribution.
- Figure 3.14 (A) Quantification of GLUT4 translocation to the PM by determining the number of SNAP tag-labeled GLUT4 versus total number of GLUT4. (B) Number of SNAP tag-labeled GLUT4 which are localized in near the PM versus total number of GLUT4. (C) Number of SNAP tag-labeled GLUT4 which are localized in perinuclear region versus total number of GLUT4. (D) Intracellular distribution of SNAP tag-labeled GLUT4 between perinuclear region (PeriNuc), cytosol, and plasma membrane (PM).
- Figure 4.1 Schematic diagram of image-based phenotypic screening to discover bioactive small molecule via monitoring cellular lipid droplets.

- Figure 4.2 Discovery novel bioactive compound SB1501 through lipid droplet monitoring HCS.
- Figure 4.3 (a) Experiment design to investigate the bioactivity of SB1501 in differentiated 3T3-L1 adipocytes. (b) After treatment of SB1501 during the 3T3-L1 differentiation, cells are stained with SF44 to visualize lipid droplets.
- Figure 4.4 (a) Distribution of the size of each single lipid droplets after the treatment with SB1501 for 8 days. (b) Mean fluorescence intensities of cells stained with SF44 after treatment of SB1051 for 8 days. (c) Quantification of triglyceride (TG) concentration after cell lysis and extraction of TG from 3T3- L1 adipocytes.
- Figure 4.5 Effects of SB1501 treatment in 3T3-L1 adipocytes.
- Figure 4.6 Quantitative real-time PCR analysis after dose dependent treatment of SB1501 for 8 days.
- Figure 4.7 Quantitative real-time PCR analysis of adipokine mRNA level after dose dependent treatment of SB1501 for 8 days.
- Figure 4.8 SB1501 improves metabolic profiles in *db/db* mice. (a),(b) Body weight changes of *db/db* mice for 4 weeks. SB1501 (10 mpk)- injected mice showed drastic weight decrease compared with vehicle- and rosiglitazone (15 mpk)- injected mice. (c) Weight of IWAT after 4 weeks of administration of vehicle, SB1501 and rosiglitazone. (d) Weight of BAT after 4 weeks of administration of vehicle, SB1501 and rosiglitazone. (e) Daily food intake data.
- Figure 4.9 Glucose tolerance tests (GTTs) after the administration of SB1501 for 4 weeks. SB1501 L (10 mpk), SB1501 H (20 mpk) and rosiglitazone (15 mpk). Area under curves of GTTs data is also presented.
- Figure 4.10 H&E staining of IWAT and BAT after the administration of SB1501 for 4 weeks.

- Figure 4.11 Immunofluorescent imaging of PGC-1 α and UCP1 in IWAT and BAT.
- Figure 4.12 Quantitative real-time PCR analysis of gene involved in browning of WAT, mitochondria biogenesis and fatty acid oxidation processes in IWAT and BAT.
- Figure 4.13 Target identification of SB1501 with TS-FITGE technology.

Chapter 1. Introduction

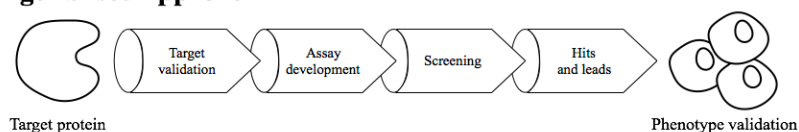
1.1. Phenotype-based approach in drug discovery

There are two types of approaches in drug discovery. One is target-based approach and the other is phenotype-based approach (Figure 1.1). The target-based approach selects specific target protein based on an understanding of the molecular mechanism about pathogenesis of disease. Generally, the target-based approach uses *in vitro* enzymatic assay to discover bioactive small molecules that directly modulate the function of the target protein. The success of the target-based approach depends on a clear understanding of the biological function of the target protein. However, it is usually not easy to clearly understand the function of certain protein within complex protein network [1]. For this reason, it is difficult to estimate the physiological behavior and downstream effects of bioactive small molecules in a cellular system. This limitation is frequently the reason for the failure of drug candidates derived from target-based approaches because of their off-target effects [2].

Therefore, the pharmaceutical community has been developing an alternative approach using a phenotypic screening system to overcome the limited understanding of complex protein network [3, 4]. Unlike the target-based approach using *in vitro* enzymatic assay systems, the phenotype-based approach identifies bioactive small molecules based on the

phenotypic changes in living cells or organisms as a final outcome of perturbation in interconnected signal pathways. Therefore, physiological behavior and biological activity of hit compounds can be evaluated at the early stage of drug discovery.

Target-based approach



Phenotype-based approach

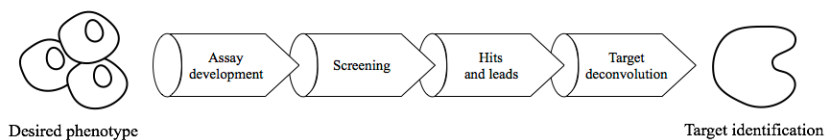


Figure 1.1. Schematic diagrams of approaches in drug discovery.

Recent advances in imaging technology ensure the image-based high-throughput screening of a large number of small molecules with multiple fluorescence channels [5-9]. By introducing fluorescent probes that can visualize cellular phenotypes, a lot of phenotypic information can be extracted from a single experiment, and this information is analyzed to evaluate the bioactivity of small molecules (Figure 1.2). Therefore, fluorescence image-based phenotypic screening has emerged as an

effective method for discovering new bioactive small molecules in the field of drug discovery.

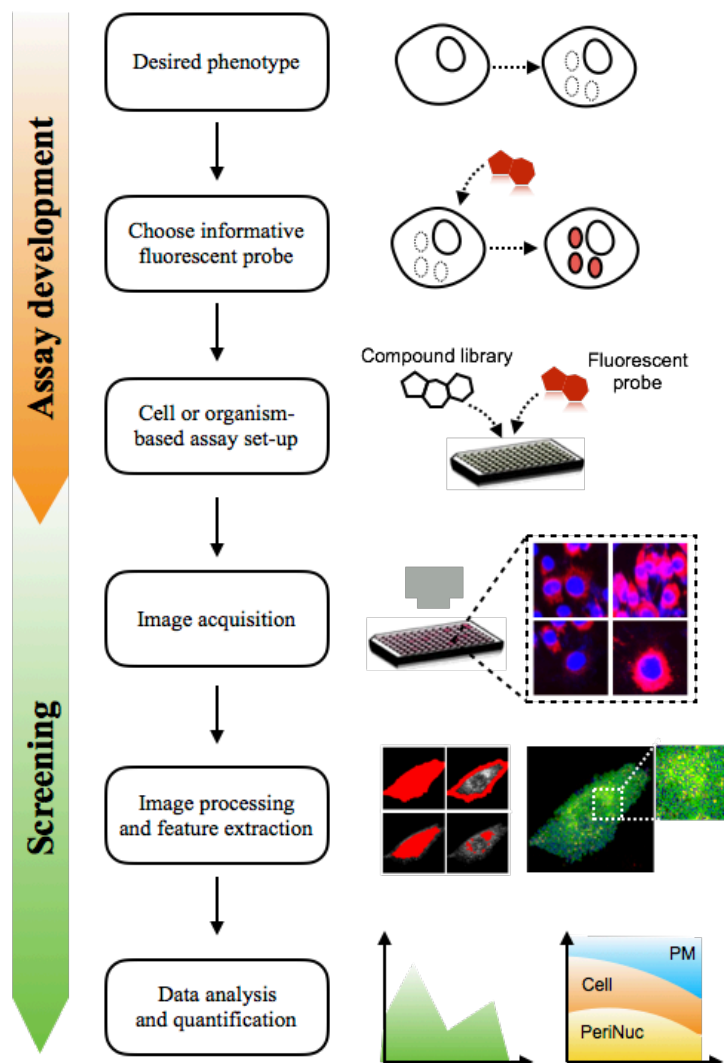


Figure 1.2. General process of image-based phenotypic screening to identify novel hits and lead compounds from small molecule compound library.

2. Metabolic syndrome

Metabolic syndrome is defined by a cluster of a metabolic risk factors including obesity, insulin resistance, hyperglycemia, hypertension and dyslipidaemia et al. Metabolic syndrome is considered as a life-threatening health problem in worldwide due to that having metabolic syndrome doubles the incidence of cardiovascular disease (CVD) and increases the incidence of type 2 diabetes mellitus (T2DM) by five times [10, 11]. In addition, many medical complications will result from metabolic syndrome including retinopathy, neuropathy, kidney disease and amputation of limbs [12]. Therefore, many researchers have been studying the cause and treatment of this disease.

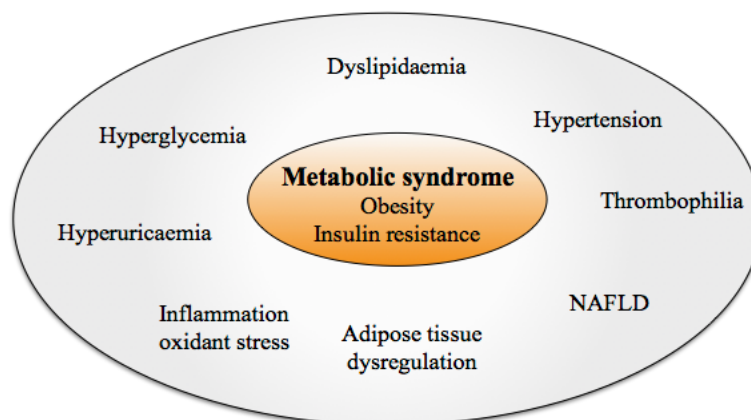


Figure 1.3. Risk factors for the occurrence of metabolic syndrome. The metabolic syndrome is a cluster of pathophysiological conditions including obesity, insulin resistance, hyperglycemia, dyslipidaemia, hypertension, thrombophilia, NAFLD, adipose tissue dysregulation, inflammation, oxidant stress, hyperuricaemia.

The most challenging part of the treatment of metabolic syndrome is that the pathogenesis of metabolic syndrome is a consequence of complex interplay between multiple metabolic parameters. Therefore, there's no single unifying therapeutic target to treat and manage the metabolic syndrome. Instead of that, preventive approaches are used to reduce the development of further medical complications by using medicines for each specific risk factor of metabolic syndrome.

Among the many risk factors, obesity and hyperglycemia are crucial factors for the pathogenesis of metabolic syndrome due to their causal links for the development of insulin resistance [13]. Insulin resistance is a condition of a normal concentration of insulin no longer stimulates the insulin response in target tissues, thereby causing impaired glucose metabolism and elevated blood glucose level (hyperglycemia). In this condition, pancreas secretes more insulin to reduce the blood glucose level which results in a consequence of hyperinsulinemia [14, 15]. Maintenance of this condition in turn worsen insulin resistance, and leads to severe hyperglycemia and T2DM. In addition, hyperinsulinemia is also associated with hypertension, dyslipidaemia and CVD. Taken together, insulin resistance is a key factor in the manifestation of metabolic syndrome. Therefore, there is a large demand for the pharmaceutical agent to manage obesity and hyperglycemia for combating metabolic syndrome.

In particular, obesity is one of the key factor for the development of insulin resistance and subsequent metabolic syndrome [16, 17]. As a key

endocrine organ, adipose tissue plays a key role in regulation of energy metabolism and homeostasis in our body. In obesity, a condition of excess accumulation of fats in adipose tissue, adipose tissue loses its normal endocrine functions, thereby causing the pathogenesis of metabolic disorders via various mechanism. For example, large amount of NEFAs are released from adipose tissue, leading to insulin resistance and lipotoxicity in β -cell, liver and muscle [18, 19]. In addition, adipose hormone (adipokines) and inflammatory cytokines (TNF- α and IL-6) are increased leading systematic insulin resistance [20]. Number of studies revealed that the obesity-induced insulin resistance mainly contributes to the development of metabolic disorders such as pro-inflammatory state, hyperglycemia, hypertension and atherosclerosis. Taken together, obesity results in imbalance of energy homeostasis, leading systematic metabolic disorder. Therefore, there is an urgent need for the pharmaceutical agent to manage obesity and obesity-associated metabolic disorders.

3. Glucose transporter 4 (GLUT4)

Glucose is the most important energy source for living organisms. The homeostasis of glucose is tightly regulated by multiple action of insulin hormone. Among them, glucose transporter 4 (GLUT4) is one of the most well-known membrane protein that its biological function is determined by the regulation of insulin [21]. Insulin controls blood glucose level by

4. Purpose

In this dissertation, I propose a phenotype-based approach to discover novel bioactive small molecules for metabolic diseases. Metabolic diseases are the consequence of complex interplay between multiple metabolic parameters in our body. Therefore, there's no single unifying therapeutic target to treat and manage the metabolic syndrome. In this regard, the target-based approach has some inevitable limitations for targeting metabolic diseases. First of all, although the insulin resistance is a key factor for the development of metabolic syndrome, development of insulin resistance is also a consequence of causal relationship with other pathophysiological conditions such as obesity and hyperglycemia. In addition, it is difficult to predict the clinical outcomes after inhibiting certain therapeutic target due to the complexity in metabolic homeostasis. For example, change in a function of therapeutic target could bring about subsequent unexpected changes in other metabolic organs. Therefore, I envision an alternative phenotype-based approach to overcome the limitations of target-based approach.

Among the many risk factors of metabolic syndrome, I focus on the hyperglycemia and obesity which are considered as a crucial risk factor for the development of metabolic syndrome. Here, I observed phenotypic changes of the cells using fluorescence bioprobes with high-throughput fluorescence imaging technology. In **chapter 2**, I suggest the phenotype-

based approach to discover bioactive small molecules for hyperglycemia with fluorescence glucose bioprobe. In **chapter 3**, I describe the development of an image-based assay system for monitoring dynamic GLUT4 trafficking to reveal the mechanism-of-action of chemical compounds which increase cellular glucose uptake. In **chapter 4**, I suggest the phenotype-based approach to discover anti-obesity small molecule via monitoring cellular lipid droplets. Taken together, I suggest the utility of image-based phenotypic screening for identifying new bioactive small molecules for combating T2DM and obesity and for understanding mode-of-action of bioactive small molecules.

5. References

1. J. Tang and T. Aittokallio, *Curr. Pharm. Des.* 2014, **20**, 23–36.
2. F. Sams-Dodd, *Drug. Discov. Today.* 2005, **10**, 139–147.
3. D. C. Swinney, *Clin. Pharmacol. Ther.* 2013, **93**, 299–301.
4. W. Zheng, N. Thorne and J. C. McKew, *Drug Discovery Today*, 2013, **18**, 1067–1073.
5. P. Ramm, *Curr. Opin. Biotechnol.* 2005, **16**, 41–48.
6. R. Macarron, M. N. Banks, D. Bojanic, D. J. Burns, D. A. Cirovic, T. Garyantes, D. V. S. Green, R. P. Hertzberg, W. P. Janzen, J. W. Paslay, U. Schopfer and G. S. Sittampalam, *Nat. Rev. Drug Discovery*, 2011, **10**, 188–195.
7. F. Zanella, J. B. Lorens and W. Link, *Trends. Biotechnol.* 2010, **28**, 237–245.
8. P. Lang, K. Yeow, A. Nichols and A. Scheer, *Nat. Rev. Drug Discovery*, 2006, **5**, 343–356.
9. A. Miyawaki, A. Sawano and T. Kogure, *Nat. Cell. Biol.* 2003, S1–S7.
10. K. G. M. M. Alberti, R. H. Eckel, S. M. Grundy, P. Z. Zimmet, J. I. Cleeman, K. A. Donato, J. C. Fruchart, W. P. T. James, C. M. Loria and S. C. Smith, *Circulation* 2009, **120**, 1640–1645.
11. P. W. F. Wilson, R. B. D’Agostino, H. Parise, L. Sullivan, J. B. Meigs, *Circulation* 2005, **112**, 3066–3072.
12. S. M. Grundy, J. I. Cleeman, S. R. Daniels, K. A. Donato, R. H. Eckel, B. A. Franklin, D. J. Gordon, R. M. Krauss, P. J. Savage, S. C. Smith, J. A. Spertus and R. Costa. *Circulation* 2005, **112**, 2735–2752.
13. M. P. Czech, *Nat. Med.* 2017, **23**, 804–814.
14. M. H. Shanik, Y. Xu, J. Skrha, R. Dankner, Y. Zick and J. Roth, *Diabetes Care.* 2008, S262–S268.
15. B. E. Corkey, *Diabetes* 2012, **61**, 4–13.

16. S. E. Kahn, R. L. Hull and K. M. Utzschneider, *Nature* 2006, **444**, 840–846.
17. P. G. Kopelman, *Med. Int.* 1994, **22**, 385–388.
18. A. Guilherme, J. V. Virbasius, V. Puri and M.P. Czech, *Nat. Rev. Mol. Cell. Biol.* 2008, **9**, 367–77.
19. N. C. Chavez-Tapia, N. Rosso and C. Tiribelli, *BMC Gastroenterol.* 2012, **12**, 20.
20. N. Ouchi, J. L. Parker, J.J. Lugus and K. Walsh, *Nat. Rev. Immunol.* 2011, **11**, 85–97.
21. Y. Minokoshi, C. R. Kahn and B. B. Kahn, *J. Biol. Chem.* 2003, **278**, 33609–33612.
22. G. M. Reaven, *Diabetes* 1988, **37**, 1595–1607.
23. P. S. Conti, D. L. Lilien, K. Hawley, J. Keppler, S. T. Grafton and J. R. Bading, *Nucl. Med. Biol.* 1996, **23**, 717–735.
24. Nehlig, E. Wittendorp-Rechenmann and C. Dao Lam, *J. Cereb. Blood Flow Metab.* 2004, **24**, 1004–1014.

Chapter 2. Construction of image-based high-throughput screening to discover novel glucose uptake enhancers

2.1. Introduction

Glucose is one of the most important energy and carbon sources for most living organisms. The homeostasis of glucose is precisely regulated in our body [1], and an abnormal cellular glucose uptake/metabolism is considered as a marker for Type 2 Diabetes Mellitus (T2DM) [2]. Therefore, monitoring of cellular glucose utilization has been used as a diagnostic tool in drug discovery [3]. To monitor the cellular glucose utilization, radioisotope-labeled glucose analogues such as [^{18}F]-2-fluoro-2-deoxy-D-glucose (^{18}F FDG), [^{14}C]-2-deoxy-D-glucose (^{14}C -2-DG), and [^{14}C] or [^3H]-3-O-methyl-D-glucose have been developed and ^{18}F FDG has been most widely used as a radioactive tracer for cancer diagnosis in medical imaging modalities using positron-emission tomography (PET) [4]. However, poor spatial and temporal resolution limits the application of radioactive probes in cellular imaging and screening [5]. In this context, fluorescent glucose analogues that can monitor the cellular glucose uptake have drawn enormous attention from biomedical communities [6]. The

first fluorescence-labeled glucose bioprobe, 6-NBDG, was developed in 1985 [7] and subsequently various fluorescent glucose bioprobes have been developed [8]. Among them, 2-NBDG (Figure 2.1A) has been extensively used for *in vivo* tumor imaging, and for the monitoring of individual cellular glucose uptake [9]. Analysis of individual cells by fluorescent glucose probes improves our understanding of the heterogeneity of the disease states and the differential susceptibility of the treatment *in vivo* [10]. Moreover, real-time bioimaging of cellular glucose uptake with confocal laser scanning microscopy (CLSM) also facilitates a better understanding of dynamic change in metabolic states of individual cells upon various treatments [11]. Overall, fluorescent glucose probes advanced our knowledge of the disease state and its diagnosis [12].

There is a growing demand for the discovery of novel anti-diabetic agents with new modes of action [14]. The characteristic phenotype of anti-diabetic agents is the enhancement of cellular glucose uptake in metabolically active target tissues such as muscle and adipose. Therefore, the discovery of novel small molecules that regulate cellular glucose uptake in muscle or adipose tissues would be a promising drug candidate against type 2 diabetes and metabolic syndrome. Meanwhile, 6-NBDG have been utilized in the screening systems [15], but they suffered limited practicality and applicability issues in HTS. Especially, the reported HTS screenings were performed by using a microplate reader instead of

microscopy after cell lysis probably due to the weak fluorescence intensity and fast photo-bleaching of 6-NBDG.

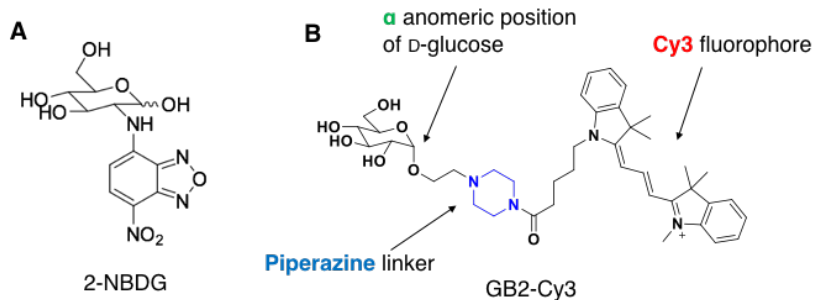


Figure 2.1. (A) Structure of 2-NBDG. (B) Structure of GB2-Cy3.

Our laboratory has reported the development of novel glucose bioprobe, GB2-Cy3 (Figure 2.1B), and have been demonstrated its application in real-time and quantitative monitoring of glucose uptake in metabolically active cells by using fluorescence microscopy and flow cytometry [13]. Fluorophore of GB2-Cy3 is a Cy3 which has superior photophysical property than NBD dye in 2- and 6-NBDG. Molar absorptivity of Cy3 is 10-fold larger than that of NBD. Therefore, sensitivity of GB2-Cy3 is dramatically increased. Sensitivity of fluorescent probe guarantees ‘High-throughput’ of image-based screening. Therefore, I envisioned the development of an image-based HTS system using a fluorescent glucose bioprobe GB2-Cy3 that has high fluorescence intensity and stable photophysical properties.

In the present study, I constructed image-based HTS to discover to discover novel glucose uptake enhancers. Prior to establishment of screening system, I explored the mechanism of cellular uptake/release of GB2-Cy3 to verify the reliability and accuracy of the screening, and demonstrated the GLUT-specific cellular uptake of GB2-Cy3. Moreover, I examined the relationship between molecular charge of glucose bioprobes and their GLUT-specific uptake. Although various glucose bioprobes labeled with different fluorophores were reported [13, 16-23], there was no systematic report on the effect of fluorophore structure on these glucose bioprobes. Thus, it is worth exploring the influence of fluorescence dyes on the cellular uptake of glucose bioprobes.

2.2. Materials and methods

General materials

^1H and ^{13}C NMR spectra were recorded on an Agilent 400-MR DD2 [Agilent, USA], Bruker DRX-300 [Bruker] and a Varian Inova-500 [Varian Assoc], and chemical shifts were measured in ppm downfield from internal tetramethylsilane (TMS) standard or specific solvent signal. Product mass analyses were performed on LC/MS system equipped with a reverse phase column (C-18, 50 x 2.1 mm, 5 μm) and photodiode array detector using electron spray ionization (ESI) or atmospheric pressure chemical ionization (APCI). Reverse phase HPLC analysis was performed on a VPODS C-18 column (150 x 4.6 mm) at a flow rate of 1.0 mL/min for analysis, and PRC-ODS C-18 column (250 x 20 mm) at a flow rate of 10.0 mL/min for preparation, Shimadzu LC-6AD pump, SPD-10A detector (Japan). HPLC solvents consist of water containing 0.1% TFA (solvent A) and acetonitrile containing 0.1% TFA (solvent B). All chemical reagents in this synthetic procedure were purchased from Sigma-Aldrich and TCI. All reactions were conducted in oven-dried glassware under dry argon atmosphere, unless otherwise specified. CH_2Cl_2 was distilled from CaH_2 immediately prior to use. Other solvents and organic reagents were purchased from commercial vendors and used without further purification unless otherwise mentioned. Ez-cytox kit was purchased from Daeil Co. and was used for the cell viability test. Hoechst 33324 and 6-NBDG were

purchased from Invitrogen. 4,6-O-ethylidene- α -D-glucose (4,6-EDG), insulin from bovine pancreas and rosiglitazone were purchased from Sigma-Aldrich. 2-(N-(7-Nitrobenz-2-oxa-1,3-diazol-4-yl)amino)-2-deoxyglucose(2-NBDG) was purchased from Invitrogen. Cytochalasin B was purchased from Santa Cruz Biotechnology. Emodin was a gift from Professor Wong-Keun Oh, Seoul National University, Republic of Korea. GAPDS was a gift from Professor Young-Tae Chang, National University of Singapore.

Fluorescence microscope, HTS equipment, and analysis program for biological cell imaging experiment

I carried out fluorescence microscopy studies with Olympus Inverted Microscope Model IX71, equipped for epi-illumination using a halogen bulb [Philips]. Emission signal of each experiments were observed at a spectral setting: red channel using a 510–550 band pass exciter filter, a 570 nm center wavelength chromatic beam splitter, a 590 nm-long pass barrier filter [Olympus]. Quantification of fluorescence images was performed by Image-Pro Plus[®] 6.2 program and all graphs were figured by GraphPad Prism 5. The quantified data are the mean measurements of 40–50 cells from at least three different independent experiments. HTS was performed by InCell analyzer 2000 [GE Healthcare] and fluorescence images were analyzed by InCell analyzer 1000 workstation 3.6 program according to manufacturer's protocol.

Cell culture

HeLa (human cervical cancer) cells and C2C12 (mouse myoblast) cells were obtained from ATCC [American Type Culture Collection, USA]. C2C12 cells were cultured in Dulbecco's modified Eagle medium (DMEM) containing 10% fetal bovine serum (FBS) and 1% antibiotic-antimycotic solution at 37 °C in an atmosphere of 5% CO₂. HeLa cells were cultured in RPMI 1640 containing 10% FBS and 1% antibiotic-antimycotic solution at at 37 °C in an atmosphere of 5% CO₂.

Glucose competition test

To measure the competitive cellular uptake of glucose bioprobes, C2C12 or HeLa cells were cultured on a cover glass bottom dish were incubated for 30 min at 37 °C in the presence of individual fluorescent glucose bioprobes in DMEM containing 55 mM D-glucose, 11 mM D-glucose, or no glucose. The final concentration of fluorescence glucose bioprobes was adjusted to 10 μM. After washing with cold PBS, fluorescence images were obtained at an excitation wavelength of 488 nm by using a fluorescence microscope (Olympus IX71).

Inhibition of endocytosis in C2C12 myoblast cells

C2C12 myoblast cells cultured on a cover glass bottom dish were incubated for 30 min with GB2-Cy3 or L-GB2-Cy3. The final concentration of fluorescence glucose bioprobes was adjusted to 10 μM.

During the incubation, temperature was adjusted to 37 °C or 4 °C. After washing with cold PBS, fluorescence images were obtained at an excitation wavelength of 488 nm by using a fluorescence microscope (Olympus IX71).

Radiolabeled 2-deoxyglucose uptake measurement

C2C12 myoblast cell cultured on a 24-well plate were treated with 10 μ M of P33A04, P33D04, P33F06, P33G07, and DMSO, and incubated for 24 h at 37 °C with 5% CO₂. After washing with cold PBS, cells were treated with ¹⁴C-labeled 2-deoxyglucose (0.1 μ Ci/ml) in HEPES-buffered saline (HBS) and incubated for 10 min at 37 °C with 5% CO₂. The cells were then washed 3 times with PBS, added 50 μ L of RIPA buffer, and kept on ice for 2 h. After cell lysis, centrifuge for 10 min at 15000 g and collect supernatants, and measured radioactivity using Liquid Scintillation Counter.

Non-radiolabeled 2-deoxyglucose uptake measurement

C2C12 myoblast cells cultured on a 6-well plate were treated with 10 μ M of P33A04, P33D04, P33F06, P33G07, and DMSO, and incubated for 24 h at 37 °C with 5% CO₂. After washing with cold PBS, cells were treated with 1 mM 2-deoxyglucose in PBS and incubated for 20 min at 37 °C with 5% CO₂. After washing three times with PBS, cells were harvested, added 500 μ L of 10 mM Tris-HCl buffer, and sonicated with Sonomacher. After

heat inactivation at 80 °C for 15 min and centrifugation at 15,000 g for 10 min, the supernatants were collected. We measured the amount of 2-deoxyglucose-6-phosphate according to the manufacturer's protocol for 2-deoxyglucose (2-DG) Uptake Measurement Kit (COSMO BIO Co., ltd.)

High-throughput screening (HTS) using InCell Analyzer 2000

C2C12 myoblast cells were seeded on black well and clear bottom 96 plate (2×10^3 cells/well) and incubated at 5 % CO₂, 37 °C for overnight. Various chemicals from our in-house pDOS library were treated to the designated cells with pin tool at 10 μ M of final concentration for 24 h. GB2-Cy3 (5 μ M) and Hoechst 33342 (2 μ g/mL) was added to individual cells. After 30 min incubation at 37 °C, cells were washed twice with pPBS and prepared for imaging with 100 μ L of pPBS per well after last washing. Fluorescence images of the resulting plate were taken automatically by InCell Analyzer 2000. GB2 image was captured with excitation filter at 543 ± 11 nm and emission filter in red channel. The fluorescence image of Hoechst 33342 was captured with excitation filter at 350 ± 25 nm and emission filter in blue channel.

In Vitro Cytotoxicity Test

Cell viability was measured by the EZ-cytox assay kit, and the experimental procedure was based on the manufacturer's manual. Briefly, cells were cultured into 96-well plates at a density of 3×10^3 cells/well for

24 h, followed by the treatment of individual compounds at various concentrations. After 24 h of incubation at 37 °C, 10 μ L of WST-1 solution [2-(4-nitrophenyl)-5-(2-sulfophenyl)-3-[4-(4-sulfophenylazo)-2-sulfophenyl]-2H-tetrazolium disodium salt] was added to each well, and the resulting plates were incubated for an additional 10 min at 37 °C. Absorbance in 455 nm was measured by microplate reader. The percentage of cell viability was calculated by following formula: % cell viability = (mean absorbance in test wells)/(mean absorbance in control well) \times 100. Each experiment was performed in triplicate.

HPLC analysis for monitoring physiological state of GB2 after cellular uptake

C2C12 myoblast cells were treated with GB2-Cy3 for 30 min and washing three times with cold pPBS. The resulting cells were treated with RIPA buffer and stored at -78°C for 30 min. The lysed cells were centrifuged at 14000 rpm for 10 min. Then, the supernatant was collected and added with cold acetone to precipitate proteins. After centrifugation at 14000 rpm for 10 min, the supernatant was collected and lyophilized to remove all liquids. The resulting residue was solubilized with methanol and subjected to HPLC analysis to identify the GB2-Cy3 recovered from cytoplasm. The HPLC analysis was performed using UV detector at 550 nm for the selective monitoring of GB2-Cy3 with the UV absorbance of Cy3 dye.

Zebrafish maintenance

Zebrafish were maintained in accordance with standard guidelines. Care and treatment of zebrafish were conducted in accordance with guidelines established by the Animal Care and Ethics Committees of the Gwangju Institute of Science and Technology, Republic of Korea. Wild-type zebrafish (*Danio rerio*) were maintained in 10 L glass tanks with 28.5 °C filtered tap water and a photoperiod of 14:10 h (light:dark). Fish were fed twice daily using combination of brine shrimp (*Artemia salina*) and dry food (Amazon Flake). For all experiments, embryos were obtained by in vitro fertilization following standard procedures.

Evaluation of GB2-Cy3 uptake in zebrafish

Fish eggs were incubated in E3 water (5 mM NaCl, 0.17 mM KCl, 0.33 mM CaCl₂ and 0.33 mM MgSO₄ in distilled water) supplemented with 0.2 mM 2-phenylthiourea (a depigmentation compound that increases larvae transparency). At 72 hpf the larvae were placed into a 96-well plate at a density of 6 embryos/well for microplate reader analysis, or 3 embryos/well for fluorescence microscopy, in 200 μ L E3 water. Larvae were incubated with GB2-Cy3 for 3 h. To assess the effect of test compounds on GB2-Cy3 uptake, the larvae were exposed to the compounds for 1 h prior to the addition of GB2-Cy3. E3 water containing the test compounds were then removed and replaced with GB2-Cy3 dissolved in E3 water.

For fluorescence microscopy, the E3 water containing GB2-Cy3 was removed and the larvae were then washed with E3 water and anesthetized with 0.02 % tricaine dissolved in E3 water. The larvae were then placed on glass microscope slides in plastic chambers (1.6 cm diameter and 3 mm depth) containing 3% methylcellulose dissolved in E3 water. Images of GB2-Cy3 uptake were captured using fluorescent microscopy (DM2500, Leica) equipped with a digital camera (DFC425C, Leica). Three larvae were imaged for each experimental sample. Images were processed using the Lieca Application Suite software and Photoshop CS4 (Adobe Systems Incorporated). GB2-Cy3 uptake into the larvae was quantified with Image J software (National Institutes of Health).

To measure GB2-Cy3 uptake using a fluorescent microplate reader, larvae from each treatment group were placed in a 1.5 mL microfuge tube and lysed with 120 μ L CellLytic M solution (Sigma-Aldrich) and mechanical disaggregation using watchmaker forceps. Larvae were then sonicated (Vibra- Cell VCX500) at 4 °C with a 10 sec 'on' and 5 sec 'off' pulse for 15 min (i.e. total time of 10 min for sonication plus 5 min pause), followed by centrifugation at 10000 rpm for 10 min. The supernatant (100 μ L) was transferred to a 96-well plate and NBDG signal was measured with a fluorescent microplate reader (SpectraMAX Gemini XS, $\text{ex}=485$ nm, $\text{em}=535$ nm). For microplate reader analysis, each 9 experimental samples were measured in triplicate wells.

Statistical analysis

The results are shown as means \pm SEM. The student's t-test was used for comparison between experimental groups (Microsoft Excel). P values of <0.05 were considered significant. Unless otherwise stated, all results are the average of three independent experiments and the error bars are standard deviation of the mean.

2.3. Results and discussion

2.3.1. Exploiting the mechanism of cellular uptake of the fluorescent bioprobe, GB2-Cy3

Design of L-GB2-Cy3, an enantiomeric pair of GB2-Cy3. The transport of D-glucose across the cellular membrane in mammalian cells is mediated by energy-coupled and facilitative mechanisms by the protein family of sodium-driven sugar co-transporter (SGLTs) and of glucose transporters (GLUTs) [14, 24], respectively. Among them, GLUTs maintain the glucose homeostasis in an energy-independent manner within the body *via* controlling their subcellular translocation [15, 25]. Due to high polarity of glucose, its transport through passive diffusion is strictly prohibited. Therefore, fluorescent glucose bioprobes should be able to visualize the GLUT-dependent transport of D-glucose in live cells.

Previous studies confirmed that GB2-Cy3 enters the cell through GLUTs in a competitive manner with D-glucose [13]. However, it is still possible that GB2-Cy3 to enter the cytoplasm partly *via* either energy-dependent endocytosis and passive diffusion. To address this issue, I investigated the detailed uptake mechanism of GB2-Cy3 in the cellular system. I focused on the fact that endogenous GLUTs can differentiate the D-glucose from the L-glucose [16, 26]. In this context, I hypothesized that the chiral

environment in GLUTs can selectively allow the entrance of GB2-Cy3 into the cytoplasm through GLUTs. To test this hypothesis, I synthesized L-GB2-Cy3, an enantiomeric pair of GB2-Cy3 (Figure 2.2A).

D-Glucose competition assay with GB2-Cy3 and L-GB2-Cy3. I performed a glucose competition assay with GB2-Cy3 and L-GB2-Cy3 in C2C12 myoblast cells to monitor physiological behavior of two probes. As shown in figure 2.2B, D-glucose successfully competed out the cellular uptake of GB2-Cy3 in a concentration-dependent manner. These data indicating that the translocation of GB2-Cy3 is mainly mediated by GLUTs. On the other hands, there was no competitive decrease of L-GB2-Cy3 cellular uptake even at the highest concentration of D-glucose (55 mM). This result confirmed that there are distinctly different cellular uptake mechanisms between GB2-Cy3 and L-GB2-Cy3 owing to their difference in stereochemistry in the glucose analog part (D- and L-glucose), and GB2-Cy3 can mimic the translocation of D-glucose in cellular systems because of its GLUT specificity.

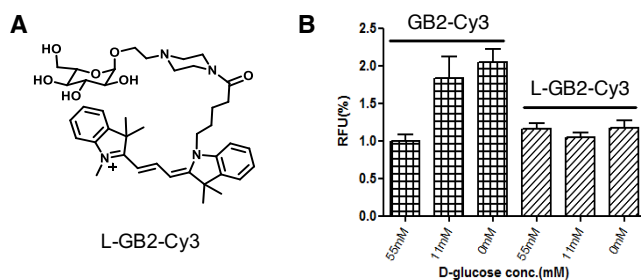


Figure 2.2. (A) Structure of L-GB2-Cy3. (B) Glucose competition assay with GB2-Cy3 and L-GB2-Cy3 in C2C12 myoblast cell line.

Suppression of endocytosis and its influence on GB2-Cy3/L-GB2-Cy3 cellular uptake. On the other hands, the basal cellular uptake level of L-GB2-Cy3 might be caused by either nonspecific endocytosis or passive diffusion. When I inhibited the endocytosis process by lowering the temperature during the incubation of probes [17, 27], a 75% of reduction in L-GB2-Cy3 uptake was observed, whereas the GB2-Cy3 uptake was marginally affected under the identical condition (Figure 2.3). Based on these observations, I convinced that the cellular uptake of GB2-Cy3 is mainly associated with cellular GLUTs. Thus, the image-based monitoring of GB2-Cy3 fluorescence signal can serve as a useful measurement of the cellular glucose uptake.

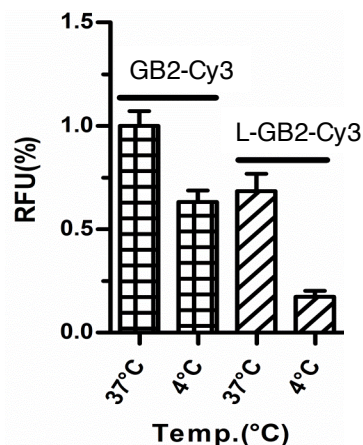


Figure 2.3. Suppression of endocytosis and its influence on GB2-Cy3/L-GB2-Cy3 cellular uptake. Relative fluorescence units (RFU) were determined from the ROI, and the data are the average values obtained in measurements performed on 40-50 cells. Error bars indicate SEM.

Release of GB2-Cy3. In the context of the fundamental role of glucose as a cellular energy source, the phosphorylation of glucose is an essential step to generate energy currency (ATP) and other cellular elements *via* the pentose-phosphate pathway once D-glucose enters the cytoplasm through GLUTs along its concentration gradient (Figure 2.4) [18, 28]. ^{18}F FDG and 2-NBDG are known to be phosphorylated by hexokinases as glucose and thereby ^{18}F FDG and 2-NBDG can be trapped within cells for an extended period of time, although the phosphorylation of 2-NBDG leads to rapid degradation into non-fluorescent products [19, 29]. However, GB2-Cy3 is not a substrate for hexokinases.

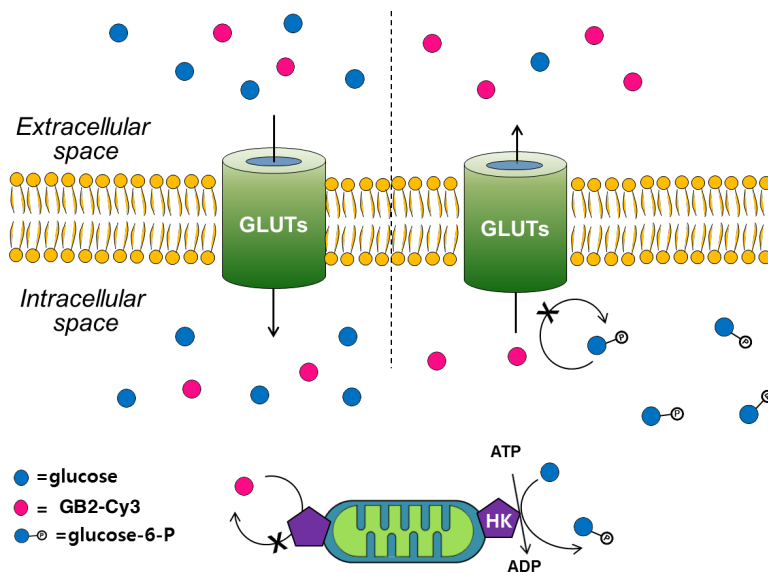


Figure 2.4. Schematic diagram of the physiological behavior of D-glucose and GB2-Cy3.

Because of this physiological behavior of GB2-Cy3, a conventional bioimaging procedure will lead to time-dependent loss of fluorescent signals, caused by the efflux of non-phosphorylated GB2-Cy3 from the cells through GLUTs due to its reversed concentration gradient after washing step. When C2C12 myoblast cells were treated with 2,4-dinitrophenol (DNP)—a reported small-molecule enhancer of cellular glucose uptake through shuffling protons across the mitochondrial membrane [20, 30], I observed high intensity of GB2-Cy3 fluorescence signals in the cytoplasm. However, this fluorescence signal was deteriorated down to that of DMSO control within 5 min, as observed by continuous monitoring of fluorescence intensity (Figures 2.5A and B). This phenomenon is a critical challenge for the bioimaging with GB2-Cy3 because the signal read-out will be significantly affected by the inevitable difference in its detection time, especially in a high-throughput screening.

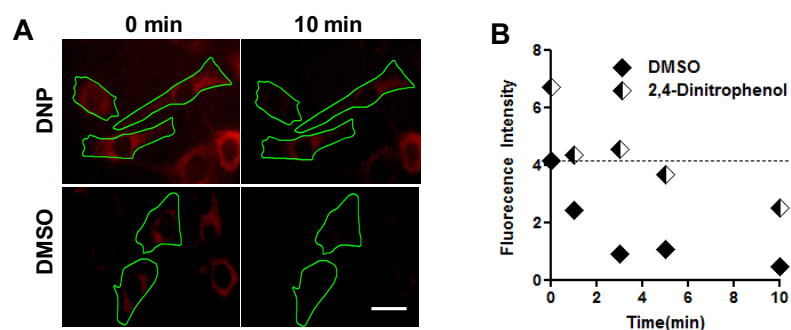


Figure 2.5. (A) Time-dependent signal loss of GB2-Cy3 within the cytoplasm of C2C12 myoblasts. The scale bar represents 20 μm . (B) Continuous monitoring of the time-dependent signal in living C2C12 myoblasts upon treatment with DNP. Fluorescence intensity was determined from the region of interest (ROI) in C2C12 cells.

Suppression of release of GB2-Cy3 using specific GLUT inhibitor. In this context, I aimed to suppress the GB2-Cy3 release after the washing step by using specific GLUT inhibitor. Among the reported specific GLUT inhibitors, I selected phloretin—a natural dihydrochalcone known to be a transient and competitive inhibitor of GLUTs [21, 31]. The treatment of phloretin was expected to inhibit the GLUT-based escape of GB2-Cy3 and to retain the fluorescence signal within the cytoplasm (Figure 2.6). As shown in figure 2.7A, the initial fluorescence intensity of GB2-Cy3 in the cytoplasm was significantly decreased within 30 min, but the treatment with phloretin preserved the fluorescence intensity of GB2-Cy3 over 60 min (Figure 2.7A and 2.7B). This result indicated that the major loss of fluorescence signals in the cytoplasm was caused by GLUT-mediated excretion of GB2-Cy3, which can be effectively blocked by treatment with GLUT inhibitor, phloretin.

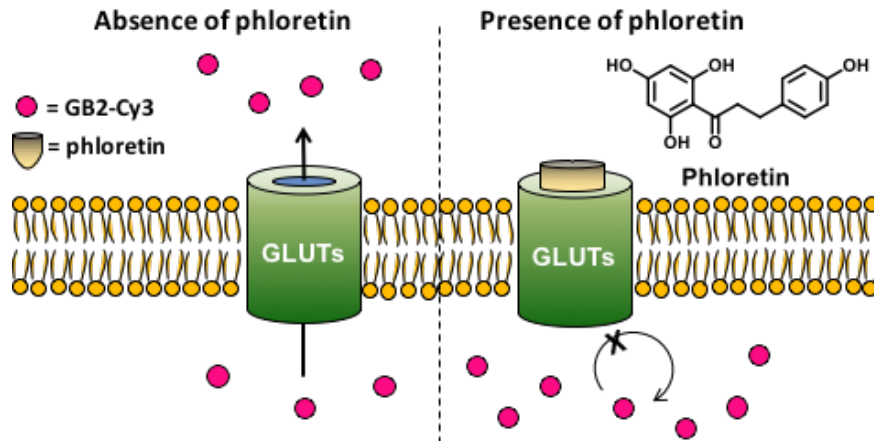


Figure 2.6. Schematic of the physiological behavior of GB2-Cy3 in the presence or absence of phloretin, with its chemical structure.

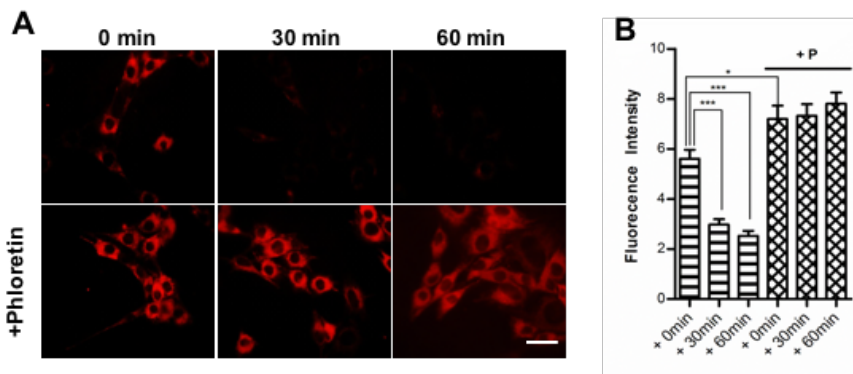


Figure 2.7. (A) Fluorescence microscopic images of cells obtained after washing with cold PBS in the presence and absence of phloretin (20 μ M). The scale bar represents 20 μ m. (B) Fluorescence intensities were determined from the ROI and the data are the average values obtained in measurements performed on 40–50 cells. Error bars indicate SEM; *** p <0.0001, ** p <0.005, and * p <0.01.

2.3.2. Impact of molecular charge on GLUT-specific cellular uptake

Design and synthesis of GB2-Cy3 derivatives having different molecular charge of the fluorophore. Recently, the molecular charge of fluorescence dyes has been studied due to their potential influence on cellular uptake. Frangioni and coworkers reported that the zwitterionic fluorophore shows better performance in optical *in vitro* and *in vivo* imaging compared with cationic or anionic dyes [32-34]. Without structural differences of the dyes, molecular charge might affect the non-specific cellular uptake of fluorophores. Inspired by their work, we anticipated that the molecular charge of fluorophores in glucose bioprobes could affect their GLUT-specific cellular uptake. To test this hypothesis, I synthesized two GB2-Cy3 derivatives with zwitterionic Cy3 (GB2-Cy3-S1) and -1 charged Cy3 (GB2-Cy3-S2) to modify the molecular charge of original GB2-Cy3 with $+1$ charged Cy3 (Figure 2.8A). Three glucose bioprobes have different charges on Cy3 ($+1$, 0 , -1) with minimal structural differences. The expected net charge of these glucose bioprobes in water at pH 7.4 is consistent with calculated molecular charges using the Marvin Sketch program (Figure 2.8B).

Prior to the cellular application of these three glucose bioprobes, I measured their photophysical properties (Figure 2.9). Fluorescence intensity and quantum yield of glucose bioprobes in methanol and water

was increased as the molecular charge of Cy3 become negative, which is consistent with previous reports [35]. The increased number of sulfonate groups on cyanine dyes improved their photophysical properties. Initially, I expected that the ameliorated photophysical properties of GB2-Cy3-S1 and GB2-Cy3-S2 might lead to an improved version of glucose bioprobe compared to the original GB2-Cy3.

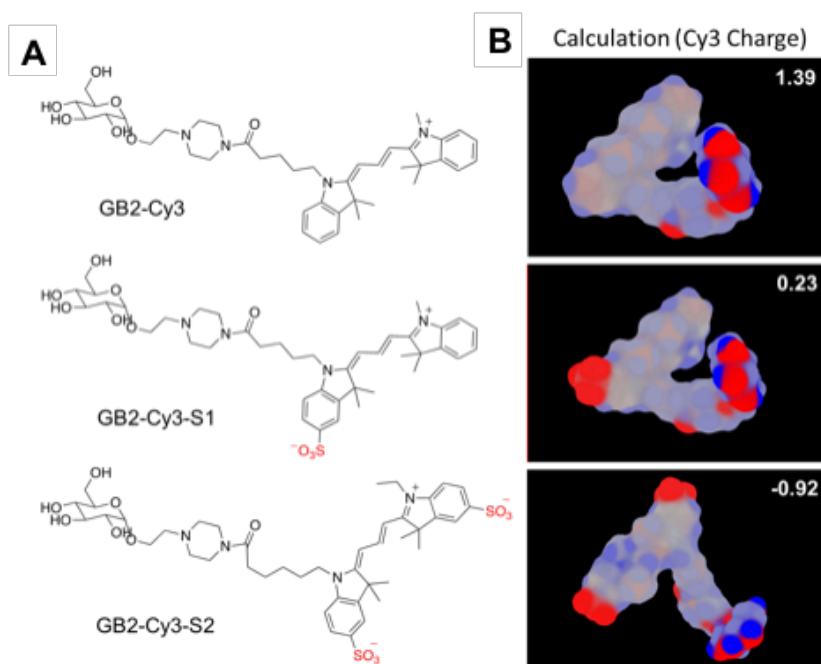


Figure 2.8. (A) Chemical structure of GB2-Cy3, GB2-Cy3-S1, and GB2-Cy3-S2. (B) Molecular charge calculation and surface charge area modeling of three glucose bioprobes using Marvin sketch 6.1.6. Molecular charge of Cy3 in pH 7.4 is displayed in white numbers in the picture.

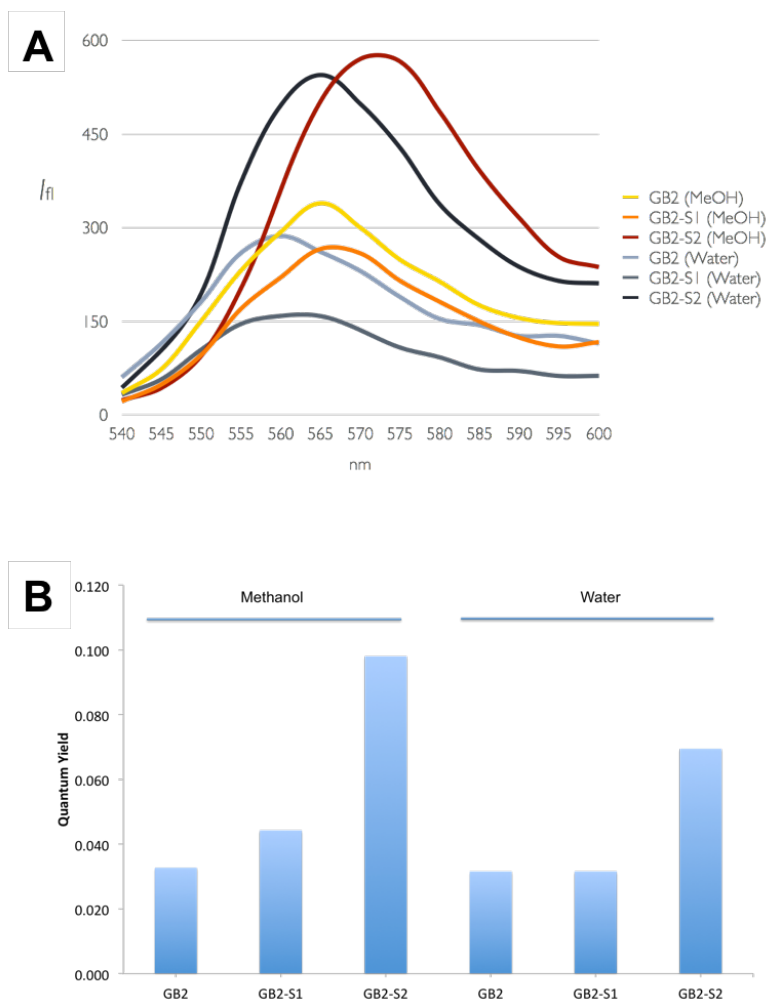


Figure 2.9. (A) Fluorescence emission spectra and (B) absolute quantum yields of GB2-Cy3, GB2-Cy3-S1, and GB2-Cy3-S2 in methanol and water.

Relationship between molecular charge of glucose bioprobes and their GLUT-specific uptake in *in vitro* system. To study the relationship between molecular charge of fluorophore and GLUT-specific uptake of glucose bioprobes, I examined the GLUT-specific uptake of three probes in *in vitro* system. To find an optimal condition for cellular imaging, first of all, I treated each probes to the human cervical carcinoma HeLa cell line for 30 min and acquired fluorescence images with a 1/1000 sec exposure time (Figure 2.10A). Interestingly, cellular uptake of GB2-Cy3-S1 and GB2-Cy3-S2 were not observed, in contrast to that of GB2-Cy3. When the exposure time is increased up to 1/5 sec from 1/1000 sec, cellular uptake of GB2-Cy3-S1 was barely observed, but not in the case of GB2-Cy3-S2. Even though, unlike GB2-Cy3-S2, GB2-Cy3-S1 shows a dose-dependent cellular uptake pattern (Figure 2.10B), cellular uptake of GB2-Cy3-S1 was still not observed at the 1/1000 sec exposure time, even at the highest concentration. Based on these experiments, I concluded that the cellular uptake of GB2-Cy3 is superior to that of GB2-Cy3-S2 and GB2-Cy3-S1, which is exactly opposite to the expectation concerning the improved photophysical properties of these GB2-Cy3 derivatives.

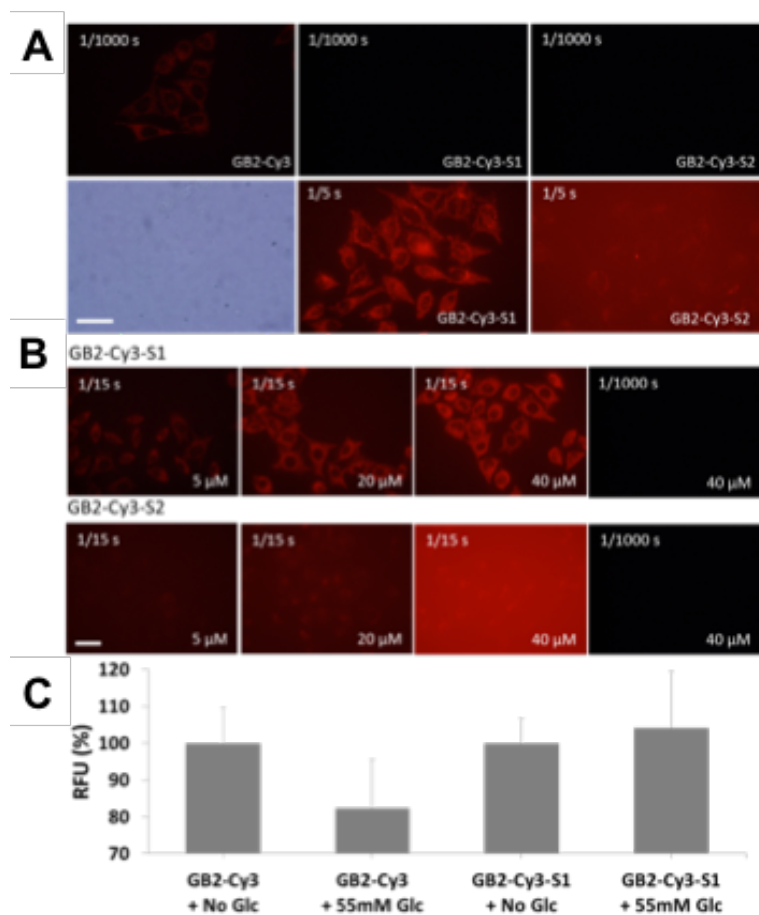
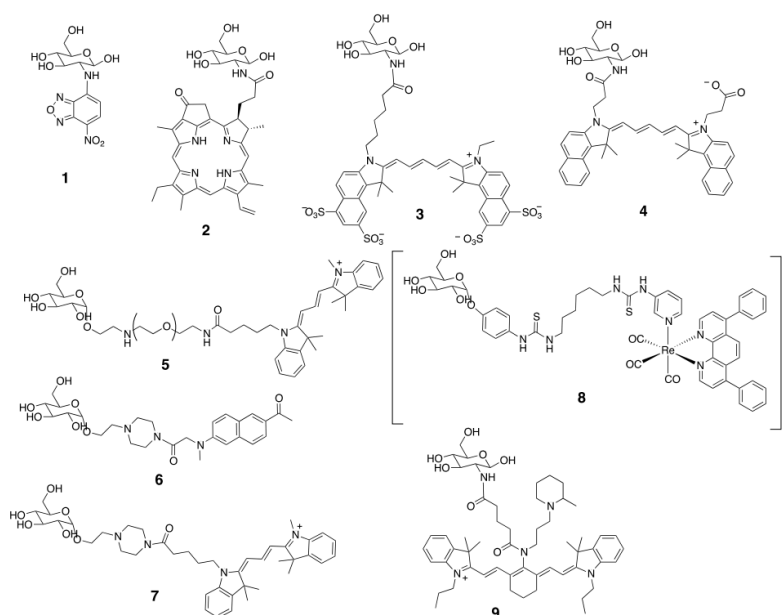


Figure 2.10. (A) Fluorescence microscopic images after cellular uptake of GB2-Cy3, GB2-Cy3-S1, and GB2-Cy3-S2 (10 μ M each) in HeLa cells. The images were captured after 1/1000 and 1/5 sec exposure time. The scale bar represents 20 μ m. (B) Dose-dependent cellular uptake of GB2-Cy3-S1 and GB2-Cy3-S2. The images were captured after 1/1000 and 1/5 sec exposure time. The scale bar represents 20 μ m. (C) Glucose competition assay with GB2-Cy3, and GB2-Cy3-S1 with 55 mM D-glucose.

D-Glucose competition assay with GB2-Cy3 and GB2-Cy3-S1.

Although cellular uptakes of two glucose bioprobes were reduced compared to that of GB2-Cy3, new bioprobes might have better selectivity for GLUT-specific cellular uptake. To test this hypothesis, I performed the competition assay and showed that cellular uptake of GB2-Cy3 was reduced as previously reported, but that of GB2-Cy3-S1 was not affected, even in the presence of a high concentration of free D-glucose (Figure 2.10C). In contrast to the observation of the Frangioni group, zwitterionic property in fluorophores was not beneficial for the GLUT-specific cellular uptake of glucose bioprobes. The positively charged version of glucose bioprobe, original GB2-Cy3, showed the best performance in *in vitro* cellular imaging. These interesting results could be a clue for the cellular behavior of previously reported glucose bioprobes. Zwitterionic [18]- and negatively charged [19]-glucose bioprobes, reported in 2004 and 2006, were not GLUT-specific and showed no competition with free D-glucose (Figure 2.11). Other reported glucose bioprobes with positive or no net charge generally showed good performance as a glucose tracer with GLUT specificity. On the basis of this finding, along with previously reported glucose bioprobes, I am confident that the molecular charge is important and can serve as one of the guidelines for the rational design of new glucose bioprobe.



Glucose Bioprobe	Expected Charge	Calculated Charge	GLUT specific cellular uptake
1	Neutral	-0.02	Specific
2	Neutral	0.39	Specific
3	Anion	-2.82	Nonspecific
4	Zwitterion	0.63	Nonspecific
5	Cation	1.39	Specific
6	Neutral	-0.05	Specific
7	Cation	1.39	Specific
8	Cation	2.94	Specific
9	Cation	2.77	Specific

Figure 2.11. Chemical structures of the previously reported glucose bioprobes and their molecular charges and biophysical properties. Cellular uptake of neutral and cationic charged glucose bioprobes are GLUT-specific as previously reported, but that of anionic and zwitterionic charged glucose bioprobes are not.

2.3.3. Construction of image-based high-through screening

Achievement of high reproducibility and accuracy of the screening. To ensure the reliable evaluation of a large number of compound library, it is crucial to have a high level of robustness and fidelity in the assay system. In this context, I considered that the biophysical properties of GB2-Cy3 about its time-dependent loss of fluorescent signals will be the critical challenge for the image-based HTS because the signal read-out will be significantly affected by the inevitable difference in its detection time, especially when screens large number of compounds. Based on this finding, I blocked the efflux of GB2-Cy3 by the treatment of phloretin, a transient and selective GLUT4 inhibitor, to sustain the fluorescence signals inside the cells for bioimaging. The treatment of phloretin during the imaging step suppressed the substantial efflux-based decrease in fluorescence signals over the extended measurement time (at least 30 min) (Figure 2.12 and 2.13).

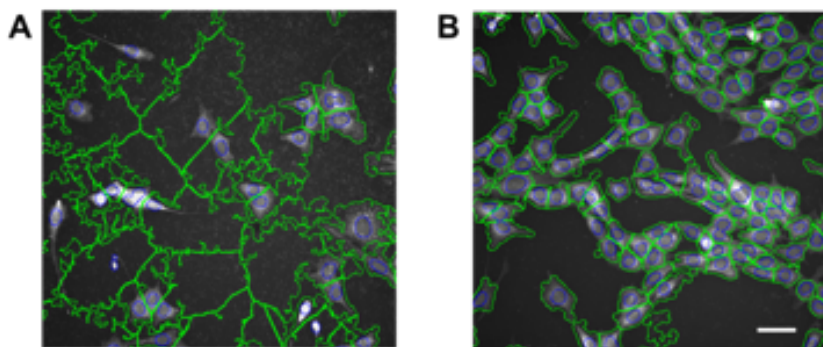


Figure 2.12. Effect of phloretin on the quantitative analysis of cellular fluorescence intensity in the high-throughput screening system. After the treatment of GB2-Cy3 and subsequent washing with (A) PBS or (B) pPBS, fluorescence images were taken by InCell analyzer 2000 and fluorescence images were automatically analyzed by InCell analyzer 1000 workstation 3.6 program. Blue line represents the automatically established boundary for cellular nucleus and green line represents automatically established boundary for individual cells. The scale bar represents 20 μm . The imaging condition (A) failed the automatic recognition of cell boundary due to the extensive efflux of GB2-Cy3.

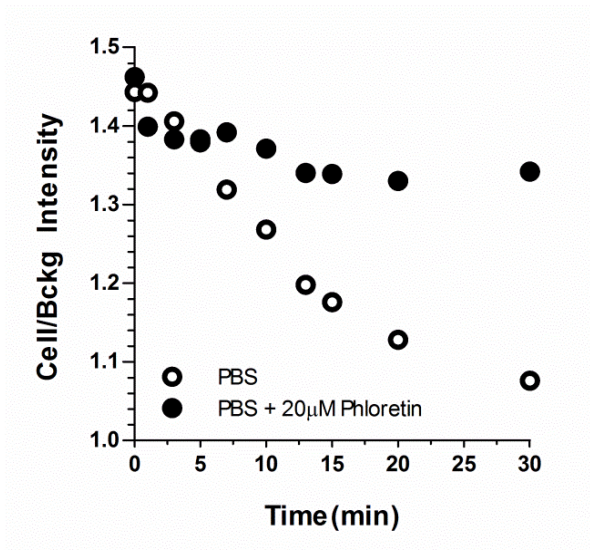


Figure 2.13. Continuous monitoring of GB2-Cy3 fluorescence intensity within the cytoplasm in the presence and absence of phloretin (20 μM).

Reproducibility of GB2-Cy3 based image-based HTS assay.

Reproducibility of GB2-Cy3 based image-based HTS assay was validated by the cross-confirmation of 2 independent screenings performed in both cases (with or without phloretin). Suppression of GB2-Cy3 efflux using pPBS significantly enhanced the reproducibility of the HTS assay. Using our image-based HTS protocol, I then performed the pilot screening in duplicate by using 88 representative compounds from our in-house pDOS library in the absence or presence of phloretin to demonstrate the accuracy and reproducibility of our HTS assay. Two independent assay data in both cases (with or without phloretin) were utilized to confirm the assay reproducibility by showing their linearity. As shown in figure 2.14, I observed improved linearity between the 2 independent assay data when the image-based HTS was performed in PBS containing 20 μ M phloretin (pPBS). These results indicate that our phenotype-based screening system meets the criteria of a practical HTS assay for drug discovery owing to its robustness, reproducibility, and accuracy.

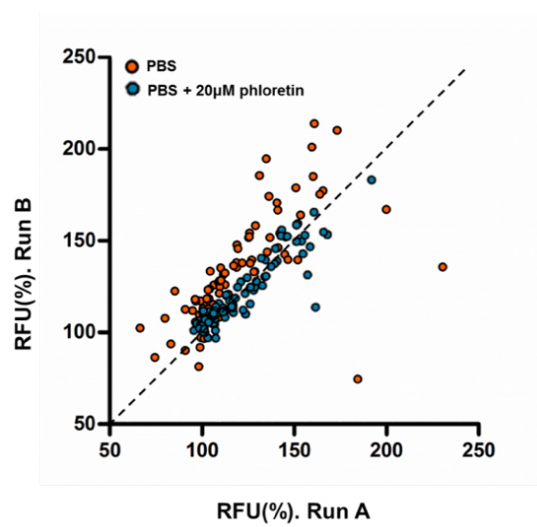


Figure 2.14. Linearity between the two independent assays in the presence or absence of 20 μM phloretin.

Construction of image-based HTS assay protocol. On the basis of this breakthrough in the bioimaging step, GB2-Cy3 can successfully be applied to the image-based HTS system for a large number of compounds as potential anti-diabetic agents in live cells with high reproducibility and accuracy (Figure 2.15).

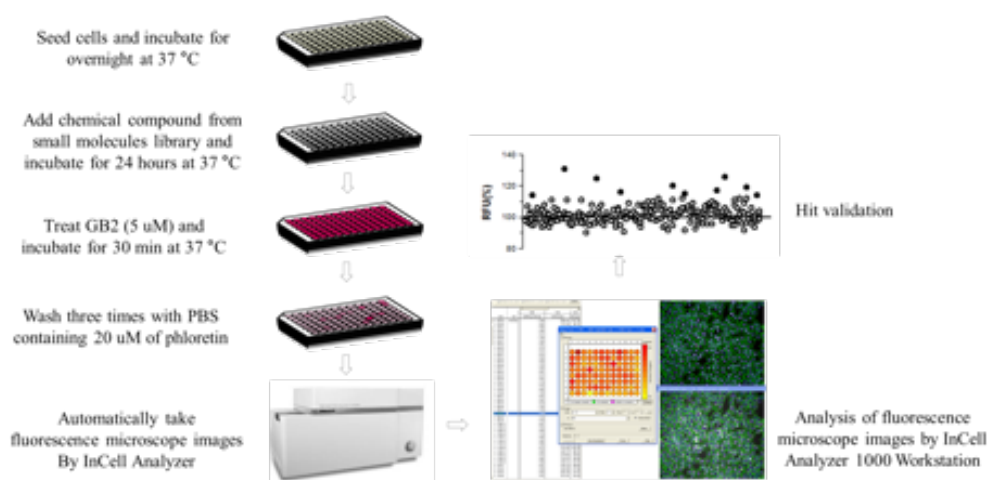


Figure 2.15. Screening protocol for image-based HTS using GB2-Cy3 to monitor cellular glucose uptake.

Comparison of GB2-Cy3 and 6-NBDG with our image-based HTS assay system. Unlike 2-NBDG and 6-NBDG, the brightness and minimal photobleaching of Cy3 in GB2-Cy3 ensures efficient detection of the fluorescence intensity in a short exposure time, which is essential for screening a large number of compounds in a high-throughput manner (Figure 2.16). These results indicate that GB2-Cy3-based phenotype-based screening system meets the criteria of a practical HTS assay for drug discovery owing to its robustness, reproducibility, and accuracy.

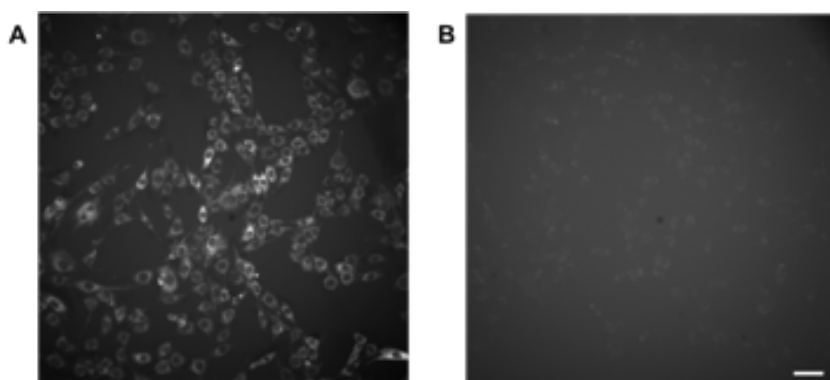


Figure 2.16. Comparison of GB2-Cy3 and 6-NBDG with our image-based HTS assay system. Cellular image of C2C12 cells after treatment with (A) GB2-Cy3 ($5 \mu\text{M}$) and (B) 6-NBDG ($20 \mu\text{M}$) for 30 min, followed by washing twice with PBS containing $20 \mu\text{M}$ phloretin. Fluorescence microscope images were captured using InCell Analyzer 2000 with same exposure time. The scale bar represents $20 \mu\text{m}$

Demonstration of the reliability of screening *via* virtual screening of DOS library. Finally, I performed virtual image-based HTS assay against 264 compounds from the pDOS library to identify bioactive small molecules that perturb the cellular glucose uptake. As shown in figure 2.17A and 2.17B, I successfully identified a series of small molecules that increased the cellular glucose uptake as observed by monitoring the fluorescence intensity of GB2-Cy3 in the cytoplasm. By the virtue of image-based screening, I was able to examine the assay results to eliminate false positives; some compounds enhanced the fluorescence intensity in the cytoplasm, but the cell morphology and staining pattern showed whether they affected the cell viability or other cellular processes (Figure 2.17B, P33H11 and Figure 2.17C).

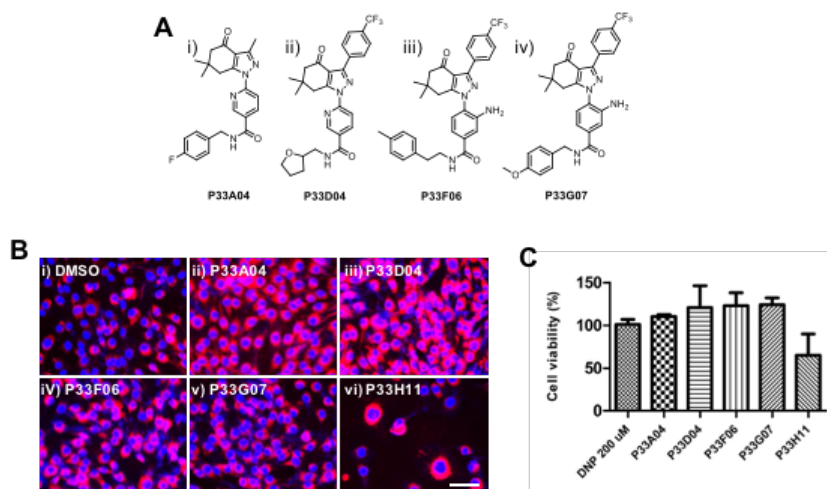


Figure 2.17. (A) Chemical structure of primary hit compounds. (B) Fluorescence images of C2C12 myoblasts. The scal bar represents 40 μ M. (C) Cell viability test of primary hit compounds in C2C12 myoblasts. Chemicals were treated for 24 hrs. Cell viability was normalized to DMSO control as 100%. Error bars indicate SEM.

Reliability of GB2-Cy3 based HTS assay. To confirm the reliability of our image-based HTS assay, 4 selected hit compounds were subjected to 2 orthogonal glucose uptake measurements using ^{14}C -labeled-2-deoxyglucose (^{14}C -2-DG) and enzyme-based uptake measurement assay of non-radiolabeled 2-deoxyglucose (2-DG). As shown in figure 2.18, the 4 hit compounds consistently showed enhanced cellular glucose uptake in both commercial methods, although these methods are not practically applicable in HTS systems. Therefore, I have clearly demonstrated the reliability of our image-based HTS system to identify novel candidates for treatment of glucose homeostasis-related diseases.

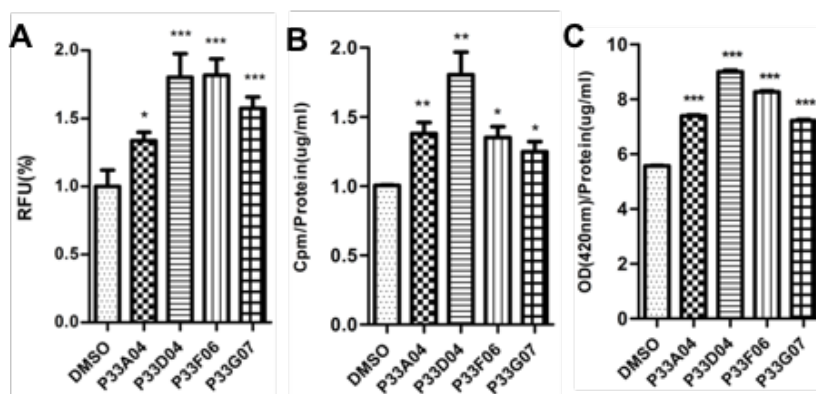


Figure 2.18. (A) RFU was determined from the ROI. C2C12 myoblasts were treated with DMSO and 4 of the primary hits, P33A04, P33D04, P33F06 and P33G07 (10 μM), for 24 h. (B) Radioisotope-based measurement of ^{14}C -labeled 2-DG uptake. Data are representative of three independent experiments. (C) Commercial enzyme-based measurement of cellular glucose uptake using non-radiolabeled 2-DG. Data are representative of three independent experiments. Error bars indicate SEM; *** $p < 0.0001$, ** $p < 0.005$, and * $p < 0.01$.

2.3.4. *In vivo* application of GB2-Cy3 in zebrafish larvae

GLUT-specific uptake of GB2-Cy3 in zebrafish larvae *in vivo* system.

Due to the immense complexity of organismic systems compared to cellular systems, the *in vivo* efficacy of drug candidates might be drastically different from their cellular or *in vitro* efficacies. Therefore, *in vivo* validation is one of the most important and inevitable steps in drug discovery. The zebrafish has been considered as a powerhouse animal model for drug discovery research, since it is an amenable organism for vertebrate-based compound screening and validation system. In this context, I envision the *in vivo* glucose-uptake monitoring system with GB2-Cy3 in zebrafish larvae. Recent study developed an *in vivo* glucose uptake screening system using 2-NBDG in zebrafish [36]. However, 2-NBDG cannot be considered as an ideal bioprobe for *in vivo* glucose uptake monitoring due to its high treatment concentration, low sensitivity, and fast photobleaching.

To establish a fluorescence-based monitoring system with GB2-Cy3 in zebrafish larvae, I first tested whether GB2-Cy3 uptake can be adequately measured time-dependently. 72 hours post fertilization (hpf) larvae were used because they allow drug testing in a 96 well plate format. In addition, GLUT transporter expression and glucose metabolism has been established at this stage of development [36]. I measured probe uptake into the zebrafish larval eye, because this is known to be a rich source of expression

of GLUTs [37] and the eye shape in 72 hpf larvae is amenable for image analysis of fluorescent intensity. I observed that 3 h incubation with GB2-Cy3 is appropriate for microscopic observation of uptake into the zebrafish larval eye (Figure 2.19).

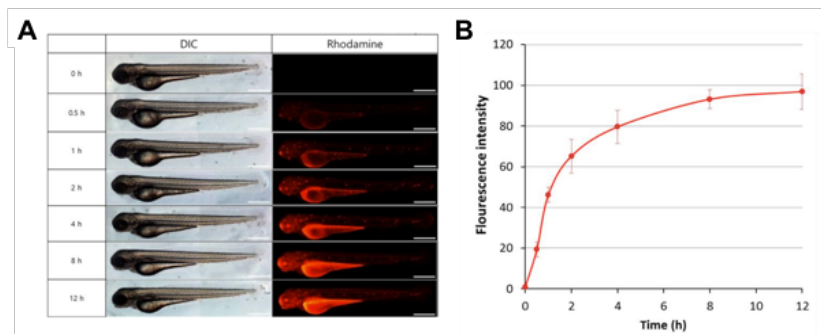


Figure 2.19. Time dependent uptake of GB2-Cy3 in zebrafish. Fluorescence intensity of GB2-Cy3 in zebrafish larval eye was dramatically increased within 2 h and saturated after 12 h upon treatment of GB2-Cy3 ($30 \mu\text{M}$) in E3 water. On the basis of this result, we concluded that 3 h incubation is optimum condition for GB2-Cy3 zebrafish imaging. The scale bar represents $500 \mu\text{m}$.

Dose-dependent uptake of GB2-Cy3 in zebrafish larvae *in vivo* system.

Next, I compared the dose-dependent *in vivo* uptake of GB2-Cy3 with that of 2-NBDG, using a fluorescent microplate reader, which would be advantageous for drug screening and validation. As shown in figure 2.20, GB2-Cy3 uptake can be observed at a dose of 5 μM and the fluorescence signal continued to increase dose-dependently up to 80 μM , with superb signal to noise ratio. In contrast, at least 600 μM concentration of 2-NBDG was required for optimal glucose uptake observation.

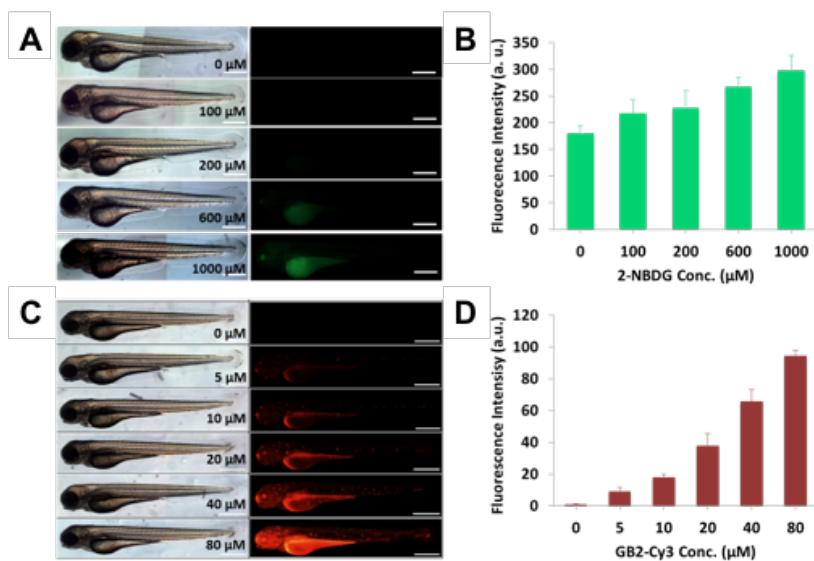


Figure 2.20. Dose dependent uptake of 2-NBDG in zebrafish (A) and its quantification data (B). Dose dependent uptake of Cy3-GB2 in zebrafish (C) and its quantification data (D). The scale bar represents 500 μm .

D-Glucose competition assay in zebrafish larvae *in vivo* system. With these results in hand, I tested whether *in vivo* uptake of GB2-Cy3 is GLUT specific or not. In the presence of 30 mM D-glucose, *in vivo* uptake of GB2-Cy3 was effectively competed out by D-glucose (Figure 2.21A and 2.21B). Furthermore, the GLUT inhibitor, 4,6-O-ethylidene- α -D-glucose (4,6-EDG), reduced GB2-Cy3 signal (Figure 2.21C and 2.21D), which provided the additional confirmation that GLUT activity is an important component of GB2-Cy3 uptake. Collectively, these results confirmed that *in vivo* uptake GB2-Cy3 in zebrafish larvae is controlled by GLUT-specific processes.

***In vivo* monitoring of glucose uptake regulators as anti-diabetic agents using GB2-Cy3.** As a final test to demonstrate that a GB2-Cy3-based assay system is a suitable for *in vivo* monitoring of glucose uptake regulators as anti-diabetic agents, I tested GB2-Cy3 uptake in zebrafish using glucose uptake enhancers with different mode of actions; (i) insulin-independent AMP kinase activator (ampkinone) [38] and (ii) insulin-independent PPAR γ agonist (rosiglitazone). Upon treatment with anti-diabetic agents having different modes of action, the increased uptake of glucose was measured by the fluorescence intensity of GB2-Cy3 in the zebrafish larval eye using fluorescence microscope and in the lysed zebrafish larvae using fluorescence microplate readers (Figure 2.22).

Furthermore, GB2-Cy3 can detect anti-diabetic drugs, an additional series of glucose uptake enhancers (insulin, GAPDS [39] and emodin) were shown to increase the *in vivo* uptake of GB-Cy3 (Figure 2.23). These results confirmed that GB2-Cy3 is an excellent bioprobe for *in vivo* monitoring of perturbed glucose uptake upon treatment with regulators of glucose homeostasis.

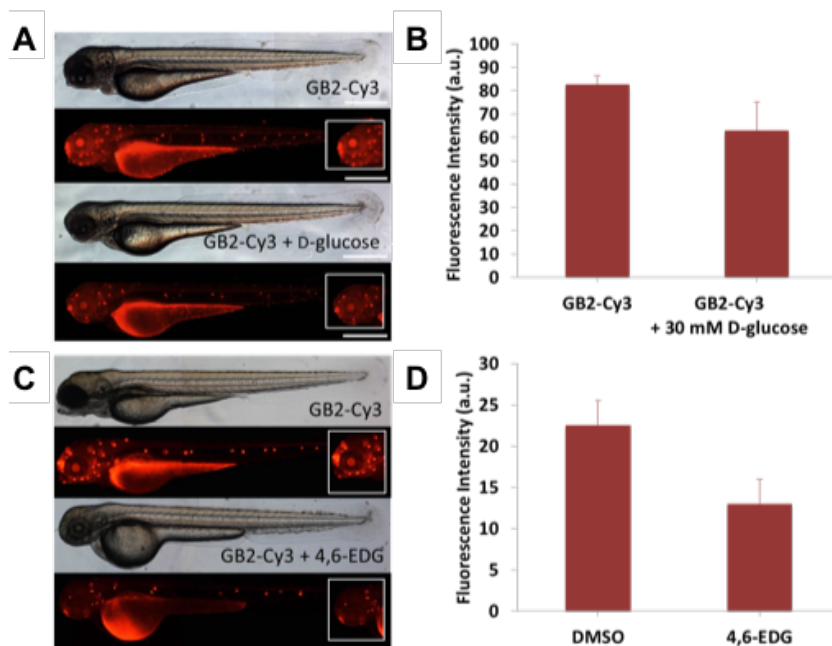


Figure 2.21. (A) Glucose competition assay of GB2-Cy3 in zebrafish. (B) Fluorescence intensities of zebrafish larval eyes. (C) GB2-Cy3 uptake was deteriorated by the GLUT inhibitor, 4,6-EDG (4,6-*O*-ethylidene- α -D-glucose, 2.5 mM), in zebrafish. (D) Fluorescence intensities of GB2-Cy3 uptake into the zebrafish larval eye. The scale bar represents 500 μ m.

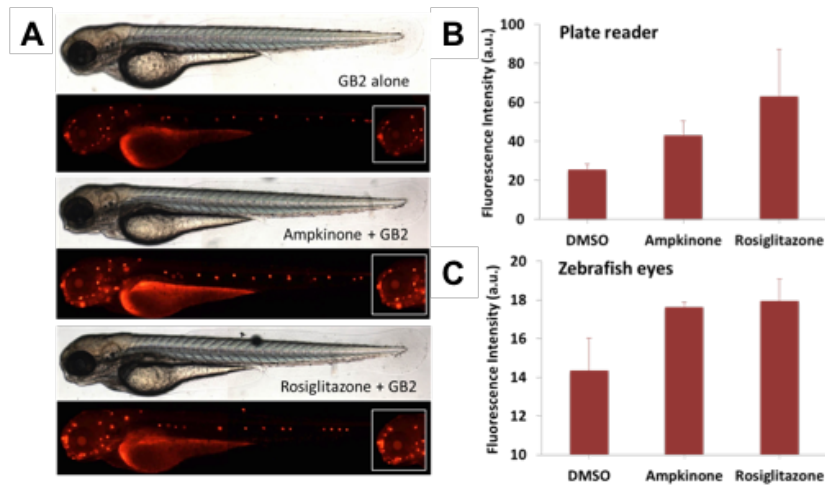


Figure 2.22. (A) GB2-Cy3 uptake increases in zebrafish after treatment with glucose uptake enhancers, ampkinone (10 μ M) and rosiglitazone (10 μ g/ml). (B) GB2-Cy3 uptake quantification of lysed larvae using a plate reader. (C) GB2-Cy3 uptake quantification by measuring fluorescence intensities of the zebrafish larval eye.

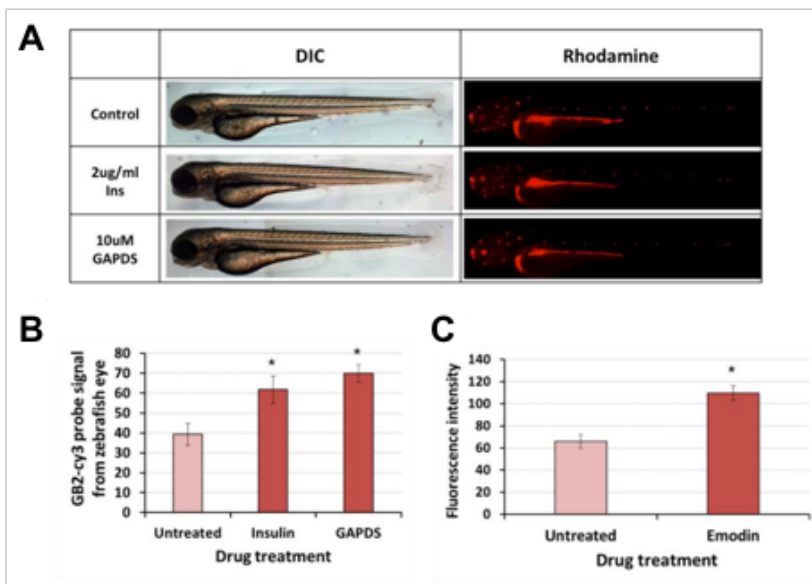


Figure 2.23. Glucose uptake enhancers (insulin, GAPDS and emodin) increased GB2-Cy3 uptake in zebrafish. 2.5 μ g/ml concentration of emodin was used for experiment.

2.4. Conclusion

In conclusion, mechanistic studies confirmed that the fluorescent glucose bioprobe GB2-Cy3 enters the cells mainly *via* GLUT-mediated translocation. Therefore, I demonstrated that GB2-Cy3 is a novel fluorescent glucose bioprobe to monitor the perturbation of cellular glucose uptake. Besides, conventional microscopy imaging revealed that the gradual decrease of fluorescent signal inside the cytoplasm after the GB3-Cy3 uptake. Based on the biophysical studies, I demonstrated that this phenomenon is caused by the efflux of non-phosphorylated GB2-Cy3 due to its reversed concentration after washing. Thereby, I effectively suppressed the efflux of GB2-Cy3 with phloretin—a transient and selective GLUT inhibitor. With this breakthrough, I could improve the reliability and accuracy of GB2-Cy3-based measurement of cellular glucose uptake in live cells. Moreover, I also demonstrated the importance of the molecular charge of glucose bioprobes on their uptake behavior. Cellular uptake of the positively charged glucose bioprobe is GLUT-specific, but that of negative charged and zwitterionic glucose bioprobes was not. This observation would be helpful for the design of new glucose bioprobes and the mechanistic understanding of GLUT-specific uptake of glucose bioprobes. Finally, I developed a novel image-based screening system to monitor the perturbation of cellular glucose uptake in a high-throughput

manner. Based on the mechanistic understanding about the biophysical behavior of GB2-Cy3, I effectively suppress the efflux of GB2-Cy3 during bioimaging by treatment with phloretin, a transient and selective GLUT inhibitor. With this breakthrough, I can develop the first image-based HTS system to monitor the glucose uptake in living cells with robustness, reproducibility, and accuracy. Considering the high demands for the discovery of novel therapeutic agents for the treatment of diabetes, obesity, and cancer, our image-based HTS system can provide a powerful tool to the biomedical research community. Furthermore, I anticipate the application of GB2-Cy3 based phenotypic assays in conjunction with other orthogonal assays, such as intracellular trafficking, signaling processes, and glucose utilization in living cells. I also confirmed GB2-Cy3 as a successful *in vivo* glucose tracer for GLUT-specific *in vivo* monitoring of glucose uptake in zebrafish model with significantly improved properties compared to the widely used glucose bioprobe, 2-NBDG. Considering the complexity of glucose homeostasis *in vivo*, I anticipate the application of GB2-Cy3 *in vivo* would provide a new insight for metabolic disease study and a valuable vertebrate-based screening system for anti-diabetes drug discovery.

2.5. References

1. Y. Minokoshi, C. R. Kahn and B. B. Kahn, *J. Biol. Chem.*, 2003, **278**, 33609–33612.
2. P. P. Hsu and D. M. Sabatini, *Cell* 2008, **134**, 703–707.
3. G. M. Reaven, *Diabetes* 1988, **37**, 1595–1607.
4. P. S. Conti, D. L. Lilien, K. Hawley, J. Keppler, S. T. Grafton and J. R. Bading, *Nucl. Med. Biol.* 1996, **23**, 717–735.
5. E. Nehlig, C. Wittendorp-Rechenmann and L. Dao, *J. Cereb. Blood Flow Metab.* 2004, **24**, 1004–1014.
6. A. Bullen, *Nat. Rev. Drug. Discovery.* 2008, **7**, 54–67.
7. L. Speizer, R. Haugland and H. Kutchai, *Biochim. Biophys. Acta.* 1985, **815**, 75–84.
8. W. H. Kim, J. Lee, D.-W. Jung and D. R. Williams, *Sensors* 2012, **12**, 5005.
9. K. Yoshioka, H. Takahashi, T. Homma, M. Saito, K. B. Oh, Y. Nemoto and H. Matsuoka, *Biochim. Biophys. Acta.* 1996, **1289**, 5–9.
10. K. Kleparnaik and F. Foret, *Anal. Chim. Acta.* 2013, **800**, 12–21.
11. V. Marx, *Nat. Methods* 2015, **12**, 187–190.
12. H. J. M. Handgraaf, F. P. R. Verbeek, Q. R. J. G. Tummers, L. S. F. Boogerd, C. J. H. van de Velde, A. L. Vahrmeijer and K. N. Gaarenstroom, *Gynecol. Oncol.* 2014, **135**, 606–613.
13. H. Y. Lee, J. J. Lee, J. Park and S. B. Park, *Chem. – Eur. J.* 2011, **17**, 143–150.
14. F. Zanella, J. B. Lrens and W. Link, *Trends Biotechnol.*, 2010, **28**, 237–245.

15. D. W. Jung, H. H. Ha, X. Zheng, Y. T. Chang and D. R. Williams, *Mol. BioSyst.*, 2011, **7**, 346–358.
16. K. Yoshioka, H. Takahashi, T. Homma, M. Saito, K. B. Oh, Y. Nemoto and H. Matsuoka, *Biochim. Biophys. Acta.* 1996, **1289**, 5–9.
17. M. Zhang, Z. Zhang, D. Blessington, H. Li, T. M. Busch, V. Madrak, J. Miles, B. Chance, J. D. Glickson and G. Zheng, *Bioconjugate Chem.* 2003, **14**, 709–714.
18. Y. Ye, S. Bloch and S. Achilefu, *J. Am. Chem. Soc.* 2004, **126**, 7740–7741.
19. Z. Cheng, J. Levi, Z. Xiong, O. Gheysens, S. Keren, X. Chen and S. S. Gambhir, *Bioconjugate Chem.* 2006, **17**, 662–669.
20. J. Park, H. Y. Lee, M. H. Cho and S. B. Park, *Angew. Chem., Int. Ed.* 2007, **46**, 2018–2022.
21. Y. S. Tian, H. Y. Lee, C. S. Lim, J. Park, H. M. Kim, Y.N.Shin, E. S. Kim, H. J. Jeon, S. B. Park and B. R. Cho, *Angew. Chem., Int. Ed.* 2009, **48**, 8027–8031.
22. M. W. Louie, H. W. Liu, M. H. C. Lam, Y. W. Lamand, K. K. W. Lo, *Chem. – Eur. J.* 2011, **17**, 8304–8308.
23. M. Vendrell, A. Samanta, S. W. Yun and Y. T. Chang, *Org. Biomol. Chem.* 2011, **9**, 4760–4762.
24. D. Deng, P. Sun, C. Yan, M. Ke, X. Jiang, L. Xiong, W. Ren, K. Hirata, M. Yamamoto, S. Fan and N. Yan, *Nature* 2015, **526**, 391–396.
25. S. Huang and M. P. Czech, *Cell Metab.* 2007, **5**, 237–252.
26. B. Thorens, M. J. Charron and H. F. Lodish, *Diabetes Care* 1990, **13**, 209–218.
27. C. Harding, J. Heuser and P. Stahl, *J. Cell Biol.* 1983, **97**, 329–339.

28. D. L. Dipietro, C. Sharma and S. Weinhouse, *Biochemistry* 1962, **1**, 455–462.
29. M. Hassanein, B. Weidow, E. Koehler, N. Bakane, S. Garbett, Y. Shyr and V. Quaranta, *Mol. Imaging Biol.* 2011, **13**, 840–852.
30. H. Terada, *Environ. Health Perspect.* 1990, **87**, 213–218.
31. G. F. Fuhrmann, S. Dervedde and G. Frenking, *Biochim. Biophys. Acta.* 1992, **1110**, 105–111.
32. H. S. Choi, K. Nasr, S. Alyabyev, D. Feith, J. H. Lee, S. H. Kim, Y. Ashitate, H. Hyun, G. Patonay, L. Streckowski, M. Henary and J. V. Frangioni, *Angew. Chem. Int. Ed.* 2011, **50**, 6258–6263.
33. H. S. Choi, S. L. Gibbs, J. H. Lee, S. H. Kim, Y. Ashitate, F. Liu, H. Hyun, G. Park, Y. Xie, S. Bae, M. Henary and J. V. Frangioni, *Nat. Biotechnol.* 2013, **31**, 148–153.
34. E. Kim, K. S. Yang, R. J. Giedta and R. Weissleder, *Chem. Commun.* 2014, **50**, 4504–4507.
35. L. I. Markova, I. A. Fedyunyayeva, Y. A. Povrozin, O. M. Semenova, S. U. Khabuseva, E. A. Terpetschnig and L. D. Patsenker, *Dyes Pigm.* 2013, **96**, 535–546.
36. J. Lee, D. W. Jung, W. H. Kim, J. I. Um, S. H. Yim, W. K. Oh and D. R. Williams, *ACS Chem. Biol.* 2013, **8**, 1803–1814.
37. Y. C. Tseng, R. D. Chen, J. R. Lee, S. T. Liu, S. J. Lee and P. P. Hwang, *Am. J. Physiol. Regul., Integr. Comp. Physiol.* 2009, **297**, R275–R290.
38. S. Oh, S. J. Kim, J. H. Hwang, H. Y. Lee, M. J. Ryu, J. Park, S. J. Kim, Y. S. Jo, Y. K. Kim, C. H. Lee, K. R. Kweon, M. Shong and S. B. Park, *J. Med. Chem.* 2010, **53**, 7405–7413.
39. J. Min, Y. K. Kim, P. G. Cipriani, M. Kang, S. M. Khersonsky, D. P. Walsh, J. Y. Lee, S. Niessen, J. R. Yates, K. Gunsalus, F. Piano and Y. T. Chang, *Nat. Chem. Biol.* 2007, **3**, 55–59.

Chapter 3. Development of novel real-time assay system for monitoring dynamic GLUT4 trafficking in live cells

1.1. Introduction

Glucose transporter 4 (GLUT4) is one of the most well-known membrane protein that its biological function is determined by the regulation of insulin [1]. The physiological role of insulin is to regulate glucose homeostasis by controlling GLUT4 trafficking and glucose uptake [2]. Spatial and temporal regulation of GLUT4 trafficking is precisely controlled by insulin to regulate glucose uptake into cells [3]. There are many regulatory elements that determine GLUT4 trafficking to enhance glucose uptake in respond to insulin action. GLUT4 are formed and accumulated in GLUT4-sorting vesicles (GSVs) in basal, and rapidly translocate to cell surface, tethers and fuses with plasma membrane (PM) (Figure 1.4). Dysfunction of insulin-stimulated GLUT4 translocation (ISGT) is closely related with insulin resistance, resulting type 2 diabetes [4, 5]. In this regard, there have been many efforts to understand the mechanism of insulin signaling to stimulate the translocation of GLUT4 to the PM.

Conventional methods determine GLUT4 translocation by immunoblotting after membrane fractionation [6] or by immunofluorescence imaging of epitope-fused GLUT4 (e.g. Myc or HA tag) [7, 8]. However, these techniques lack of robustness to monitor dynamic regulation of GLUT4 trafficking in real-time. Recent high-resolution live-cell imaging using total internal reflection fluorescence microscopy (TIRFM) have been successfully applied to study GLUT4 recycling processes that take place near the PM [9, 10, 11, 12]. However, most of studies using TIRF microscopy are restricted to the investigation of GLUT4 trafficking events near the PM in a thin TIRF zone such as tethering and fusion. Thereby, it is still unclear and debating how insulin regulates GLUT4 trafficking between intracellular compartments such as trans-golgi network (TGN), endosomes, and GSVs. To solve these questions, a novel imaging technique that probes intracellular trafficking of GLUT4 with spatiotemporal resolution in living cell is needed.

Fluorescence imaging techniques based on protein tags are the most versatile method for investigating spatiotemporal movement of protein of interests [13]. In these techniques, a protein of interest is genetically fused to a protein tag, and specifically labeled at desired time and location by adding its probes in living cells. To date, various kind of protein tag are reported, including SNAP, CLIP, Halo, TMP and FAPs [14]. Among them, SNAP tag is a mutant of O⁶-alkylguanine-DNA alkyltransferase (AGT) that promotes bio-orthogonal reaction with O⁶-benzylguanine (BG) derivatives

with superior reaction kinetics [15]. Using the specific reactivity of SNAP tag with BG, fluorophore-linked BG derivatives are widely used to visualize various biological processes such as expression level, subcellular localization, and protein-protein interaction of protein of interests [16-19]. Especially, SNAP tag attracted interest due to its variety kinds of fluorescent probes including membrane-impermeable probes and fluorogenic probes with large variation of excitation and emission wave lengths.

In the present study, I developed a novel real-time and quantitative monitoring system of GLUT4 trafficking in living cells. I developed EGFP-GLUT4-SNAP which enables the spatiotemporal analysis of GLUT4 trafficking in living cells. EGFP-GLUT4-SNAP was carefully designed to observe the translocation of GLUT4 to the PM. Specifically, I exposed the SNAP tag to the outside of the cell when the GLUT4 moves to the PM, and introduced membrane-impermeable SNAP tag probes. Therefore, EGFP-GLUT4-SNAP is only labeled with its fluorescence when the GLUT4 moves to the PM, thereby we could successfully observe GLUT4 translocation to the PM in a real-time and quantitative manner. With this novel GLUT4 imaging system, I also could observe the real-time intracellular movement of GLUT4. As a result, I demonstrated the recently suggested model of insulin-stimulated GLUT4 translocation (ISGT) by proving the formation of endosomal recycling pool in the vicinity of the PM following the continued insulin stimulation.

3.2. Materials and methods

Cell culture

CHO-K1 cells and 3T3-L1 cells (mouse embryonic fibroblasts) were obtained from ATCC [American Type Culture Collection]. CHO-K1 cells were maintained in RPMI containing 10% fetal bovine serum (FBS) [GIBCO] and 1% antibiotic-antimycotic solution at 37 °C in an atmosphere of 5% CO₂. 3T3-L1 cells were maintained in DMEM containing 10% heat-inactivated bovine calf serum (BCS) [GIBCO] and 1% antibiotic-antimycotic solution at 37 °C in an atmosphere of 5% CO₂. After reaching confluence, 3T3-L1 cells were differentiated by treating the cells with 1 μM dexamethasone, 10 μM rosiglitazone, and 5 μg/ml insulin in DMEM containing 10% FBS for 2 days, and the cell culture was subsequently maintained by substituting the medium with fresh DMEM containing 10% FBS and 5 μg/ml insulin.

DNA cloning

cDNA of GLUT4 is obtained from pcDNA3.2/v5-DEST hGlut4 plasmid from Addgene. pDiaplayTM vector was obtained from Invitrogen. pSNAP_f vector was obtained from NEB. EGFP-C2 vector was obtained from Addgene. To construct pGLUT4-TM, GLUT4 gene was amplified by PCR from the pcDNA3.2/v5-DEST hGlut4 using forward primer 5'-CTT AAG CTT ATG CGG TCG GGC TTC-3' (Hind III site) and reverse primer 5'-

TAT TCC CGG GAG TCG TTC TCA TC-3' (Xma I site). For the PCR amplification, 200 μ M of dNTP mixture, 0.2 μ M of forward primer, 0.2 μ M of reverse primer, 10 ng of pcDNA3.2/v5-DEST hGlut4, 1.25 Units of Pfu polymerase [Beams bio] and 5 μ l of 10X reaction buffer [Beams bio] were dissolved in 50 μ l of ddH₂O. Polymerase chain reaction was done using touch down and hot-start method. The PCR product was purified using QIAquick PCR purification kit [Qiagen]. The PCR product and pDisplayTM vector [Invitrogen] were digested with Hind III [Beams bio] and Xma I [Beams bio] at 37°C for 12 hrs. After DNA digestion reaction, 1 μ l of CIAP was added to vector sample and incubated at 37°C for 1 hr. Reaction products were separated by gel electrophoresis using 1% agarose gel, and extract pure DNA using QIAquick Gel Extraction kit [Qiagen]. The resulting insert and vector were ligated with T4 ligase [NEB] at 16°C for 12 hrs, and transformed to competent cell by heat shock at 42°C for 30 sec. After the incubation of competent cells (DH5 α) at 37°C for 2 hrs, spread cells to LB agar plate containing ampicillin. Colony was inoculated to LB medium containing ampicillin, and plasmid DNA was purified by QIAprep Miniprep kit [Qiagen]. To construct pGLUT4-TM-SNAP, pGLUT4-TM was amplified using forward primer 5'-GGA ATT CGC TAG CTA TGC CGT CGG-3' (Nhe I site) and reverse primer 5'-CCG GAA TTC ACG TGG CTT CTT CTG CC-3' (EcoR I site). After PCR amplification, PCR product and pSNAP_f vector were double digested (Nhe

I and EcoR I) and ligated using the previously explained methods. After transformation to competent cell (DH5 α), pGLUT4-TM-SNAP was purified by QIAprep Miniprep kit [Qiagen]. To construct pEGFP-GLUT4-SNAP, pGLUT4-TM-SNAP was amplified using forward primer 5'-CCA ACA CAA GCT TTA TGC CGT CGG-3' (Hind III site) and reverse primer 5'-CCA AC AGG TAC CTT AAT TAA CCT CGA GT-3' (Kpn I site). After PCR amplification, PCR product and pEGFP-C2 vector were double digested (Hind III and Kpn I) and ligated using the previously explained methods. All the plasmid products were validated by sequencing.

Plasmid transfection

Cells were seeded on cover glass bottom dish at a density of 2×10^4 cells/ml. After 24 hrs, medium was exchanged to fresh medium containing serum without antibiotic-antimycotic. Transfection was performed using Lipofectamine LTX [Invitrogen] followed by manufacturer's protocol. Briefly, 2.5 μ g of plasmid DNA (pEGFP-GLUT4-SNAP) and 3.9 μ l of Plus reagent in 125 μ l of Opti-MEM [Gibco] was mixed with 5.9 μ l of LTX reagent in 125 μ l of Opti-MEM. After incubate mixture solution in room temperature for 5 min, 250 μ l of mixture solution was added into well (6 well plate). After 12 hrs, medium was washed out and subsequent experiments were performed.

In-gel fluorescence analysis

CHO-K1 cells were transfected with pEGFP-GLUT-SNAP or pEGFP-C2 using Lipofectamine LTX [Invitrogen]. After 12 hrs, cells were lysed with RIPA buffer containing 1x phosphatase inhibitor cocktail [Roche]. Protein concentration of whole lysates was adjusted to 3 mg/ml in 100 μ l of RIPA buffer. For 100 μ l of cell lysates, 1 μ M of SNAPsurface 649 was added and incubated at 37 °C. After 30 min, make 1x SDS sample by adding 1/4 volume of 5x SDS buffer into lysate. Whole proteome was separated by SDS-PAGE and analyzed by fluorescence scanning equipment [Typhoon, GE healthcare].

Fluorescence microscopy imaging

After transfection of cells with pEGFP-GLUT4-SNAP using Lipofectamine LTX according to manufacturer's method, fluorescence microscopy imaging was performed using DeltaVision imaging system [GE Healthcare] equipped with 60x objective lenses of Olympus IX-71 inverted microscope. Four-color standard filter set was used for fluorescence imaging. FITC channel; excitation with 475 ± 14 nm and emission with 525 ± 24 nm. TIRTC channel; excitation with 542 ± 14 nm and emission with 597 ± 23 nm. Cy5 channel; excitation with 632 ± 11 nm and emission with 679 ± 17 nm. Live cell imaging was performed in chamber maintaining 37 °C and atmosphere with 5% CO₂.

Immunofluorescence imaging

CHO-K1 cells were transfected with pEGFP-GLUT-SNAP using Lipofectamine LTX [Invitrogen] and incubated for 12 hrs. After wash out medium, 1 μ M of SNAPsurface 649 was treated to cells with 170 nM of insulin or not and incubated for 30 min at 37 °C incubator. After wash out medium with PBS, cells were fixed with 3.7 % paraformaldehyde for 15 min at room temperature and washed out. Fixed cells were blocked with 4% BSA in PBS for 1 hr at room temperature. Primary antibody (EEA-1, 1:500 in 1% BSA-PBS) was incubated overnight at 4 °C. After washing with PBS for three times, cells were incubated with TRITC-conjugated secondary antibody (1:500 in 1% BSA-PBS) for 2 hrs at room temperature. After washing with PBS for 5 times, nucleus was stained with Hoechst 33342 [Thermo Scientific] and washed out. Fluorescence microscopy imaging was performed using DeltaVision imaging system [GE Healthcare] equipped with 60x objective lenses of Olympus IX-71 inverted microscope. Temperature was maintained at 23 °C.

High-content image analysis

Fluorescence single cell images were divided into 4 cell compartments; whole cell, cell center, plasma membrane and perinuclear region. Within each cell compartment, GLUT4 vesicles were detected from EGFP and SNAP tag-labeled channels. Single vesicles are analyzed to measure the number, area and intensity. Phenotypic parameters are analyzed depend on

time and localization to exclude the information about spatiotemporal GLUT4 trafficking.

Statistical analysis

The results are shown as means \pm SEM. The student's t-test was used for comparison between experimental groups (Microsoft Excel). P values of <0.05 were considered significant.

3.3. Results and discussion

Construction of EGFP-GLUT4-SNAP. To study spatiotemporal trafficking of GLUT4 in living cells, I constructed EGFP-GLUT4-SNAP by genetically encoding EGFP and SNAP tag into GLUT4. First of all, to achieve the visualization of GLUT4 translocation to the PM, I designed to fuse SNAP tag to the C-terminal of GLUT4 and to expose SNAP tag toward the extracellular side of cells when the GLUT4 translocate to the PM (Figure 3.1) [20]. With this construct, membrane-impermeable SNAP tag probe (Figure 3.2B) would be selectively labeled with EGFP-GLUT4-SNAP at the PM, thereby I could monitor the translocation of GLUT4 to the PM. I also fused EGFP to the N-terminal of GLUT4 to visualize the endogenous expression level and overall distribution of GLUT4 (Figure 3.1).

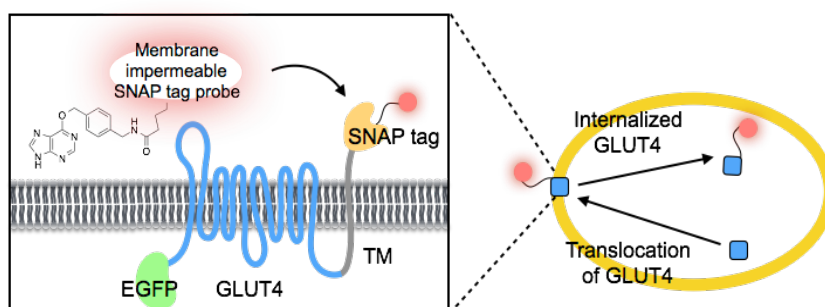


Figure 3.1. Schematic diagram of EGFP-GLUT4-SNAP

After the plasmid construction, I performed transfection of pEGFP-GLUT4-SNAP into mammalian cells and confirmed the expression of EGFP-GLUT4-SNAP. First of all, I transfected pEGFP-GLUT4-SNAP in CHO-K1 cells, then the cell lysates were incubated with SNAP tag probes. Next, I performed in-gel fluorescence analysis (Figure 3.2A). As shown in figure 3.2A, I confirmed the expression of EGFP-GLUT4-SNAP at the expected molecular weight (~86 kDa). I also confirmed the bio-orthogonal reaction of EGFP-GLUT4-SNAP with SNAP tag probe (SNAPsurface 649) in cell lysates.

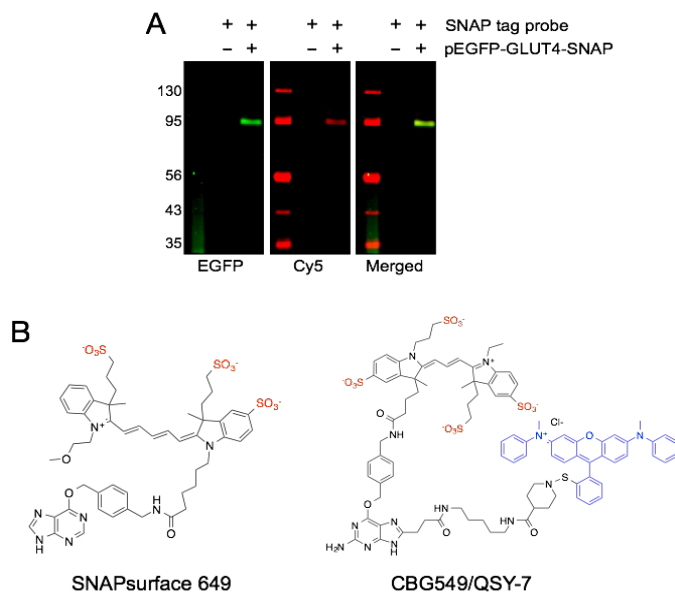


Figure 3.2. (A) In-gel fluorescence analysis of EGFP-GLUT4-SNAP expressing cells after labeling with SNAP tag probes. Whole-cell lysates of EGFP-GLUT4-SNAP expressing CHO-K1 cells were incubated with 1 μ M of SNAPsurface 649 for 1 hour and resolved on SDS-PAGE. In-gel fluorescence at green (488 nm excitation, 532 nm emission) and red (excitation, emission) were analyzed. (B) Structures of membrane-impermeable SNAP tag probes.

Moreover, I transfected pEGFP-GLUT4-SNAP or pEGFP in CHO-K1 cells, then incubated with membrane-impermeable SNAP tag probe (SNAPsurface 649, Figure 3.2B) in live cells for 1 hour. After washing, I observed the cells with fluorescence microscopy in live cells. As shown in figure 3.3, cells transfected with pEGFP-GLUT4-SNAP showed fluorescence from Cy5—the fluorophore which is linked to SNAPsurface 649. These data indicate that SNAP tag of EGFP-GLUT4-SNAP is exposed to the extracellular side of cells, and reacts with its probes as I initially designated. Comparing with the cells transfected with pEGFP, I convinced that the reaction between EGFP-GLUT4-SNAP and SNAP tag probe is bio-orthogonal without background signals (Figure 3.3).

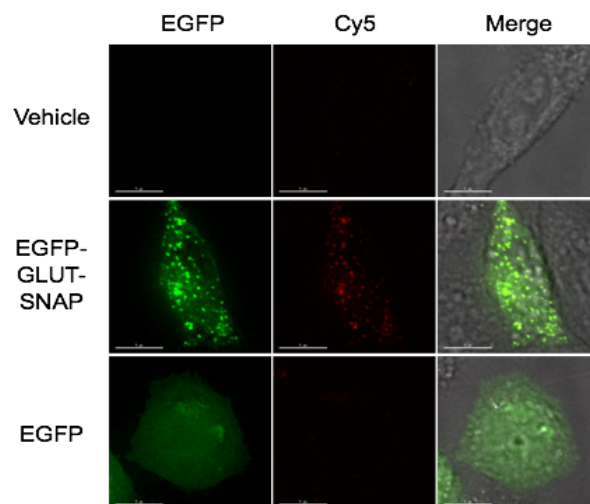


Figure 3.3. Live cell fluorescence imaging of EGFP-GLUT4-SNAP expressing cells after labeling with SNAP tag probes. EGFP-GLUT4-SNAP expressing or EGFP expressing CHO-K1 cells were incubated with 1 μ M of SNAPsurface 649 for 1 hour. After wash out media, fluorescence images were taken in live cells using DeltaVision imaging system. Scale bars indicate 5 μ m.

Taken together, I successfully constructed EGFP-GLUT4-SNAP, a novel imaging system for monitoring GLUT4 in living cells.

Quantitative monitoring of GLUT4 translocation to the PM. Next, I demonstrated the utility of our system for quantitative monitoring of GLUT4 translocation to the PM in living cells. Insulin is well known about its dose-dependent effect on GLUT4 translocation to the PM [2]. Therefore, I treated cells with different concentration of insulin, and incubated with membrane-impermeable SNAP tag probe (SNAPsurface 649). After incubation, cells were washed and imaged with fluorescence microscopy (Figure 3.4A). As shown in figure 3.4B, SNAP tag-labeling increased in an insulin-dependent manner. This data indicates that insulin stimulates the translocation of EGFP-GLUT4-SNAP to the PM. Furthermore, I could quantitatively determine the translocation of GLUT4 by measuring the fluorescence intensities of each cells (Figure 3.5). Taken together, EGFP-GLUT4-SNAP is a novel imaging system that enables quantitative monitoring of GLUT4 translocation to the PM in living cells.

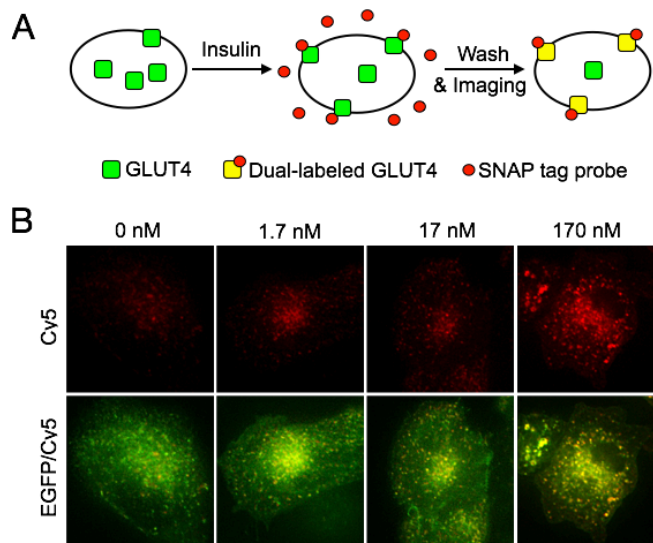


Figure 3.4. Quantitative monitoring of GLUT4 translocation to the PM. (A) Schematic diagram. (B) Insulin dose-dependently increased SNAP tag labeling. EGFP-GLUT4-SNAP expressing CHO-K1 cells are stimulated with insulin (0, 1.7, 17, 170 nM) and incubated with 1 μ M of SNAPsurface 649 for 1 hour. After wash out media, fluorescence images were taken in live cells using DeltaVision imaging system. SNAP tag labeling; Cy5 ex/em channel, EGFP; EGFP ex/em channel.

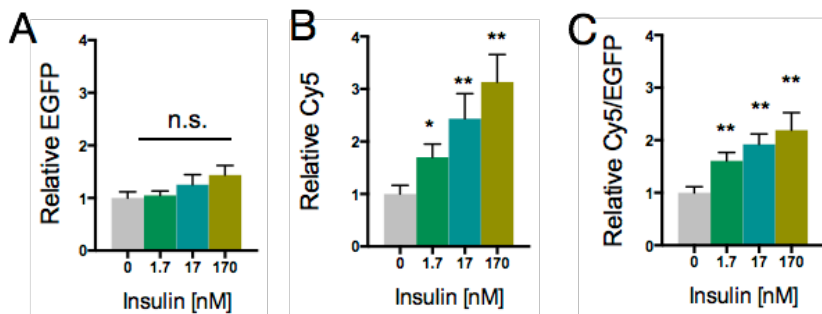


Figure 3.5. (A) Relative fluorescence intensities of cell images from EGFP channel. (B) Relative fluorescence intensities of cell images from Cy5 channel. (C) Calculated relative Cy5/EGFP fluorescence intensities. Error bars are SEM. * $P < 0.05$, ** $P < 0.01$ versus 0 nM insulin treated groups.

Real-time monitoring of GLUT4 translocation to the PM. Nonetheless, non-fluorogenic SNAP tag probe is not suitable for the real-time kinetic study of GLUT4 translocation to the PM due to the necessary of washing step. Therefore, I introduced a fluorogenic and membrane-impermeable SNAP tag probe, CBG549/QSY-7 into EGFP-GLUT4-SNAP imaging system. CBG549/QSY-7 is composed of SNAP tag substrate (BG), a membrane-impermeable fluorophore and quencher of its fluorophore (Figure 3.2B). Therefore, CBG549/QSY-7 reacts with SNAP tag and turned-on only when EGFP-GLUT4-SNAP translocate to the PM and enables the real-time and quantitative imaging of GLUT4 translocation (Figure 3.6A). Using this system, I analyzed the kinetics of insulin action on GLUT4 translocation in living cells. EGFP-GLUT4-SNAP expressing cells were incubated with insulin and CBG549/QSY-7 together, then fluorescence images were taken at 1 min intervals for 30 min. As shown in figure 3.6B, I observed rapidly increasing fluorescence in the cells which are stimulated with insulin compared with basal cells.

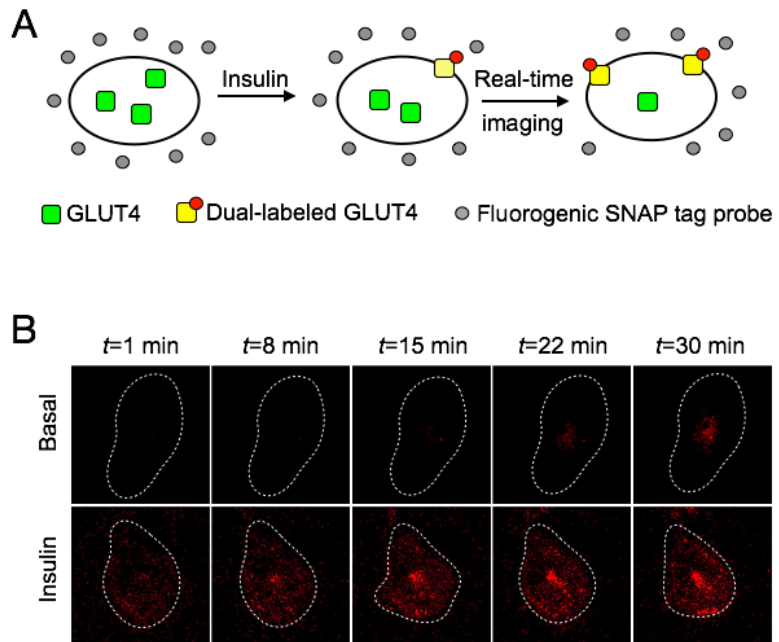
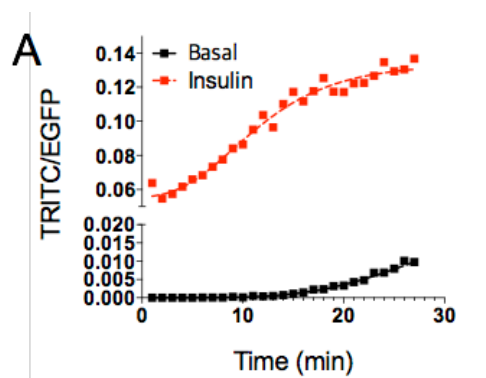


Figure 3.6. Real-time imaging of GLUT4 translocation in live cells. (A) Schematic diagram of real-time imaging using fluorogenic and membrane-impermeable SNAP tag probes. (B) Time-lapse live cell images in the presence of 1 μ M of CBG549/QSY-7.

Furthermore, fluorescence intensity of insulin-stimulated cells reached saturation in 20 min (Figure 3.7A and 3.7B), showing consistency with previously reported data [21, 22]. In conclusion, I convinced that the conjunction of EGFP-GLUT4-SNAP and fluorogenic and membrane-impermeable SNAP tag probe provides us a useful real-time imaging system for monitoring GLUT4 translocation to the PM.



B

<i>t</i>	Basal	Insulin
1 min	0.0000	0.0639
8 min	0.0001	0.0776
15 min	0.0011	0.1172
22 min	0.0048	0.1225
30 min	0.0132	0.1493

Figure 3.7. (A) Calculated TRITC/EGFP fluorescence intensities from cell images from TRITC channel (Figure 3.6B) and EGFP channel. (B) Fluorescence intensities at each time point.

Verification of insulin action on the control of intracellular GLUT4 distribution. Although insulin obviously increases the translocation of GLUT4 to the PM, where insulin acts to modulate intracellular GLUT4 trafficking is still controversial. There have been two controversial models, ‘Static retention model’ and ‘Dynamic equilibrium model’ (Figure 3.8). ‘Static retention model’ (Model I) claims that insulin induces the release of GSVs from internally sequestered cytoplasmic pool [23]. In contrast, ‘Dynamic equilibrium model’ (Model II) claims that tethering and fusion of GLUT4 at the PM are the major insulin actions [24]. Recently, series of studies using TIRF microscopy revealed a dual-mode of insulin action to control GLUT4 vesicle exocytosis (Model III) which unites the static retention model and dynamic equilibrium model [11]; (i) Insulin accelerates the burst translocation of GSVs from the sequestered internal pool to the PM at early stage of insulin stimulation. Followed by insulin burst, (ii) insulin continuously enhances the GLUT4 translocation to the PM by accelerating the tethering and fusion of GLUT4 within endosomal compartments near the PM. These studies proved the model by investigating the tethering and fusion events of GLUT4 at the PM due to intrinsic limitation of TIRF microscopy. Therefore, there is no clear evidence of how insulin regulates GSVs and endosomal compartments to translocate GLUT4 into the PM.

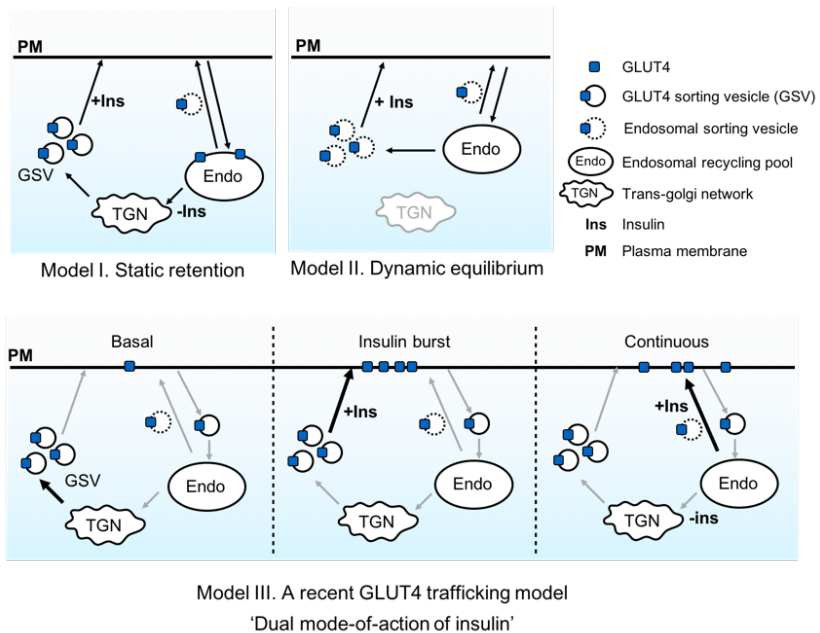


Figure 3.8. Models of Insulin-stimulated GLUT4 translocation (ISGT). In the static retention model, insulin stimulates burst translocation of internally sequestered GSV immediately to the PM. In the dynamic equilibrium model, insulin increases GLUT4 at the PM by inducing translocation of GLUT4 from endosomal recycling pool to the PM. A recently suggested model (Model III) united controversial two models. At initial stage of insulin stimulation, insulin promotes burst translocation of sequestered GSV at perinuclear region to the PM. Continuously, insulin enhances the GLUT4 translocation to the PM by accelerating the tethering and fusion of GLUT4 within endosomal recycling pool near the PM.

Herein, I investigated the recently proposed model about ISGT by visualizing intracellular distribution of GLUT4 after insulin stimulation. I could observe the internalized GLUT4 in perinuclear region or in the vicinity of PM by tracing SNAP-labeled EGFP-GLUT4-SNAP. Therefore, I expected that our system can be utilized to reveal the insulin action on spatiotemporal GLUT4 regulation including translocation to the PM, internalization by endocytosis, and intracellular distribution after the internalization.

First of all, I confirmed that GLUT4 are mainly localized in perinuclear region of cell which is assumed as TGN—the internal recycling site of GSVs in basal state. Then, I continuously monitored dynamic trafficking of GLUT4 by real-time imaging after insulin stimulation or not (Figure 3.9). In basal state, I observed that GLUT4 continuously moves back and forth between the PM and perinuclear region (Figure 3.9A). After insulin stimulation, GLUT4 immediately started to translocate to the vicinity of the PM (Figure 3.9B., $t=6$ min). After 15 min, I observed the formation of distinct intracellular compartment of GLUT4 in the vicinity of the PM (Figure 3.9B., $t=16$ min) which are assumed as endosomal recycling pool based on the preceding studies [11, 12, 25].

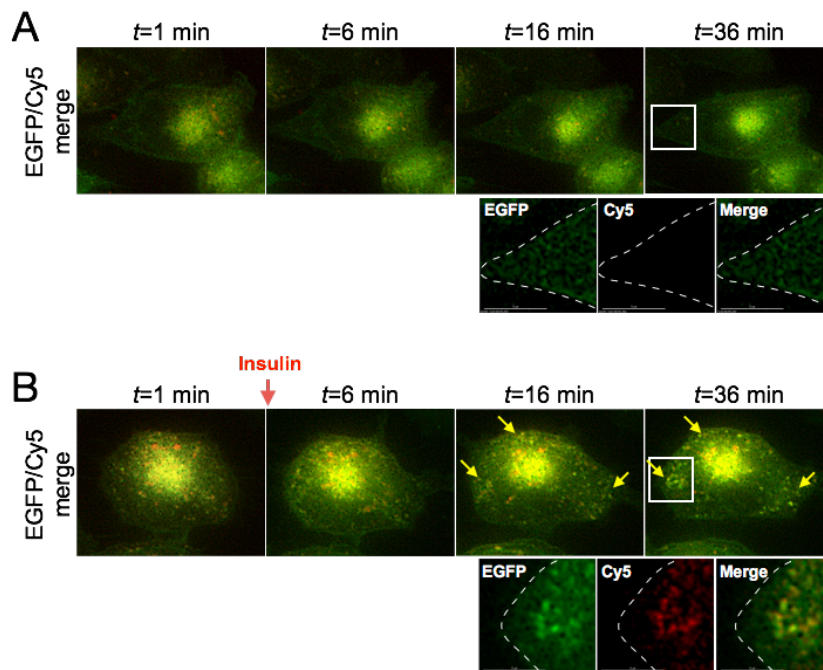


Figure 3.9. Insulin actions on the control of intracellular distribution of GLUT4. Time-lapse fluorescence images after stimulated with insulin or not. EGFP-GLUT4-SNAP expressing CHO-K1 cells are labeled with $1 \mu\text{M}$ of SNAPsurface 649 in basal condition. After wash out media, cells were stimulated with insulin or not. Time-lapse fluorescence images were taken every minute with Cy5 and EGFP channels. Yellow arrows indicate the formation of GLUT4 clusters near the PM. White boxes indicate enlarged images below. Scale bars, $5 \mu\text{m}$.

To demonstrate this idea, I performed immunofluorescence imaging with an early endosome marker (EEA1). As shown in figure 3.10, I confirmed the colocalization of early endosome with insulin-induced intracellular compartment of GLUT4 near the PM. From these data, I concluded that insulin has dual mode-of-action to control GLUT4 translocation; (i) The burst translocation of GSVs from internally sequestered pool to the PM at early stage, and (ii) The transition of GLUT traffic from static retention to dynamic equilibrium by enhancing the formation of endosomal pool of cycling pool near the PM. Overall, I convinced that EGFP-GLUT4-SNAP is a novel system for monitoring intracellular trafficking of GLUT4.

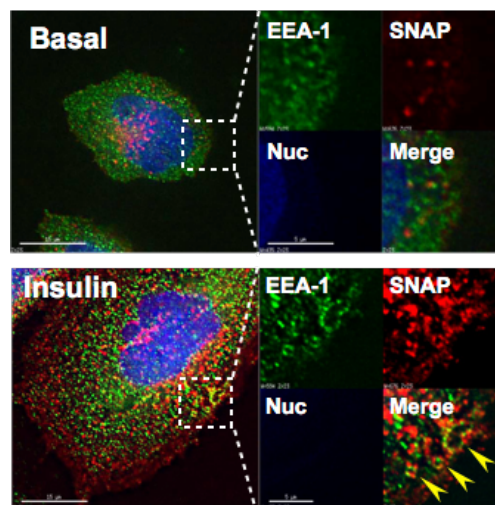


Figure 3.10. Immunofluorescence imaging of SNAP tag-labeled GLUT4 with early endosome marker (EEA-1). White boxes indicate enlarged images. Arrowheads, colocalization. Scale bars, 5 μ m.

Construction of high-content screening platform. Based on the results so far, I was confident with the utility of EGFP-GLUT4-SNAP system for the profiling of GLUT4 trafficking. Therefore, I constructed high-content screening platform using EGFP-GLUT-SNAP (Figure 3.11). I developed automated high-content image analysis protocol. In this platform, fluorescence images are taken after treatment of small molecules or siRNA in EGFP-GLUT4-SNAP expressing cells, then applied to analysis protocol. High-content analysis protocol divides the single cell fluorescence images into 4 cell compartments; whole cell, cell center, plasma membrane and perinuclear region. Next, GLUT4 proteins are detected from both EGFP and SNAP tag probe channels, and analyzed to obtain quantitative parameters including number, area and intensity of GLUT4-containing vesicles. Finally, all the phenotypic parameters are analyzed for the profiling of GLUT4 trafficking.

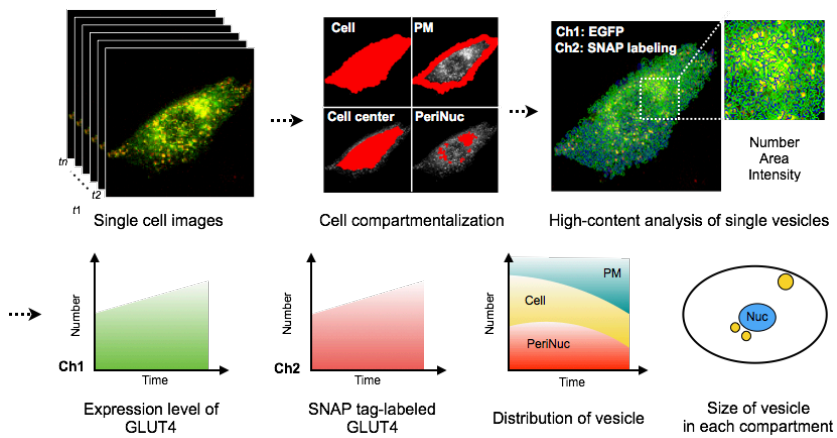


Figure 3.11. High-content screening (HCS) platform with EGFP-GLUT4-SNAP. Flow diagram of high-content analysis protocol. First of all, single cell fluorescence images are into 4 cell compartments; whole cell, cell center, plasma membrane and perinuclear region. Within each cell compartment, GLUT4 proteins are detected from both EGFP and SNAP tag-labeled channels. Single vesicles are analyzed to measure the number, area and intensity. Phenotypic parameters are analyzed depend on time and localization to exclude the information about spatiotemporal GLUT4 trafficking.

As a validation of our HCS platform, I investigated the kinetics of GLUT4 translocation and intracellular distribution of cycling GLUT4 under insulin stimulation. I applied the time-lapse cell images taken with insulin or not (Figure 3.12A) to the high-content analysis protocol. As shown in figure 3.12A, all the single vesicles in both EGFP and SNAP tag probe channels were detected, then I performed high-content analysis. First of all, data showed that number of SNAP-labeled GLUT4 rapidly increased upon insulin stimulation and reached saturation after 20 min while the signal increased 2-fold after 30 min (Figure 3.12B) and these results are consistent with previous data from fluorescence intensity quantification (Figure 3.7). Secondly, I analyzed the intracellular distribution of GLUT4 among perinuclear region, cytosol and PM. In basal state, the majority of SNAP tag-labeled GLUT4 are detected in perinuclear region, indicating GLUT4 recycles between PM and perinuclear region in basal state (Figure 3.12C). Upon insulin stimulation, a large proportion of the SNAP tag-labeled GLUT4 distributed to the vicinity of PM (Figure 3.12D). From these data, I confirmed the insulin-stimulated distribution of the cycling GLUT4 from perinuclear region to the vicinity of PM using our HCS platform. Taken together, I developed the novel HCS platform for the profiling of GLUT4 trafficking.

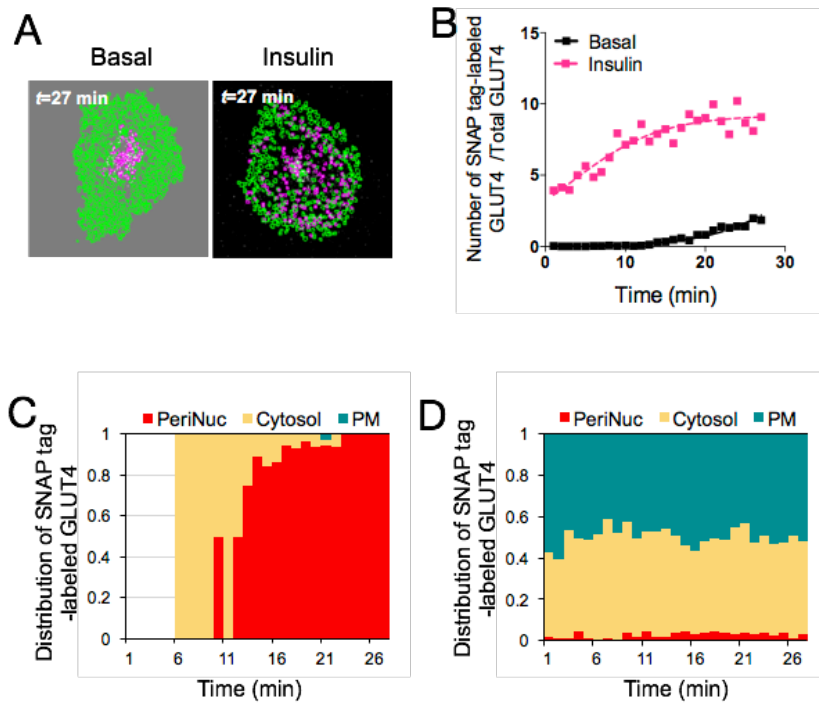


Figure 3.12. (A) Representative images of single vesicle detection in basal or insulin-stimulated cells. Green lines, EGFP. Pink lines, SNAP tag-labeling. (B) Time-dependent increase in number of SNAP tag-labeled GLUT4 versus total number of GLUT4. (C),(D) Intracellular distribution of SNAP tag-labeled GLUT4 between perinuclear region, cytosol and plasma membrane over time.

Rosiglitazone sensitizes insulin through distinct mode of GLUT4 trafficking. Rosiglitazone which is a sort of thiazolidinediones (TZDs) have been demonstrated to sensitize and augment insulin-stimulated increases of GLUT4 at the PM in differentiated adipocytes, but its effect on GLUT4 trafficking is not fully discovered [26-28]. Here, I investigated the effect of the rosiglitazone on GLUT4 trafficking with this HCS platform. Rosiglitazone is known to affect the differentiation process of adipocytes. Therefore, I differentiated 3T3-L1 first, then transfected cells with EGFP-GLUT4-SNAP. EGFP-GLUT4-SNAP expressing 3T3-L1 adipocytes were treated with rosiglitazone or not, and cells were stimulated with insulin. I incubated cells with membrane-impermeable SNAP tag probes (SNAPsurface 649) to quantitatively measure GLUT4 translocation to the PM, and observed GLUT4 trafficking by time-lapse fluorescence imaging. As shown in figure 3.13, insulin stimulation and co-treatment of insulin with rosiglitazone induced translocation of GLUT4 to the PM in 3T3-L1 adipocytes, thereby SNAP tag-labeling was increased. In addition, the line profiles of fluorescence intensities showed that SNAP tag-labeled GLUT4 are distributed in the vicinity of the PM.

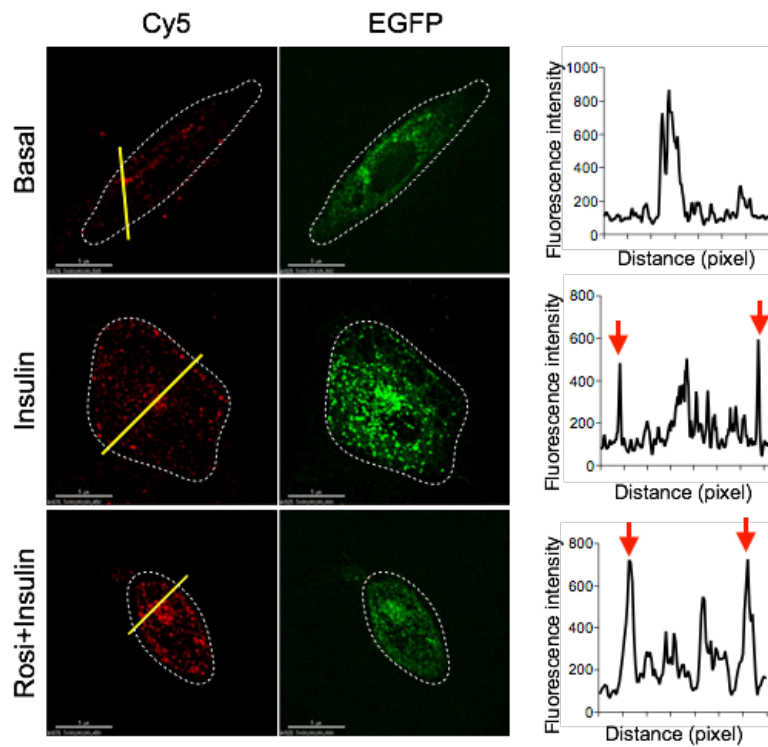


Figure 3.13. Effect of rosiglitazone co-treatment on intracellular GLUT4 distribution. After stimulation with insulin (170 nM), cells are labeled with SNAPsurface 649 (1 μ M) for 1 hour. Time-lapse fluorescence images were taken every minute with Cy5 and EGFP channels using DeltaVision imaging system. Line profiles of fluorescence intensities are obtained from indicated yellow lines on images. Red arrow, plasma membrane. Scale bars, 5 μ m.

Next, I analyzed GLUT4 trafficking with our HCS platform. First of all, I evaluated the number of GLUT4 that translocate to the PM by determining the ratio of SNAP tag-labeled number of GLUT4 vesicle ($Cy5_{tot}$) to total number of GLUT4 vesicles ($EGFP_{tot}$). Insulin increased the translocation of GLUT4 to the PM compared with basal condition, and co-treatment of rosiglitazone sensitized the effect of insulin by showing 2-fold increase in $Cy5_{tot}/EGFP_{tot}$ (Figure 3.14A). Consistent with line profiles of fluorescence intensities (Figure 3.13), the number of SNAP tag-labeled GLUT4 that are constantly located near the PM ($Cy5_{PM}$) was also increased by insulin stimulation, and co-treatment of rosiglitazone enhanced this effect (Figure 3.14B). These data suggest that rosiglitazone sensitizes the insulin-stimulated GLUT4 translocation to the PM and the localization of GLUT4 near the PM. Therefore, I hypothesized that rosiglitazone might sensitize the insulin by inducing the localization of GLUT4 near the PM. To test this idea, I analyzed the distribution of SNAP tag-labeled GLUT4 among perinuclear region, cytosol and vicinity of the PM (Figure 3.14D). As a result, data showed that co-treatment of rosiglitazone showed a distinct difference in intracellular distribution of SNAP tag-labeled GLUT4. Under insulin stimulation, the number of SNAP tag-labeled GLUT4 near the PM (Figure 3.14B, $Cy5_{PM}/EGFP_{tot}$) was increased, whereas the number of SNAP tag-labeled GLUT4 at the perinuclear region was maintained relatively constant. From these data, I convinced that insulin retaining the GLUT4 in endosomal compartment in the vicinity of

the PM according to recently suggested model about ISGT (Figure 3.8). On the other hands, co-treatment of rosiglitazone increased the number of SNAP tag-labeled GLUT4 present in perinuclear region (Figure 3.14C). Considering the basis that rosiglitazone increases endosomal recycling kinetic without specificity between GLUT4 and transferrin receptor (TfR) [28, 29], these data suggest that co-treatment of rosiglitazone increases the number of GLUT4 recycles *via* trans-golgi network by inducing the overall endocytosis kinetics in the cells, thereby increase the GLUT4 pool that can respond to insulin stimulation. Taken together, rosiglitazone sensitizes insulin-stimulate GLUT4 translocation through distinctly different mode of intracellular GLUT4 trafficking. Of course, there is a necessary of further study to elucidate the precise site of action of rosiglitazone with regard to the exocytosis and endocytosis steps, but I am confident with our HCS platform as a powerful tool for getting extensive amounts of information from a fluorescence imaging experiment.

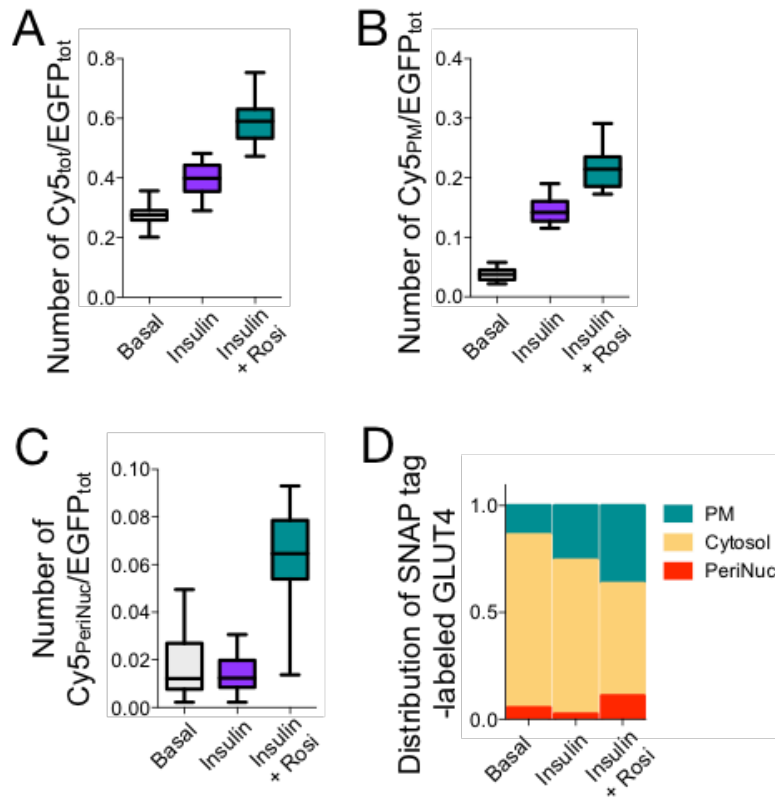


Figure 3.14. (A) Quantification of GLUT4 translocation to the PM by determining the number of SNAP tag-labeled GLUT4 versus total number of GLUT4. (B) Number of SNAP tag-labeled GLUT4 which are localized in near the PM versus total number of GLUT4. (C) Number of SNAP tag-labeled GLUT4 which are localized in perinuclear region versus total number of GLUT4. (D) Intracellular distribution of SNAP tag-labeled GLUT4 between perinuclear region (PeriNuc), cytosol, and plasma membrane (PM).

2.4. Conclusion

In summary, I developed a novel imaging system for monitoring dynamic GLUT4 trafficking in living cells. GLUT4 is importantly regulated to control body blood levels by insulin hormone. Dysregulation of GLUT4 trafficking is associated with insulin resistance and type 2 diabetes. Therefore, there have been many efforts to understand the mechanism of insulin signaling to control GLUT4 trafficking. However, these studies mostly depend on immuno-labeling and fixation. As a result, conventional methods are not only lack of robustness, but also strongly restrict spatiotemporal monitoring of dynamic GLUT4 trafficking in real-time. Recently, TIRF microscopy are extensively used to study GLUT4 trafficking that take place near PM including tethering and fusion. However, these studies are restricted to the investigation of GLUT4 trafficking events near the PM. Therefore, intracellular GLUT4 trafficking is still unclear and debating. In this context, I proposed the novel image-based high-content assay system ‘EGFP-GLUT4-SNAP’ for monitoring GLUT4 in living cells which enables spatiotemporal analysis of intracellular GLUT4 trafficking. I fused SNAP tag to the C-terminal of GLUT4, and designed to be exposed to extracellular

space only when GLUT4 translocate to the PM. Using fluorogenic- or non-fluorogenic- membrane-impermeable SNAP tag probes, I could monitor GLUT4 translocation in quantitative and real-time manners. As a result, I successfully confirmed insulin-stimulated real-time and quantitative translocation of GLUT4 to the PM in live cells. In addition, EGFP-GLUT4-SNAP system could be utilized for the real-time monitor intracellular GLUT4 trafficking. As a result, I could demonstrate the recently proposed dual mode-of-action of insulin on GLUT4 cycling (Figure 3.8) by proving that constant insulin stimulation induces the formation of endosomal pool near the PM. These findings about the transition of GLUT traffic from static retention to dynamic equilibrium by insulin will provide us a new insight to perturb insulin signaling pathways as an approach to combat insulin resistant and type 2 diabetes.

Finally, I constructed HCS platform to profile GLUT4 trafficking. This HCS platform will be used to study how chemical compounds or proteins perturb GLUT4 trafficking. As an example, I investigated the effect of rosiglitazone treatment on GLUT4 trafficking in 3T3-L1 adipocyte. Consistent with previous studies [28], co-treatment of rosiglitazone with insulin enhanced the GLUT4 translocation to the PM. Notably, I figured out that rosiglitazone has different mode of

intracellular GLUT4 trafficking compared with insulin; rosiglitazone enhances the GLUT4 recycling *via* trans-golgi network by inducing the overall endocytosis kinetics. These data indicate that different mode of intracellular GLUT4 trafficking between insulin and rosiglitazone may be a key mechanism to sensitize insulin by rosiglitazone treatment. Although the site of action of rosiglitazone for this difference remains unknown, I am confident that our HCS platform is a very powerful tool for discovering unrevealed information about GLUT4 trafficking in living cells. Taken together, EGFP-GLUT-SNAP-based HCS platform will be valuable research tool for studying type 2 diabetes and its treatment because of its utility of studying signaling pathways which regulate GLUT4 trafficking, and of studying mechanism-of-action of chemical compounds which increase cellular glucose uptake by regulating GLUT4 trafficking.

2.5. References

1. S. E. Kahn, R. L. Hull and K. M. Utzschneider, *Nature* 2006, **444**, 840–846.
2. D. Leto and A. R. Saltiel, *Nat. Rev. Mol. Cell Biol.* 2012, **13**, 383–396.
3. N. J. Bryant, R. Govers and D. E. James, *Nat. Rev. Mol. Cell Biol.* 2002, **3**, 267–277.
4. W. T. Garvey, L. Maianus, J. H. Zhu, G. Brechtel-Hook, P. Wallace and A.D. Baron, *J. Clin. Investig.* 1988, **101**, 2377–2386.
5. R. R. Henry, L. Abrams, S. Nikoulina and T. P. Ciaraldi, *Diabetes* 1995, **44**, 836–946.
6. L. J. Robinson, S. Pang, D. S. Harris, J. Heuser and D.E. James, *J. Cell. Biol.* 1992, **117**, 1181–1196.
7. H. Al-Hasani, D. R. Yver and S. W. Cushman, *FEBS Letters* 1999, **460**, 338–342.
8. P. Huang, Y. M. Altshuller, J. C. Hou, J. E. Pessin and M. A. Frohman, *Mol. Biol. Cell.* 2005, **16**, 2614–2623.
9. L. Jiang, J. Fan, L. Bai, Y. Wang, Y. Chen, L. Yang, L. Chen and T. Xu, *J. Biol. Chem.* 2008, **283**, 8508–8516.
10. C. H. Li, L. Bai, D. D. Li, S. Xia and T. Xu, *Cell Research* 2004, **14**, 480–486.
11. Y. Xu, B. R. Rubin, C. M. Orme, A. Karpikov, C. Yu, J. S. Bogan and D. K. Toomre, *J. Cell Biol.* 2011, **193**, 643–653.
12. K.G. Stenkula, V. A. Lizunov, S. W. Cushman and J. Zimmerberg, *Cell Metabolism* 2010, **12**, 250–259.
13. A. Ladler and C. Shultz, *Angew. Chem. Int. Ed.* 2013, **52**, 2408–2410.
14. K. Dean and A. Palmer, *Nat. Chem. Biol.* 2014, **10**, 512–523.

15. A. Juillerat, T. Gronemeyer, A. Keppler, S. Gendreizig, H. Pick, H. Vogel and K. Johnsson, *Chemistry & Biology* 2003, **10**, 313–317.
16. G. Lukinavičius et al., *Nat. Chem.* 2013, **5**, 132–139.
17. C. J. Zhang, L. Li, G. Y. Chen, Q. H. Xu and S. Q. Yao, *Org. Lett.* 2011, **13**, 4160–4163.
18. X. Sun et al., *ChemBioChem* 2011, **12**, 2217–2226.
19. E. Prifty, L. Reymond, M. Umebayashi, R. Hovius, H. Riezman and K. Johnsson, *ACS. Chem. Biol.* 2014, **9**, 606–612.
20. J. Holleran, D. Brown, M. H. Fuhrman, S. A. Adler, G. W. Fisher and J. W. Jarvik, *Cytometry A.* 2010, **7**, 776–782.
21. V. Patki, J. Buxton, A. Chawla, L. Lifshitz, K. Fogarty, W. Carrington, R. Tuft and S. Corvera, *Mol. Biol. Cell.* 2011, **12**, 129–141.
22. P. D. Brewer, E. N. Habtemichael, I. Romenskaia, C. C. Mastick and A. C. F. Coster, *J. Biol. Chem.* 2014, **289**, 17280–17298.
23. J. M. Muretta, I. Romenskaia and C. C. Mastick, *J. Biol. Chem.* 2008, **283**, 311–323.
24. O. Martin, A. Lee and T. E. McGraw, *J. Biol. Chem.* 2006, **281**, 484–490.
25. H. Zaid, C. N. Antonescu, V. K. Randhawa and A. Klip, *Biochem. J.* 2008, **413**, 201–215.
26. M. Shintani, H. Nishimura, S. Yonemitsu, Y. Ogawa, T. Hayashi, K. Hosoda, G. Inoue and K. Nakao, *Diabetes* 2001, **50**, 2296–2230.
27. S. Yonemitsu, H. Nishimura, M. Shintani, R. Inoue, Y. Yamamoto, H. Masuzaki, Y. Ogawa, K. Hosoda, G. Inoue, T. Hayashi and K. Nakao, *Diabetes* 2001, **50**, 1093–1101.
28. L. Martinez, M. Berenguer, M. C. Bruce, Y. L. Marchand-Brustel and R. Govers, *Biochemical Pharmacology* 2010, **79**, 1300–1309.
29. C. Livingstone, D. E. James, J. E. Rice, D. Hanpeter and G. W. Gould, *Biochem. J.* 1996, **315**, 487–495.

Chapter 4. Discovery of anti-obesity small molecule via monitoring cellular lipid droplets

4.1. Introduction

Obesity is disease that threatens human life quality. Obesity is highly associated with the risk of metabolic diseases such as type 2 diabetes, dyslipidemia, hypertension, and cardiovascular disease and cancer [1, 2]. Obesity can be cause by variety of genetic [3] or environmental factors [4], and the constant growing obesity population is causing serious social costs in the world.

Obesity is defined as a medical condition of an energy intake over energy expenditure and excessive energy stored in the body [5]. Adipose tissue is an energy storage organ that regulates energy balance of our body. Adipose tissue stores energy in the form of triglycerides, and release non-esterified fatty acids (NEFAs) and glycerol into circulation when energy is limiting [6]. Under obesity, excess amounts of fats are stored in adipose tissue resulting hypertrophy and hyperplasia of adipocytes. A variety of mechanisms explain the correlation between obesity with the pathogenesis

of metabolic disorders. In obesity, more NEFAs are released from adipose tissue, leading to insulin resistance and lipotoxicity in β -cell, liver and muscle [7, 8]. In addition, adipose tissue plays a role in the production and secretion of adipose hormones (adipokines) that regulate energy homeostasis [9]. In obese subjects, several adipokines are increased leading insulin resistance in our body [10, 11]. Overall, obesity results in imbalance of energy homeostasis, leading systematic metabolic disorder. Therefore, there is an urgent need for the pharmaceutical agent to manage obesity and obesity-associated metabolic diseases.

Here in, I discovered a novel small molecule that decreasing obesity, SB1501, by image-based high-content screening (HCS). In addition, I demonstrate the therapeutic potential of SB1501 in decrease obesity and improve metabolic parameter *in vivo*.

4.2. Materials and methods

Cell culture

HeLa cells and 3T3-L1 cells (mouse embryonic fibroblasts) were obtained from ATCC [American Type Culture Collection]. HeLa cells were maintained in RPMI containing 10% fetal bovine serum (FBS) [GIBCO] and 1% antibiotic-antimycotic solution at 37 °C in an atmosphere of 5% CO₂. 3T3-L1 cells were maintained in DMEM containing 10% heat-inactivated bovine calf serum (BCS) [GIBCO] and 1% antibiotic-antimycotic solution at 37 °C in an atmosphere of 5% CO₂.

Animals and administration

C57BLKS/*J-db/db* mice were obtained from Central Lab Animal Inc. (Seoul, South Korea). Rosiglitazone (oral gavage, 15 mg/kg/day) and SB1501 (oral gavage, 10 mg/kg/day and 20 mg/kg/day) were administered for 4 weeks. For the glucose tolerance tests (GTTs), mice were fasted for 12 hrs, and glucose was injected. Blood glucose concentrations were measured at 15, 30, 60, 90, and 120 min after glucose injection. All experiments were approved by the Institute of Laboratory Animal Resources of Seoul National University.

3T3-L1 differentiation

After reaching confluence, 3T3-L1 cells were differentiated by treating the cells with 1 μM dexamethasone, 10 μM rosiglitazone, and 5 $\mu\text{g}/\text{ml}$ insulin in DMEM containing 10% FBS for 2 days, and the cell culture was subsequently maintained by substituting the medium with fresh DMEM containing 10% FBS and 5 $\mu\text{g}/\text{ml}$ insulin.

Image-based high-throughput screening for monitoring cellular LDs.

HeLa cells were cultured on black 96-well plates. Small molecules (final concentration of 10 μM) were added to the designated wells using a pin tool and incubated for 24 hrs. SF44 (5 μM) and Hoechst 33342 (2 $\mu\text{g}/\text{mL}$) were added to individual wells. After 30 min incubation at 37 °C, fluorescence images of the each well were acquired automatically using InCell Analyzer 2000 [GE Healthcare]. Fluorescence images were captured using an excitation filter at CFP channel and an emission filter at Cy3 channel. Fluorescence images of Hoechst 33342 were captured using an excitation filter at 350 ± 25 nm, exposure of 0.3 s, and an emission filter in the blue channel. Fluorescence intensities were analyzed using the InCell Analyzer 1000 workstation 3.6 program.

Western blot analysis

3T3-L1 cells were seeded on 6 well plate, and differentiated at 100% confluency. From the first day of differentiation, SB1501 was treated to

cells for 8 days while maintaining the cells with fresh DMEM containing 10% FBS and 5 $\mu\text{g}/\text{ml}$ insulin. After 8 days, cell lysates were obtained by RIPA buffer containing 1x protease inhibitor cocktail [Roche]. The proteome was analyzed by SDS-PAGE and transferred into PVDF membrane. After blocking with 2% BSA-TBST for 1 hr, membranes were treated with desired primary antibody (1:1000 in 1% BSA-TBST) overnight at 4 °C. After washing with TBST for 3 times, membranes were exposed to HRP-conjugated secondary antibody (1:2000 in 1% BSA-TBST) for 1 hr at room temperature, and developed by ECL prime [GE Healthcare]. Chemiluminescent signal was scanned by ChemiDoc™ MP imaging system [Biorad].

Gene expression analysis (qRT-PCR)

3T3-L1 cells were seeded on 6 well plate, and differentiated at 100% confluency. From the first day of differentiation, 40 μM of SB1501 was treated to cells for 8 days while maintaining the cells with fresh DMEM containing 10% FBS and 5 $\mu\text{g}/\text{ml}$ insulin. After 8 days, total RNA was isolated using RNA isolation kit [Qiagen]. cDNA was synthesized using reverse transcriptase kit and oligo(dT) primer according to manufacturer's instruction [Bioneer]. Quantitative real-time PCR was performed with cDNA, primers and SYBR Green [Kapa Biosystems]. The Applied Biosystems™ StepOnePlus real-time PCR system was used for qRT-PCR. All the primers for qRT-PCR were obtained from Bioneer.

Immunofluorescence imaging

3T3-L1 cells were seeded on 6 well plate, and differentiated at 100% confluency. From the first day of differentiation, 40 μ M of SB1501 was treated to cells for 8 days while maintaining the cells with fresh DMEM containing 10% FBS and 5 μ g/ml insulin. After wash out medium with PBS, cells were fixed with 3.7 % paraformaldehyde for 15 min at room temperature and permeabilized with 0.1% TritonX-100 in PBS for 10 min. After the blocking of cells with 4% BSA in PBS for 1 hr at room temperature, primary antibody (UCP1 and PGC-1 α , 1:200 in 1% BSA-PBS) was incubated overnight at 4 $^{\circ}$ C. After washing with PBS for three times, cells were incubated with TRITC-conjugated secondary antibody (1:200 in 1% BSA-PBS) for 2 hrs at room temperature. After washing with PBS for 5 times, nucleus was stained with Hoechst 33342 [Thermo Scientific] and washed out. Fluorescence microscopy imaging was performed using DeltaVision imaging system [GE Healthcare] equipped with 60x objective lenses of Olympus IX-71 inverted microscope. Temperature was maintained at 23 $^{\circ}$ C.

Measurement of triglyceride (TG) concentration

3T3-L1 cells were seeded on 12 well plate and differentiated at 100% confluency. After induce differentiation, cells were maintained for 8 days with DMEM containing 10% FBS, 5 μ g/ml insulin and SB1501. After 8 days, cells were incubated with 5% NP-40 in ddH₂O. The total proteomes

were transferred to ep-tube, and measure triglyceride concentration using Triglyceride Quantification Assay Kit [Abcam] according to manufacturer's instruction.

Target identification with TS-FITGE technology

HeLa cells were harvested with trypsin/EDTA solution and resuspended in a conical tube before compound treatment. 20 μ M of SB1501 was incubated with HeLa cells for 1 hr. After compound treatment, cells were heated to a range for 3 min (From 37 $^{\circ}$ C to 56.1 $^{\circ}$ C). Total proteome was obtained by lysis cells with freeze-thawed cycle with liquid nitrogen. Soluble fraction was obtained from the supernatants after centrifugation at 20,000g for 20 min at 4 $^{\circ}$ C. After methanol precipitation, the pellet was resuspended with 10 μ l of conjugation buffer (30 mM Tris-HCl (pH 8.6), 2M thiourea, 7M urea, 4% CHAPS (w/v)) by sonication. 1 μ l of 0.4 mM Cy3-NHS or Cy5-NHS were added and incubated at 4 $^{\circ}$ C for 45 min. After the conjugation, methanol was added to the mixture for precipitation and incubated at -20 $^{\circ}$ C for 1h. The mixture was centrifuged at 20,000 g for 3 min at 4 $^{\circ}$ C. Supernatants were discarded, and the pellet was washed with MeOH. The pellets were resuspended with 75 μ l of rehydration buffer (7 urea, 2M thiourea, 2% CHAPS (w/v), 40 mM DTT, and 1% IPG buffer) by sonication. The sample from both compound-treated group (Cy5 conjugated) and DMSO-treated group (Cy3 conjugated) were mixed. 150

μ l of the mixtures were separated by 2D-gel electrophoresis using Ettan IPGphor [GE Healthcare] and Ettan DALTsix electrophoresis system [GE Healthcare]. The resulting gels were scanned with Typhoon Trio [GE Healthcare].

Statistical analysis

The results are shown as means \pm SEM. The student's t-test was used for comparison between experimental groups (Microsoft). P values of <0.05 were considered significant.

4.3. Results and discussion

Discovery SB1501 from the image-based HTS. Obesity is a condition of excess fat storage in adipocyte. One of the most dramatic phenotypic change of obese adipocytes is enlarged unilocular lipid droplets by the storage of excess energy intake [15]. In this point of view, I hypothesized that the quantity and size of lipid droplets are a key phenotype for measure adiposity of cells. In previous study in our laboratory, we constructed a novel high-content screening platform of monitoring cellular lipid droplets to discover autophagy modulator with the basis that size and quantity of lipid droplets are a late-stage marker of autophagy process (Figure 4.1) [16].

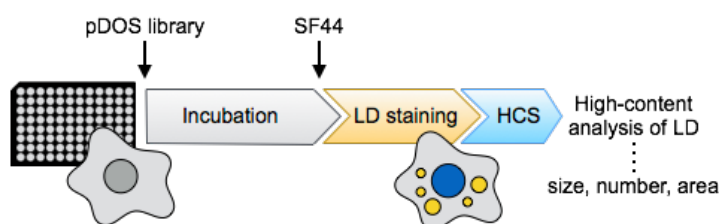


Figure 4.1. Schematic diagram of image-based phenotypic screening to discover bioactive small molecule via monitoring cellular lipid droplets

Nonetheless, cellular lipid droplets are also significantly influenced by lipid biogenesis and metabolism [17, 18]. As a result, screening of in-house small molecule library identified several hit compounds without alteration of cellular autophagic process. Among them, SB1501 (Figure 4.2a) most efficiently reduced lipid droplet in a dose-dependent manner without cell toxicity and autophagic induction (Figure 4.2b and 4.2c). Moreover, lipid accumulation which are driven by ectopic infusion of fatty acid was also restricted by SB1501. On the basis of these results, I concluded that SB1501 is a novel small molecule that can reduce cellular lipid

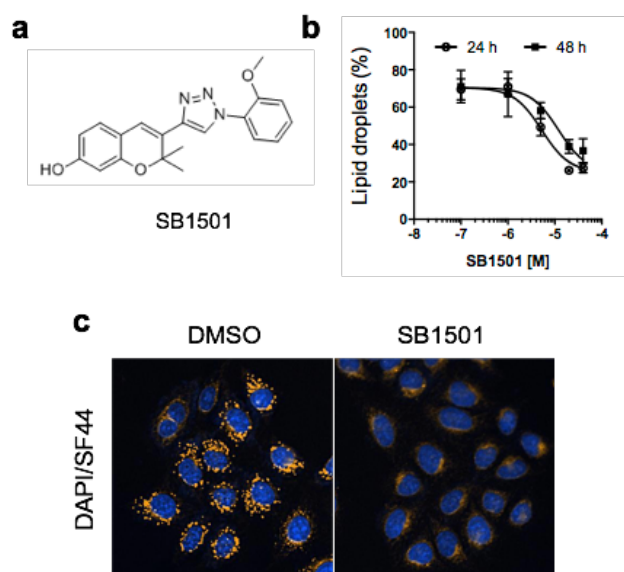


Figure 4.2. Discovery novel bioactive compound SB1501 through lipid droplet monitoring HCS. (a) Structure of hit compound, SB1501. (b) Dose-dependent LD decrease in HeLa cell line after treatment of SB1501. (c) Fluorescence images after 24 h treatment of DMSO or SB1501 (40 μM) in HeLa cell line.

accumulation by inhibiting lipid biogenesis or accelerating lipid metabolism process.

SB1501 decreases lipid droplets in 3T3-L1 adipocytes. In this point of view, I hypothesized that SB1501 might be a novel bioactive small molecule for treating adiposity of adipocytes by reducing lipid storage of cells. To confirm this idea, I treated SB1501 into differentiated 3T3-L1 adipocytes, and observed quantify and size of lipid droplets *via* image-based high-content analysis. 3T3-L1 pre-adipocytes are the most common *in vitro* model for studying adipocytes. Once differentiation of pre-adipocytes is induced, the cells start to express transcriptional regulators of adipogenesis and differentiated into adipocytes with accumulation of excess amounts of fats forming large lipid droplets [19]. After the induction of differentiation of 3T3-L1 pre-adipocytes, I treated SB1501 into cells during the course of differentiation with different time term (Figure 4.3a). After 8 days, I observed phenotypic change of lipid droplets by staining cells with SF44—a novel fluorescent lipid droplet bioprobe. As shown in figure 4.3b, long-term treatment of SB1501 induced the formation of multilocular lipid droplets with reduced size compared with vehicle (DMSO)-treated cells.

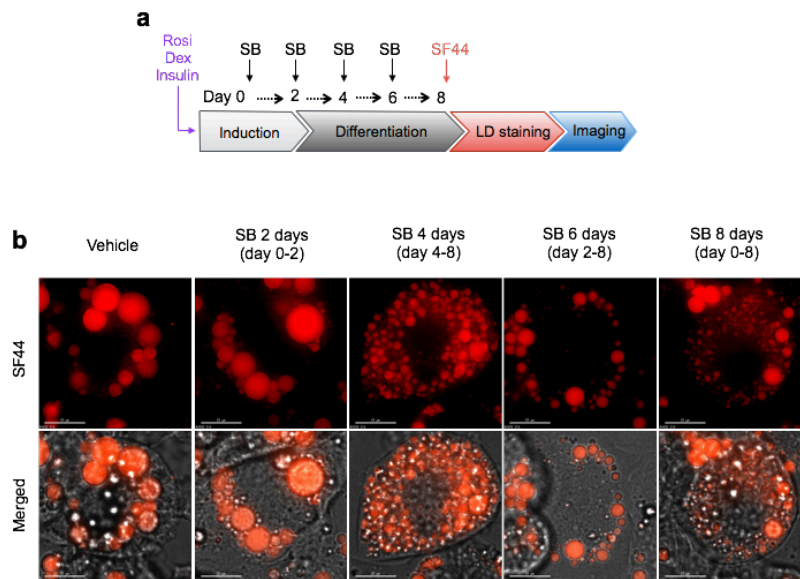


Figure 4.3. (a) Experiment design to investigate the bioactivity of SB1501 in differentiated 3T3-L1 adipocytes. (b) After treatment of SB1501 (40 μM) during the 3T3-L1 differentiation, cells are stained with SF44 (5 μM) to visualize lipid droplets. Fluorescence images are taken by DeltaVision imaging system. Scale bars are 15 μm .

Consistent with microscopy images, quantitative high-content analysis of images revealed that SB1501 effectively reduced the distribution of the size of each single lipid droplets (Figure 4.4a). In addition to the decrease in the size of LDs, SB1501 also effectively reduced fat storage within cells as determined by measurement of SF44 fluorescence intensity (Figure 4.4b) and triglyceride (TG) concentration (Figure 4.4c). On the other hands, SB1501 treatment at early stage of differentiation, from day 0 to day 2, did not reduce size of lipid droplets and fat storage in adipocytes. SB1501 also did not suppressed the expression of key regulatory genes (PPAR α and aP2) for adipogenesis process [19]. From these data, I convinced that SB1501 does not have critical effect on transcriptional regulation of adipocyte differentiation, while distinctly reduce fat storage of adipocytes.

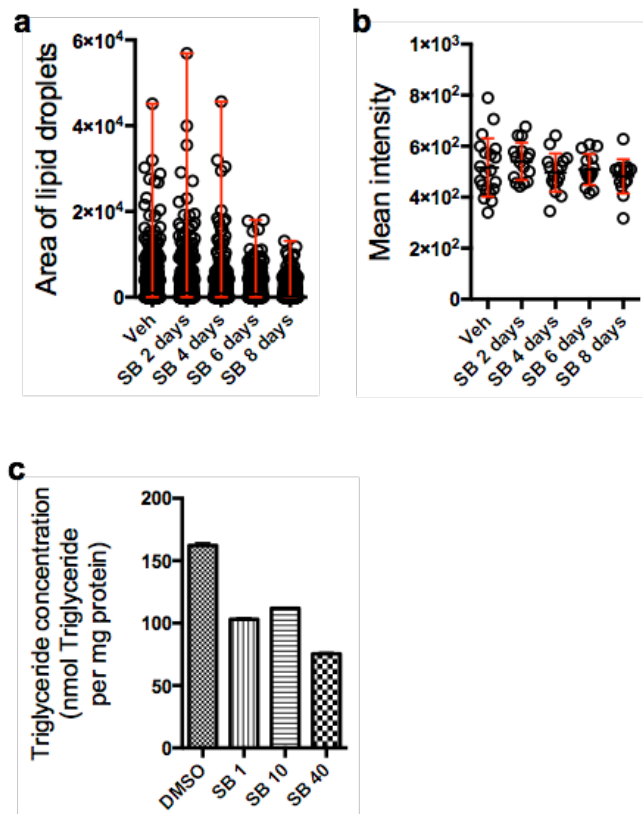


Figure 4.4. (a) Distribution of the size of each single lipid droplets after the treatment with SB1501 for 8 days. (b) Mean fluorescence intensities of cells stained with SF44 after treatment of SB1051 for 8 days. (c) Quantification of triglyceride (TG) concentration after cell lysis and extraction of TG from 3T3-L1 adipocytes.

SB1501 increases mitochondrial biogenesis and fatty acid oxidation via PGC-1 α . To elucidate the mechanism of action of SB1501-dependent decrease of fat storage, I observed the change in mitochondria biogenesis and fatty acid oxidative metabolism after SB1501 treatment. At present, a number of studies revealed that increased mitochondria biogenesis and oxidative metabolism can ameliorate the development of type 2 diabetes [20, 21, 22]. Especially, fatty acid oxidation can ameliorate the lipid accumulation, which is believed to contribute to the restoration of insulin sensitivity. In this regard, I investigated the expression of proteins which are involved in the process of mitochondria biogenesis and fatty acid oxidation.

PGC-1 α , a transcriptional co-activator, is a master regulator of energy metabolism. PGC-1 α induces pathways for energy metabolism such as adaptive thermogenesis, mitochondria biogenesis, and fatty acid oxidation [23, 24, 25]. Therefore, I investigated the SB1501-dependent regulation of PGC-1 α expression, and up-regulation of its downstream cellular processes involved in mitochondria biogenesis and fatty acid oxidation. After treatment of SB1501 for 8 days in differentiated 3T3-L1 adipocytes, I observed the effect of SB1501 on the induction of PGC-1 α expression (Figure 4.5a). I also confirmed that SB1501 increases the mitochondria biogenesis as shown by the increased mitochondrial proteins (Cox iv, CPT1, Figure 4.5a), mitochondrial DNA (mtDNA) copy number (Figure 4.5b) and mitotracker staining (Figure 4.5c). Uncoupling protein 1 (UCP1)

is a downstream protein of PGC-1 α , which is the gold standard protein marker of adaptive thermogenesis in adipocyte [26, 27]. Stimulation of certain signaling pathways can induce UCP1-expressing adipocytes in WAT, so-called brown-like or beige adipocytes, and these adipocytes promote the dissipation of energy as a heat [28]. Considering the role of BAT in energy expenditure by oxidizing fatty acid to generate heat through the action of UCP1, I strongly anticipated the effect of SB1501 on the induction of UCP1 expression resulting the reduced fatty acid accumulation and the formation of multilocular lipid droplets. As I hypothesized, immunoblot analysis and immunofluorescent imaging revealed that SB1501 increased the expression of UCP1 (Figure 4.5a and 4.5c). Meanwhile, temporal immunoblot analysis of PGC-1 α and UCP1 revealed that SB1501 induces expression of PGC-1 α earlier than that of UCP1. Overall, these data demonstrated that SB1501 decreases fat storage by inducing mitochondria biogenesis and fatty oxidation *via* regulation of PGC-1 α in adipocytes. Furthermore, decrease in the expression level of Fat-specific protein 27 (Fsp27) which mediate the fusion of lipid droplets in adipocytes, means that SB1501 reduces the demand for lipid storage capacity due to decreased adiposity (Figure 4.5a).

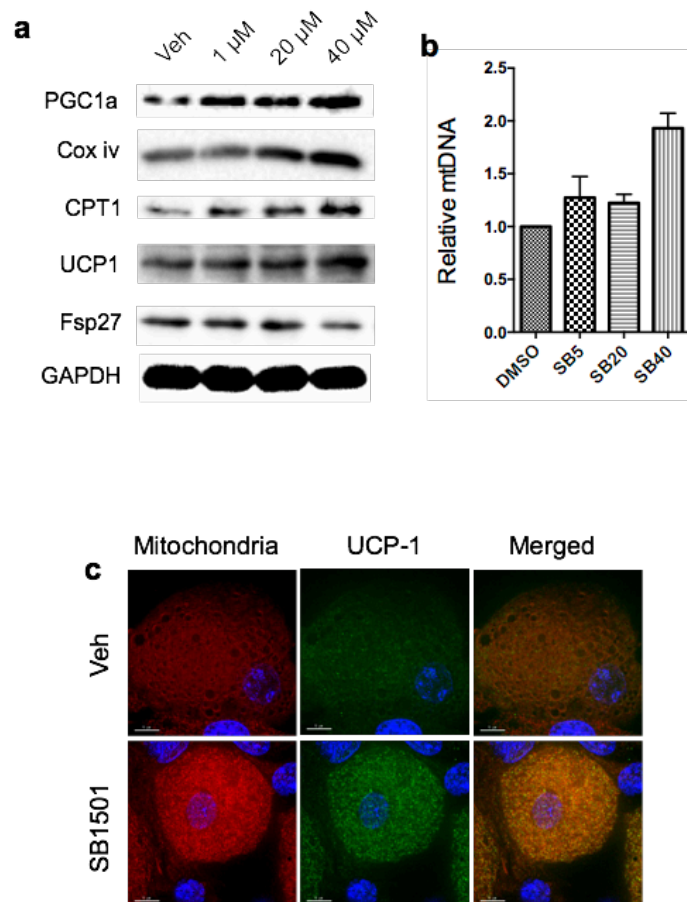


Figure 4.5. Effects of SB1501 treatment in 3T3-L1 adipocytes. (a) Immunoblot analysis of proteins involved in mitochondria biogenesis, fatty acid oxidation and adaptive thermogenesis after dose dependent treatment of SB1501 (40 μ M) for 8 days. (b) Mitochondria DNA (mtDNA) quantification using real-time QPCR analysis. (c) Immunofluorescence imaging of UCP-1 after treatment with Veh or SB1501. Scale bars indicate 15 μ m.

Consistent with changes in protein level, SB1501 increased expression level of genes for mitochondria biogenesis (PGC-1 α , PPAR α , TFAM), fatty acid uptake and metabolism (CPT1, CD36, LPL) and unilocular LD formation (Fsp27) (Figure 4.6).

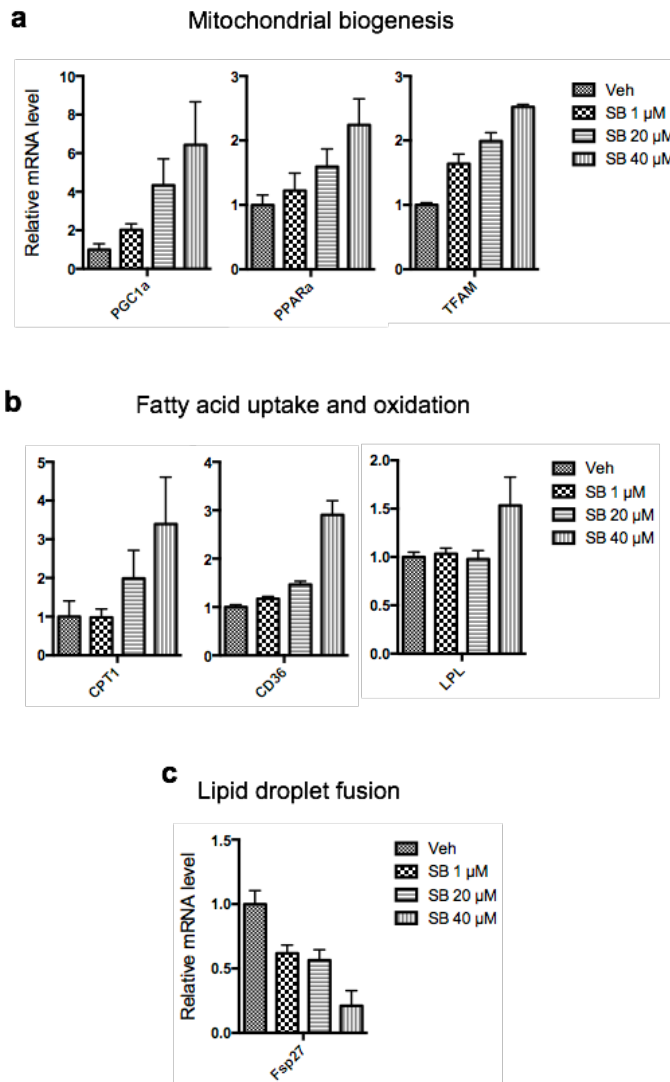


Figure 4.6. Quantitative real-time PCR analysis after dose dependent treatment of SB1501 for 8 days.

SB1501 changes mRNA level of adipokines. SB1501 suppressed the mRNA level of resistin, an adipokine which is considered to promote obesity-mediated insulin resistance and T2DM, whereas mRNA level of adiponectin, known to enhance insulin sensitivity, was slightly increased (Figure 4.7) [11]. From these data, I convinced that SB1501 changes transcriptional regulation of adipocytes to improve the metabolic activity.

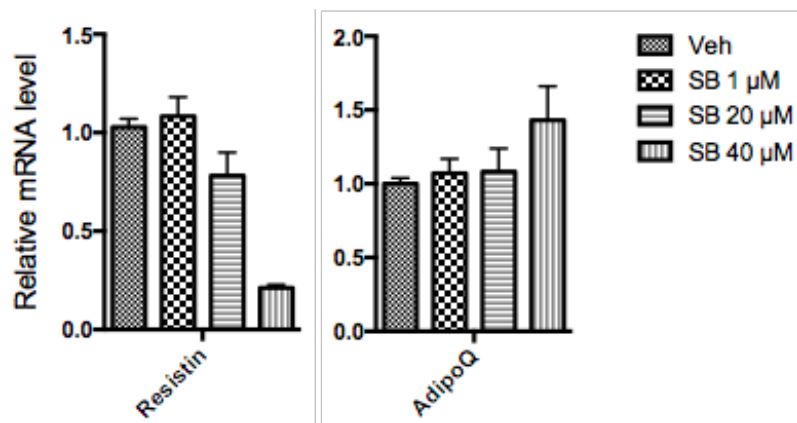


Figure 4.7. Quantitative real-time PCR analysis of adipokine mRNA level after dose dependent treatment of SB1501 for 8 days.

SB1501 prevents obesity and improves glucose homeostasis in obese *db/db* mice. Taken together, I convinced that SB1501 reduces the fat storage of adipocytes by inducing PGC-1 α dependent cellular processes involved in mitochondria biogenesis and fatty acid oxidation. In particular, increase of UCP1 expression imply that SB1501 might have a potential to promote 'Browning' process in WAT which is considered as a novel approach to treat obesity and obesity-mediated metabolic disorders [28]. Moreover, SB1501 showed potential to improve insulin resistance of human body by reducing the transcriptional level of resistin and increasing adiponectin. Taken together, I convinced that SB1501 might has a therapeutic potential to reduce obesity and to improve metabolic parameters *in vivo* via its effects on energy expenditure in adipocytes. Therefore, I tested therapeutic potential of SB1501 for obesity and obesity-induced metabolic disorder *in vivo* using *db/db* mice model.

Obese *db/db* mice is a useful *in vivo* model for studying obesity-induced metabolic defects. Therefore, I orally injected SB1501 daily for 4 weeks in *db/db* mice, then observed metabolic parameters. As a positive control, rosiglitazone was tested in parallel [29, 30]. Consistent with the phenotypic changes shown *in vitro* studies, SB1501-treated *db/db* mice showed significant reduction in its body weight (Figure 4.8a). SB1501-treated mice started to show weight loss from the second week compared to vehicle group, resulting decrease in the weight of mice by 5.2 g, whereas the weight of vehicle- or rosiglitazone-treated mice was increased by 2.5 g and

11.6 g respectively (Figure 4.8b). These results were also consistent with the reduction of the tissue weight of adipose tissues (IWAT, BAT) (Figure 4.8c and d) and the reduction of daily food intake (Figure 4.8e). From these data, I convinced that SB1501 has a therapeutic potential for combating obesity by reducing fat storage in adipose tissue and body mass.

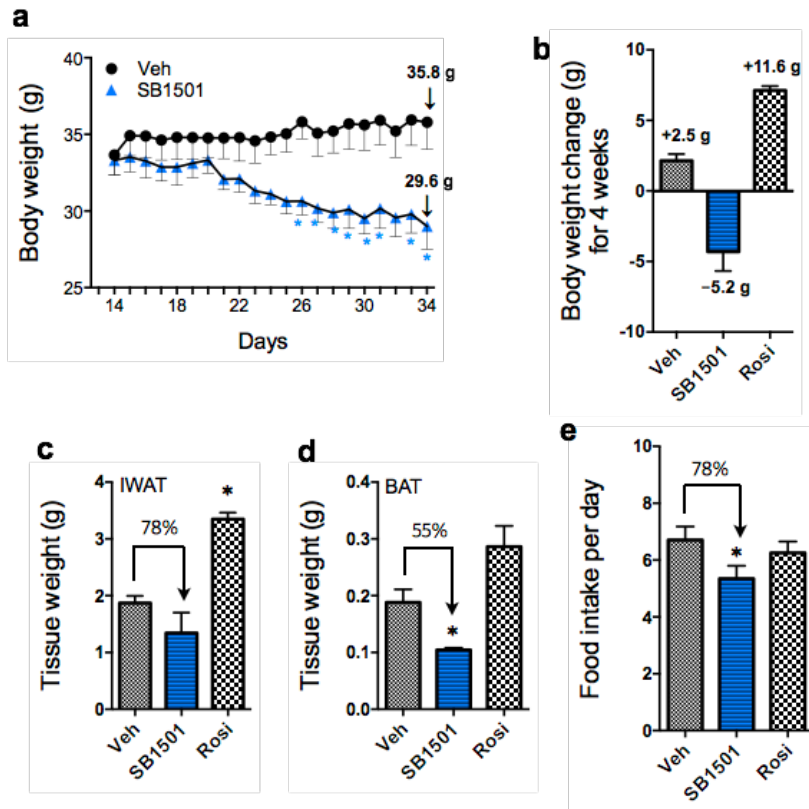


Figure 4.8. SB1501 improves metabolic profiles in *db/db* mice. (a),(b) Body weight changes of *db/db* mice for 4 weeks. SB1501 (10 mpk)-injected mice showed drastic weight decrease compared with vehicle- and rosiglitazone (15 mpk)-injected mice. (c) Weight of IWAT after 4 weeks of administration of vehicle, SB1501 and rosiglitazone. (d) Weight of BAT after 4 weeks of administration of vehicle, SB1501 and rosiglitazone. (e) Daily food intake data.

Glucose tolerance tests (GTTs). Obesity is ultimately related with the development of metabolic complications including insulin resistance [1, 2]. To confirm whether SB1501 improves glucose homeostasis regulation with decreasing obesity, I studied glucose tolerance tests (GTTs) in db/db mice. As shown in figure 4.9, SB1501 shown to ameliorate glucose tolerance to a similar level of rosiglitazone. Combined with body weight change and histology of adipose tissues, I confirmed that SB1501 has therapeutic potential to decrease the obesity and to improve glucose homeostasis.

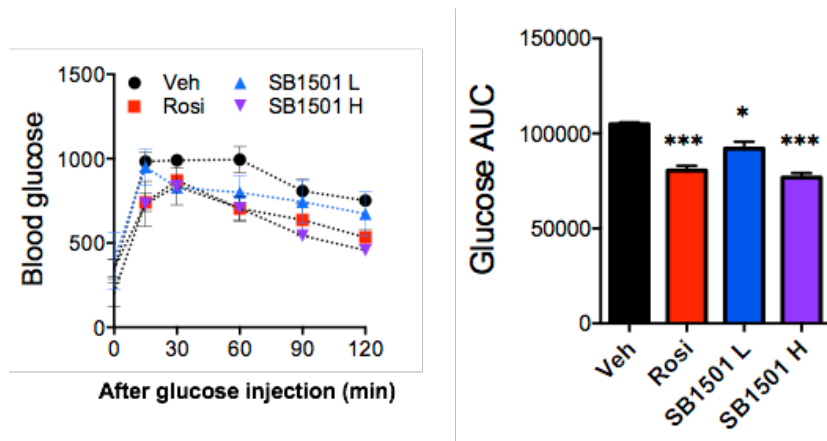


Figure 4.9. Glucose tolerance tests (GTTs) after the administration of SB1501 for 4 weeks. SB1501 L (10 mpk), SB1501 H (20 mpk) and rosiglitazone (15 mpk). Area under curves of GTTs data is also presented.

SB1501 induces browning process in IWAT and BAT. Consistent with the body weight data, H&E staining of IWAT and BAT sections of *db/db* mice showed that SB1501 treatment significantly reduced the size of adipocytes in both IWAT and BAT (Figure 4.10). Considering that the size of adipocyte is inversely correlate with insulin sensitivity, I convinced that SB1501 reduced body weight and fat mass by decreasing fat accumulation in adipocytes, and resulting improvement in glucose tolerance in *db/db* mice.

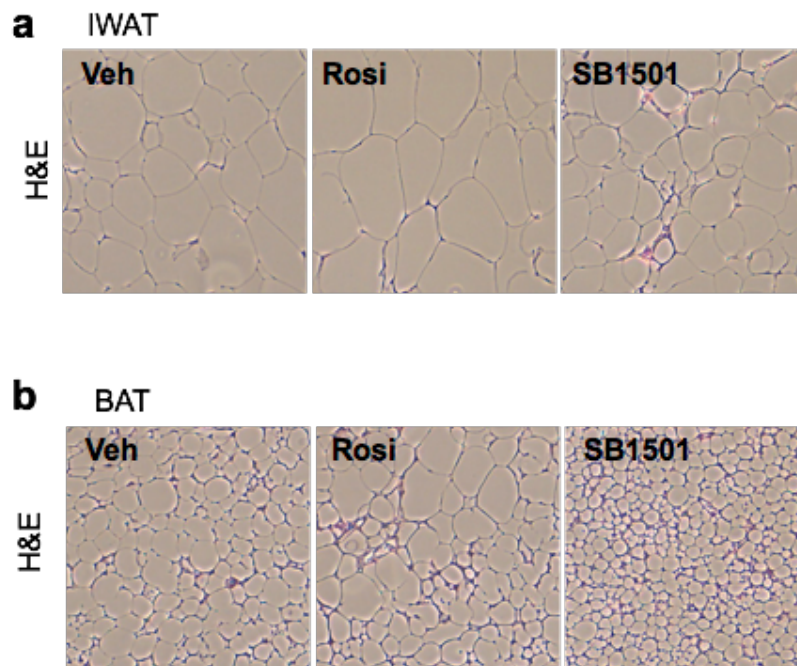


Figure 4.10. H&E staining of (a) IWAT and (b) BAT after the administration of SB1501 for 4 weeks.

Moreover, evident increase in the expression of PGC-1 α and UCP1 in both IWAT and BAT, as shown by immunofluorescent imaging, implied that SB1501 combats obesity by increasing energy expenditure of adipose tissues through the PGC-1 α —UCP1 regulatory axis (Figure 4.11). Notably, formation of adipocytes that composed of multilocular lipid droplets in WAT, is a representative BAT-like phenotype [28, 31], suggesting that SB1501 might induce the browning of IWAT and the thermogenic regulation *in vivo*.

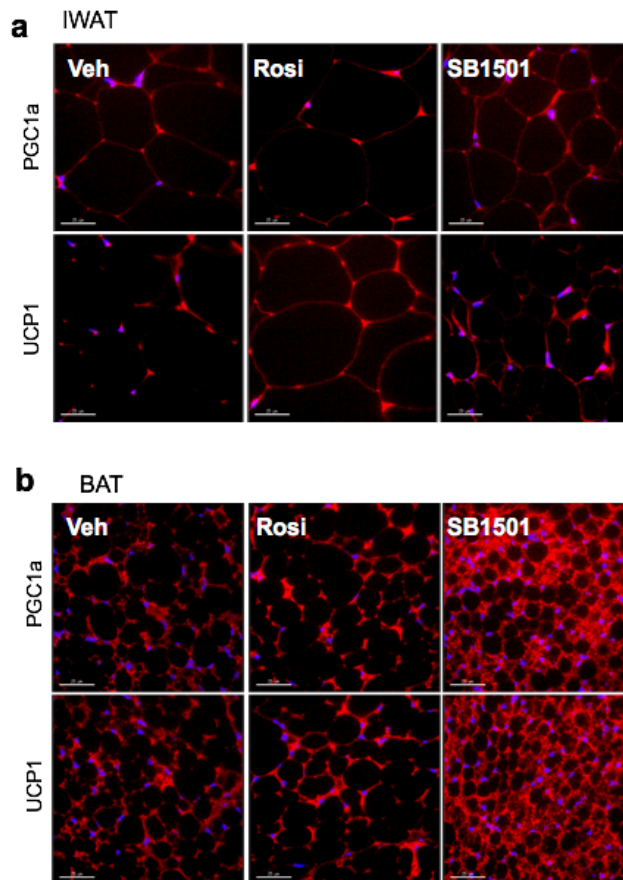


Figure 4.11. Immunofluorescent imaging of PGC-1 α and UCP1 in (a) IWAT and (b) BAT. Scale bars indicate 15 μ m.

Therefore, I investigated the alterations in gene expression of IWAT and BAT by quantitative real-time PCR analysis (Figure 4.12). Consistent with immunofluorescent imaging data, SB1501 dramatically increased the expression of UCP1 and PGC-1 α in IWAT. Along with the upregulation in brown adipocyte marker (Cidea), we also observed the increase in genes for regulating mitochondria biogenesis (Cox iv) and fatty acid oxidation (Acox1 and CPT1b) in IWAT (Figure 4.12a). In the BAT, there were significant increase in the thermogenic gene expression level (UCP1), but PGC-1 α mRNA level was not significantly changed. Nonetheless, I could observe evident increase in the expression of genes regulating mitochondria biogenesis and fatty acid oxidation (Figure 4.12b). Together, these data suggested that SB1501 reduces the body weight and fat mass by increasing energy expenditure of adipose tissues thermogenic program, thereby ameliorating insulin resistance *in vivo* mice model.

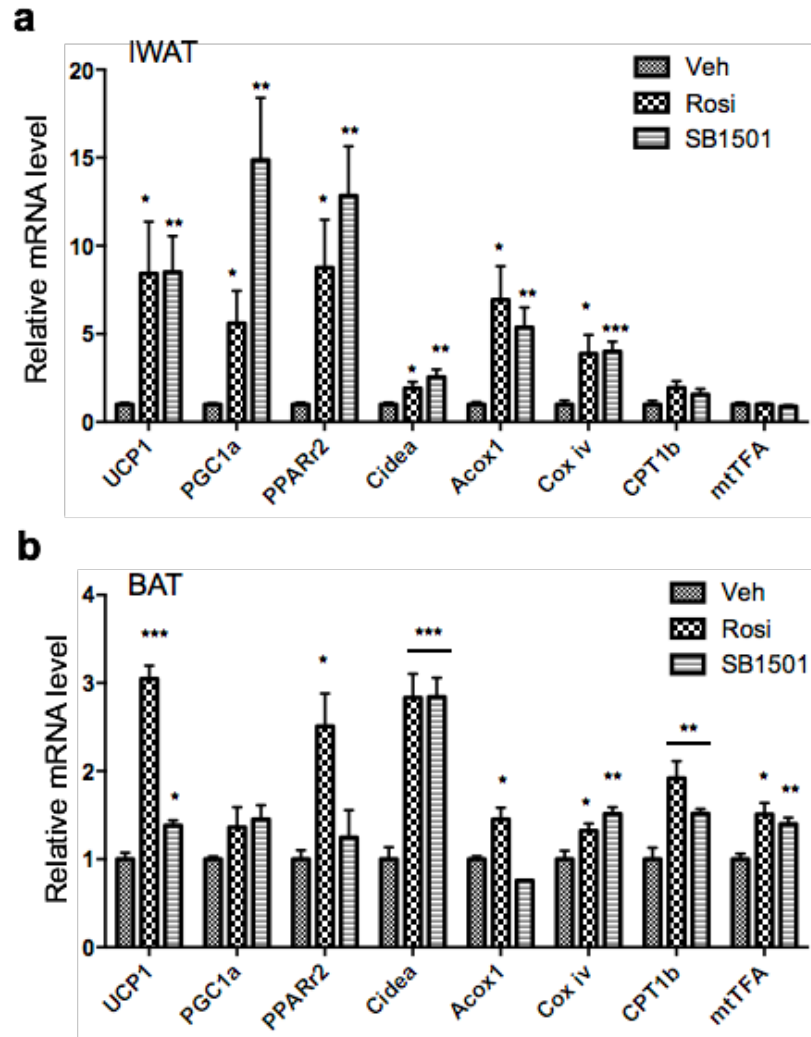


Figure 4.12. Quantitative real-time PCR analysis of gene involved in browning of WAT, mitochondria biogenesis and fatty acid oxidation processes in IWAT and BAT.

Identification of potential target for SB1501 via TS-FITGE. Next, I aimed to elucidate the molecular target of SB1501. The commonly used approach for target identification (Target ID) includes the affinity chromatography-pull down assay, activity-based proteome profiling, and affinity-based proteome profiling [32, 33, 34]. In most cases, chemical modification of bioactive compounds is required to introduce functional handles for covalent cross-linking to target proteins. However, there were many failures in preparing target ID probes because even slight modifications may abolish the biological activity of original hit compounds [35]. For target ID of SB1501, I attempted to design a target ID probe which do not loss the bioactivity of SB1501. However, structure modification of SB1501 obliterated the bioactivity of SB1501, limiting the access to target ID probes. Therefore, there is a high demand for the label-free target ID method without any structural modification in SB1501.

Recently, a label-free target identification method using thermal stability shift-based fluorescence difference in two-dimensional gel electrophoresis (TS-FITGE) is reported. TS-FITGE is based on cellular thermal stability assay (CETSA), the engagement of bioactive ligands stabilizes or destabilizes target proteins against heat denaturation and changed the melting temperature (T_m) of the target protein [37]. However, CETSA is applicable for biased candidate proteins using designated immunoblot analysis, thereby we applied thermal stability shift to our FITGE technique [38]. After treatment of vehicle of SB1501 into cells, cells were heated at a range

of temperatures to induce thermal denaturation. Target protein of SB1501 will show shifted thermal stability and show different amounts in the soluble fraction in whole proteome. Next, vehicle-treated group and SB1501-treated group are labeled with Cy3-NHS and Cy5-NHS respectively, and mixed and separated by 2D-gel electrophoresis. Quantitative 2D gel image analysis of each protein spot revealed target proteins with shifted thermal stability by drug engagement, and excised for identification by mass spectrometry.

In-gel fluorescence scanning of 2D gels revealed characteristic spots at 56 kDa and 70 kDa approximately. I excised the spots from 2D gels, and performed MS/MS analysis. After MS/MS analysis, I would obtain a list of proteins detected from each spot, and selected potential candidates for target proteins that were repeatedly identified (Figure 4.13).

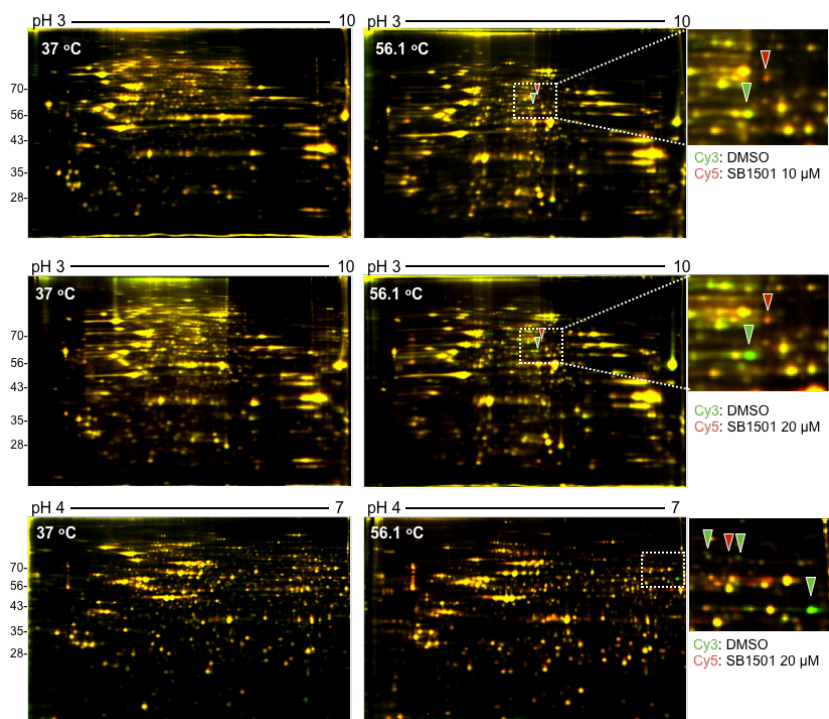


Figure 4.13. Target identification of SB1501 with TS-FITGE technology. Merged image of TS-FITGE in the absence (Cy3) and presence (Cy5) of SB1501 (10 μ M or 20 μ M). In the extended image of indicated box in the whole gel image of 56.1 $^{\circ}$ C, we identified protein spots showing thermal stability shift by SB1501 in Hela cell line. Green arrows indicate the spots which are destabilized by SB1501 engagement. Red arrows indicate the spots which are stabilized by SB1501 engagement.

4.4. Conclusion

In this study, I discovered new small molecule SB1501 that has novel therapeutic potential to treat obesity and obesity-related metabolic disorder. Initially, I discovered SB1501 from the unbiased image-based phenotypic screening by monitoring cellular lipid droplets with a hypothesis that size and quantity of LDs are crucial for the measurement of adiposity in adipocytes. Also, I figured out that SB1501 decreases fat accumulation by inducing PGC-1 α regulatory cellular processes involving adaptive thermogenesis, mitochondria biogenesis and fatty acid oxidation in 3T3-L1 adipocytes. Notably, SB1501 reduced glycerol release and gene expression of resistin, whereas gene expression of adiponectin was increase.

From these data, I convinced that SB1501 treatment has novel therapeutic potential for combating obesity and obesity-associated insulin resistance. Therefore, I administrated SB1501 into obese-induced *db/db in vivo* mice model. *In vivo* administration of SB1501 evidently reduced the size of adipocytes in adipose tissue, the body weight, and fat mass after the administration of 10 mpk SB1501 for 4 weeks. Not only SB1501 decreased obesity, also improved glucose tolerance as determined by glucose tolerance tests (GTTs). Consistent with *in vitro* data, SB1501 also increased PGC-1 α and PGC-1 α regulated UCP-1 expression in IWAT and BAT. Moreover, profiles of mRNA expression revealed that thermogenic

capacity, mitochondria biogenesis and fatty acid oxidation are upregulated in SB1501-administrated mice. Together, I concluded that SB1501 reduces the body weight and fat mass by increasing energy expenditure of adipose tissues and activate the thermogenic program, thereby improving insulin sensitivity *in vivo*. In light of high demands for a new class of therapeutic agents for combating obesity and obesity-associated metabolic disorders, SB1501 would be a powerful resource for the development of first-in-class anti-obesity drug.

4.5. References

1. S. E. Kahn, R. L. Hull and K. M. Utzschneider, *Nature* 2006, **444**, 840–846.
2. P. G. Kopelman, *Med. Int.* 1994, **22**, 385–388.
3. A. J. Walley, A. I. F. Blakemore and P. Froguel, *Hum. Mol. Genet.* 2006, **15**, R124–R130.
4. P. J. Brantley, V. H. Myers and H. J. Roy, *J. La. State. Med. Soc.* 2005, **1**, S19–S27
5. Y. H, Tseng, A. M. Cypess and C. R. Kahn, *Nat. Rev. Drug Discov.* 2010, **9**, 465–482.
6. J. K. Sethi and A. J. Vidal-Puig, *J. Lipid. Res.* 2007, **48**, 1253-1262.

7. A. Guilherme, J. V. Virbasius, V. Puri and M.P. Czech, *Nat. Rev. Mol. Cell Biol.* 2008, **9**, 367–77.
8. N. C. Chavez-Tapia, N. Rosso and C. Tiribelli, *BMC Gastroenterol.* 2012, **12**, 20.
9. N. Musi and R. Guardado-Mendoza, *Cell. Endocrinol. Heal. Dis.* 2014, **89**, 229–237.
10. N. Ouchi, J. L. Parker, J.J. Lugus and K. Walsh, *Nat. Rev. Immunol.* 2011, **11**, 85–97.
11. R. Gómez, J. Conde, J. J. Gómez Reino, F. Lago and O. Gualillo, *Reumatol. Clin.* 2009, **5**, 6–12.
12. A. Jo, J. Jung, E. Kim and S.B. Park, *Chem. Commun.* 2016, **52**, 7433–7445.
13. M. Koh, J. Park, J. Y. Koo, D. Lim, M. Y. Cha, A. Jo, J. H. Choi and S. B. Park, *Angew. Chem., Int. Ed.* 2014, **53**, 5102–5106.
14. S. Lee, Y. Nam, J. Y. Koo, D. Lim, J. Park, J. Ock, K. Suk and S. B. Park, *Nat. Chem. Biol.* 2014, **10**, 1055–1060.
15. A. Martinsson, *Pol. Arch. Med. Wewn.* 1969, **42**, 481–486.
16. S. Lee, E. Kim and S. B. Park, *Chem. Sci.* 2013, **4**, 3282–3287.
17. A. R. Thiam, R. V. Farese and T. C. Walther, *Nat. Rev. Mol. Cell Biol.* 2013, **14**, 775–86.
18. H. Yang, A. Galea, V. Sytnyk and M. Crossley, *Curr. Opin. Cell Biol.* 2012, **24**, 509–16.
19. E. D. Rosen and O. A. MacDougald, *Mol. Cell. Biol.* 2006, **7**, 885–896.
20. ME Patti and S. Corvera, *Endocr. Rev.* 2010, **31**, 364–395.
21. E. E. Blaak, D. P. C. van Aggel-Leijssen, A. J. M. Wagenmakers, W. H. M. Saris and M.A. van Baak, *Diabetes*, 2000, **49**, 2102–2107.
22. H. Zong et al., *Proc. Natl. Acad. Sci. USA.* 2002, **99**, 15983–15987.
23. B. N. Finck and D. P. Kelly, *J. Clin. Invest.* 2006, **116**, 615–622.
24. P. Fernandez-Marcos and J. Auwerx, *Am. J. Clin.* 2011, **93**, 884–890.

25. J. Lin, C. Handschin and B. M. Spiegelman, *Cell. Metab.* 2005, **1**, 361–370.
26. P. Pulserver, Z. Wu, C. W. Park, R. Graves, M. Wright and B. M. Spiegelman, *Cell* 1998, **92**, 829-839.
27. D. G. Nicholls, *Biochim. Biophys. Acta.* 2006, **1757**, 459–466.
28. M. Harms and P. Seale, *Nat. Med.* 2013, **19**, 1252–1263.
29. P. Seale et al., *Nature* 2008, **454**, 961–967.
30. P. Seale et al., *J. Clin. Invest.* 2011, **121**, 96–105.
31. V. Peirce, S. Carobbio and A. Vidal-Puig, *Nature* 2014, 510, 76–83.
32. S. Pan, H. Zhang, C. Wang, S. C. Yao and S. Q. Yao, *Nat. Prod. Rep.* 2016, **33**, 612–620.
33. M. Schenone, V. Dancik, B. K. Wagner and P. A. Clemons, *Nat. Chem. Biol.* 2013, **9**, 232–240.
34. G. M. Simon, M. J. Niphakis and B. F. Cravatt, *Nat. Chem. Biol.* 2013, **9**, 200–205.
35. U. Rix and G. Superti-Furga, *Nat. Chem. Biol.* 2009, **5**, 616– 624.
36. H. Park, J. Ha, J. Y. Koo, J. Park and S. B. Park, *Chem. Sci.* 2017, **8**, 1127-1133.
37. D. Martinez Molina and P. Nordlund, *Annu. Rev. Pharmacol.* 2016, **56**, 141–161.
38. J. Park, S. Oh and S. B. Park, *Angew. Chem., Int. Ed.* 2012, **51**, 5447–5451.

Conclusion

As the life expectancy of human has been extended, it has become an important issue to achieve high quality of life. Along with these changes, the metabolic syndrome has become a major health problem in worldwide as it is more and more common in adults with increase in westernized life style, excessive energy supply and obesity. Although it is possible to prevent the progress of metabolic syndrome and its clinical complications by controlling life style, medication is also required to control risk factors such as hyperglycemia, hypertension and dyslipidemia. Among the many risk factors, hyperglycemia and obesity are the crucial factors for the pathogenesis of metabolic syndrome. Recent findings revealed that hyperglycemia and obesity are causally linked with insulin resistance, and they aggravate metabolic syndrome. In particular, obesity causes increase in pro-inflammatory state and systematic metabolic disorders. Therefore, there is a large demand for the development of therapeutic agents to manage obesity and hyperglycemia.

However, as the case of other metabolic diseases, development of obesity and hyperglycemia is a consequence of interplay between multiple metabolic parameters, and there's no unifying therapeutic target. Therefore, target-based approach has as indispensable challenge in terms of determining target protein among the multiple potential therapeutic targets

which are regulating energy metabolism. In this regard, I propose the phenotype-based approach to discover novel bioactive small molecules for combating hyperglycemia and obesity.

In this study, I explore the possibility of phenotypic screening as a promising approach to identify anti-diabetic and anti-obesity agents. To establish phenotypic screenings, I focus on the metabolic phenotypes which are representing the amelioration of pathophysiological condition of hyperglycemia and obesity. After the decision of metabolic phenotypes, I constructed and performed image-based high-throughput screening (HTS) in cellular systems using fluorescence bioprobes.

In chapter 2, image-based high-throughput screening (HTS) to discover novel anti-diabetic compounds was proposed using fluorescence glucose bioprobe (GB2-Cy3) for monitoring cellular glucose uptake. First of all, I explored the biophysical properties of the GB2-Cy3. Based on the understanding of biophysical properties of GB2-Cy3, I figured out that GB2-Cy3 is released after its cellular uptake resulting inaccurate measurement of glucose uptake. To avoid this phenomenon, I introduced specific GLUT4 inhibitor, phloretin, to the assay system for achievement of robustness and accuracy of screening. As a result, I successfully constructed the first image-based HTS to monitor the glucose uptake in living cells. From the practical screening of small molecule library, I discovered the new glucose uptake enhancers. In addition, I also

demonstrated the *in vivo* applicability of GB2-Cy3 for monitoring the efficacy of anti-diabetic compounds in zebra fish larvae system. Taken together, I suggest that phenotypic screening for monitoring glucose uptake would be an efficient approach to discover new bioactive compounds which have anti-diabetic potential.

In chapter 3, I developed image-based high-content screening (HCS) for monitoring dynamic GLUT4 trafficking in living cells. I developed real-time and quantitative assay system, EGFP-GLUT4-SNAP, based on the genetically encoded SNAP tag and EGFP into GLUT4. This novel assay system enabled the determination of the quantity and kinetics of GLUT4 trafficking within cellular system. By expending this assay system into HCS platform, I could reveal the regulation of intracellular distribution of GLUT4 after the treatment of anti-diabetic agent (rosiglitazone) or insulin. I anticipate that this approach allows us to understand the cellular GLUT4 trafficking, and to study mechanism-of-action of anti-diabetic agents which increase cellular glucose uptake by regulating GLUT4 trafficking.

In chapter 4, I describe the discovery of novel anti-obesity small molecule from the phenotype-based approach. In obesity, excess amounts of fats are stored in adipose tissue resulting hypertrophy of adipocytes. Therefore, I hypothesized that amount of cellular lipid droplets (LDs) is a metabolic phenotype of obesity as the size of white adipocytes is

determined by large and unilocular LDs. From this point of view, I performed an image-based high-throughput screening (HTS) in cellular system using fluorescence LD bioprobe (SF44) to identify small molecules which reduce cellular LDs. As a result, I discovered a new bioactive compound, SB1501, that reduces LDs in adipocyte cells. In addition, I could demonstrate the therapeutic potential of SB1501 by finding out *in vivo* efficacy of SB1501 including body weight reduction, fat mass reduction and amelioration of insulin resistance. Thus, I suggest that phenotypic screening for monitoring cellular LDs would be an efficient approach to discover new bioactive compounds which have anti-obesity potential.

In conclusion, I suggest that phenotypic screening is a promising approach to discover new bioactive small molecules. Although this dissertation focused on the metabolic disease, phenotype-based approach will be very useful when it is applied to diseases in which the therapeutic target is not thoroughly defined. Therefore, I anticipate that this approach will shed light on the medicinal field.

국문초록

표현형 기반 접근을 통한 생리활성 저분자 화합물의 발굴 및 이를 이용한 대사성질환에 관한 연구

조아라

서울대학교 자연과학대학원 화학부

표현형 기반 접근법을 통해 생리활성 저분자 화합물을 발굴하는 연구가 각광을 받고 있다. 전통적인 표적 기반 접근법에서는 질병의 발생과 관련된 분자적 메카니즘에 대한 이해에 기반하여 설정한 특정 단백질의 기능을 조절하는 것에 초점을 맞추고 있으나, 표현형 기반 접근법은 세포나 개체에서 일어나는 표현형에 주목함으로써 복잡한 세포 신호전달계의 상호작용의 최종적 결과를 관찰한다. 표적 기반 접근법에 비해 표현형 기반 접근법이 지니는 주요한 강점은 질병의 조절에 대한 기능이 아직까지 밝혀지지 않은 특정 질병들에 대한

새로운 생물학적 표적 단백질을 발굴할 수 있는 잠재력을 갖는다는 것이다. 이러한 맥락에서, 표현형 기반 접근법은 뚜렷한 발병 원인이 밝혀지지 않은 질병에 적용되었을 때 매우 큰 효용을 보일 것이라고 생각할 수 있다. 따라서 본 논문에서는 표현형 기반 접근법을 체계적으로 도입하여 통해 대사성질환의 신규 생리활성 저분자 화합물을 발굴하는 연구에 대하여 논하고자 한다.

첫 번째 장에서는 본 논문의 연구 배경과 연구 목적에 관하여 기술하였다. 두 번째 장에서는 고혈당과 제 2 형 당뇨병을 개선할 수 있는 새로운 생리활성 저분자 화합물을 발굴하기 위하여 세포의 포도당 흡수를 관찰할 수 있는 표현형 기반 스크리닝을 구축한 연구에 대하여 논하였다. 본 연구에서는 형광 포도당 프로브 (GB2-Cy3)를 활용하여 이미징 기반의 고효율 스크리닝을 구축하였다. 그리고 저분자 화합물 라이브러리에 대한 스크리닝으로부터 항 당뇨병 물질로서의 가능성을 갖는 새로운 포도당 흡수 촉진 화합물을 발굴할 수 있었다. 또한 형광 포도당 프로브의 전하적 성질이 GLUT-선택적 세포 흡수에 미치는 영향을 미친다는 것을 입증하였다. 마지막으로 GB2-Cy3 가 세포 뿐만 아니라 제브라피쉬 (zebrafish larvae) 동물 모델 시스템에도 적용될 수 있음을 입증하였다. 이러한 동물 수준의 이미징 시스템은 추후 생리활성 물질의 활성을 검증하는 연구에 유용한 수단이 될 것이라고 기대된다. 세 번째 장에서는

살아있는 세포에서 일어나는 GLUT4 의 역학적 이동을 관찰하기 위한 형광 이미징 기법에 대하여 서술하였다. 이를 위하여 유전자 재조합 기법을 활용해 EGFP-GLUT4-SNAP 이라는 새로운 이미징 시스템을 개발하였다. 이와 같은 새로운 이미징 시스템을 이용하여 살아있는 세포에서 일어나는 GLUT4 의 이동을 실시간으로 그리고 정량적으로 관찰할 수 있음을 증명하였다. 이러한 이미징 시스템은 세포 내에서 일어나는 GLUT4 의 조절 기전과 세포의 포도당 흡수를 촉진하는 생리활성 물질의 작용 기전을 이해하기 위한 연구들에 유용한 수단으로써 활용될 것으로 기대된다. 네 번째 장에서는 표현형 기반 접근법을 통해 항 비만 효과를 갖는 새로운 저분자 화합물을 발굴할 연구에 관하여 서술하였다. 본 연구에서는 세포의 지방 방울을 관찰할 수 있는 이미징 기반의 표현형 기반 스크리닝을 수행하였으며, 그 결과 지방 세포의 지방 방울을 감소시키는 SB1501 이라고 하는 새로운 저분자 화합물을 발굴하였다. 발굴한 저분자 화합물의 작용 기전을 연구한 결과 SB1501 이 PGC-1 α 단백질을 통해 세포의 미토콘드리아 발생, 지방산 산화 그리고 적응열발생 (adaptive thermogenesis)를 유도한다는 것을 밝혔다. 또한 SB1501 은 비만이 유도된 동물 모델에서 체중 감소, 지방 조직의 무게 감소 그리고 인슐린 저항성 개선과 같은 치료학적 가능성을 나타냈다. 결과적으로 본 연구를 통하여 표현형 기반 접근을 통해 비만과 비만에

기인한 인슐린 저항성을 개선할 수 있는 새로운 생리활성 저분자 화합물을 발굴할 수 있음을 입증하였다.

요약하면 본 연구는 1) 세포의 표현형을 관찰할 수 있는 형광 바이오프로브의 물성에 대한 탐색, 2) 형광 바이오프로브를 이용한 이미징 기반의 표현형 스크리닝 시스템 구축, 3) 저분자 화합물 라이브러리 스크리닝을 통한 새로운 생리활성 물질 발굴, 4) 발굴된 생리활성 물질의 작용 기전에 관한 연구로 구성되어 있다. 이러한 일련의 연구들을 통하여 표현형 기반의 접근법이 새로운 생리활성 저분자 물질을 발굴하기 위한 유용한 방법임을 제안하고자 한다. 본 연구는 대사성질환을 개선할 수 있는 생리활성 물질의 발굴에 중점을 두고 있다. 이는 대사성질환의 치료 표적이 뚜렷하게 규명되지 않았기 때문에 표현형 기반 접근법이 효과적으로 작용할 것이라고 기대할 수 있기 때문이다. 이와 같은 체계적인 표현형 기반 접근법은 대사성질환 뿐만 아니라 다양한 질병의 새로운 생리활성 물질을 발굴하는 연구에 활용될 것으로 기대된다.

핵심 용어: 화학생물학, 표현형 기반 접근법, 고효율 스크리닝, 고집적 스크리닝, 형광 바이오프로브, 형광 현미경 이미징, 표적 단백질 규명, 대사증후군, 고혈당, 제 2형 당뇨병, 비만

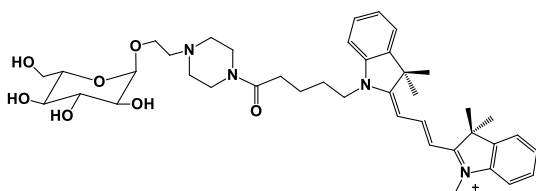
학번: 2011-20305

Appendix

Synthetic procedures and NMR spectra

1.1. L-GB2

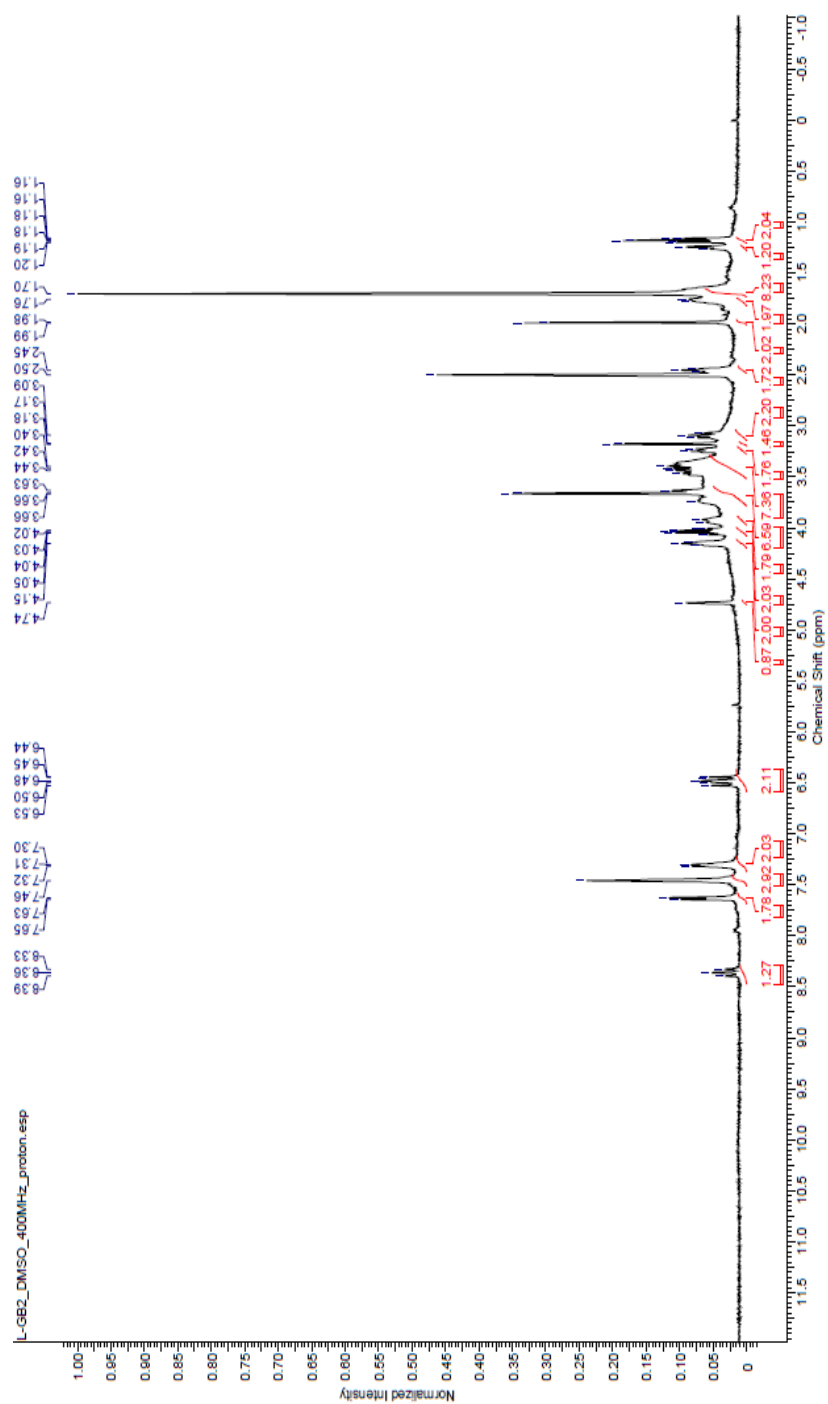
L-GB2 was prepared using the same procedure described in the previous report for GB2 synthesis [13 of chapter 2.5].



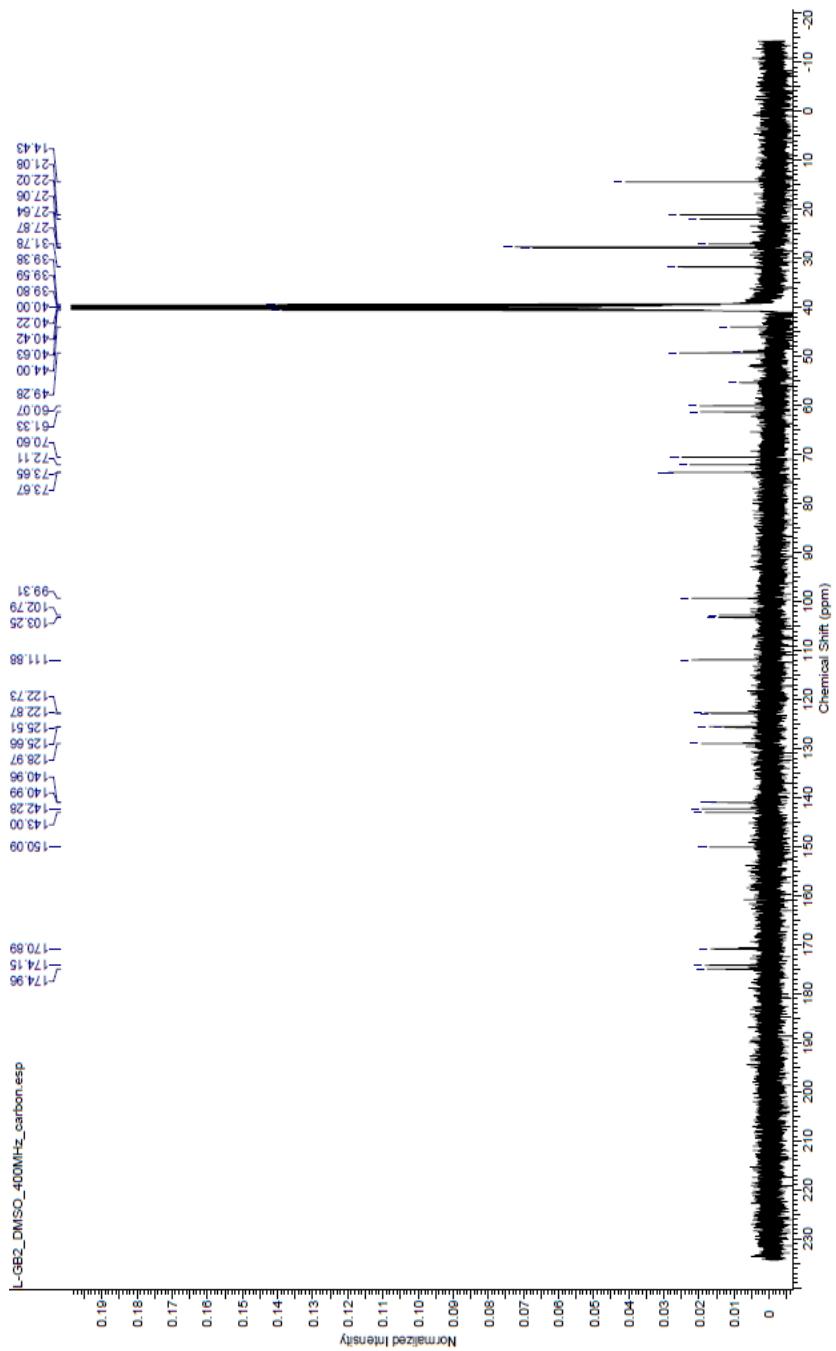
^1H NMR [400 MHz, $(\text{CD}_3)_2\text{SO}$] δ 8.39 (t, $J = 12$ Hz, 1H), 7.64 (d, $J = 12$ Hz, 2H), 7.46 (s, 3H), 7.32–

7.30 (m, 2H), 6.53–6.44 (m, 2H), 4.74 (s, 1H), 4.17–4.14 (m, 2H), 4.07–4.01 (m, 2H), 3.95–3.92 (m, 2H), 3.74–3.63 (m, 7H), 3.47–3.40 (m, 8H), 3.25–3.23 (m, 2H), 3.18 (d, $J = 4$ Hz, 2H), 3.09 (t, $J = 8$ Hz, 2H), 2.45 (m, 2H), 1.99 (d, $J = 4$ Hz, 2H), 1.77 (d, $J = 4$ Hz, 2H), 1.70 (s, 9H), 1.27–1.24 (m, 2H), 1.20–1.16 (m, 2H); ^{13}C NMR [100 MHz, $(\text{CD}_3)_2\text{SO}$] δ 174.96, 174.15, 170.89, 150.09, 143.00, 142.26, 140.99, 140.96, 128.97, 125.66, 125.51, 122.87, 122.73, 111.88, 111.84, 103.25, 102.79, 99.31, 73.67, 73.65, 72.11, 70.60, 61.33, 60.07, 55.38, 49.28, 49.25, 48.95, 44.00, 31.78, 27.87, 27.64, 27.06, 22.02, 21.08, 14.43; HRMS (FAB $^+$): calculated for $\text{C}_{41}\text{H}_{57}\text{N}_4\text{O}_7$ $[\text{M}]^+$: 717.4227; found : 717.4251.

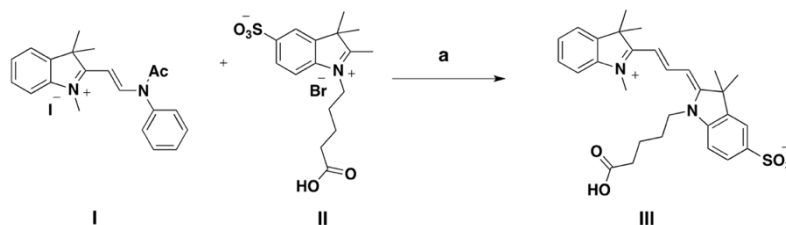
^1H NMR of L-GB2 (DMSO- d_6 , 400 MHz)



^{13}C NMR of L-GB2 (DMSO- d_6 , 100 MHz)

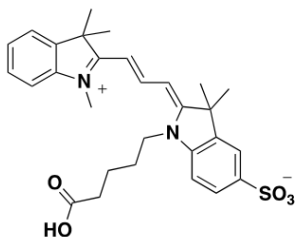


1.2. Synthesis of GB2-Cy3, GB2-Cy3-S1 and GB2-Cy3-S2



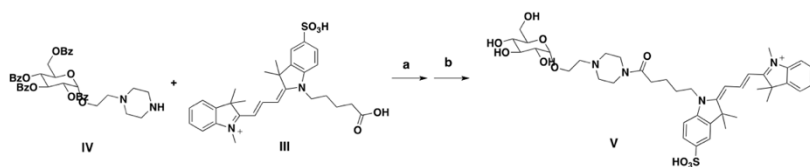
Scheme S1. Synthesis procedure of Cy3-S1. (a) pyridine, Ac₂O, 120 °C, 2h, 17%

Cy3-S1 (III), 2-((1E,3E)-3-(1-(4-carboxybutyl)-3,3-dimethyl-5-sulfoindolin-2-ylidene)prop-1-en-1-yl)-1,3,3-trimethyl-3H-indol-1-ium



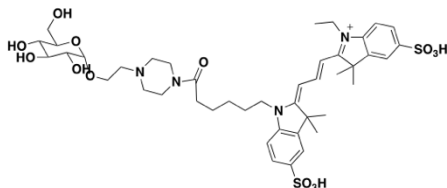
Intermediate I and II were synthesized as previously reported.^{1,2} Intermediate I (100 mg, 0.22 mmol) and intermediate II (94 mg, 0.22 mmol) were dissolved in pyridine (5 mL) and Ac₂O (5 mL). The reaction mixture was stirred at 120 °C for 2 h. The solvents were evaporated in vacuo, and remaining liquid was dissolved with brine and dichloromethane. The organic layer was separated and the aqueous layer was extracted three times with dichloromethane. The combined organic layer was dried over anhydrous Na₂SO₄(s) and filtered through a celite-packed glass filter. The filtrate was concentrated in vacuo and purified with HPLC to provide Cy3-S1, III (20 mg).

¹H-NMR (300 MHz, MeOD): δ 8.56 (t, J = 13.72 Hz, 1H), 7.98–7.83 (m, 2H), 7.61–7.53 (m, 1H), 7.51–7.29 (m, 4H), 6.56–6.39 (m, 2H), 4.22–4.10 (m, 2H), 3.76–3.69 (m, 3H), 3.68–3.60 (m, 1H), 2.49–2.36 (m, 2H), 1.78 (s, 6H), 1.77 (s, 6H), 1.29 (s, 3H); LRMS (ESI+) m/z calcd for C₂₉H₃₅N₂O₅S [M]⁺ : 523.23 Found : 523.08.



Scheme S2. Synthetic procedure of GB2-Cy3-S1. (a) TSTU, DIPEA, DMF, r.t., overnight; (b) NaOMe, MeOH, r.t., 3 h. 21% (two steps).

GB2-Cy3-S1 (V), 2-(((1E,3E)-3-(3,3-dimethyl-1-(5-oxo-5-(4-(2-(((2S,3R,4S,5S,6R)-3,4,5-trihydroxy-6-(hydroxymethyl)tetrahydro-2H-pyran-2-yl)oxy)ethyl)-piperazin-1-yl)pentyl)-5-sulfoindolin-2-ylidene)prop-1-en-1-yl)-1,3,3-trimethyl-3H-indol-1-ium



Intermediate VI was purchased from GE healthcare. Intermediate VI (7.5 mg, 0.011 mmol) were dissolved in DMF (1 mL). DIPEA (8.26 μ l, 0.044 mmol) and TSTU (5.36 mg, 0.017 mmol)

were added to the reaction mixture and stirred at room temperature for 1 h. Then, intermediated IV and was added to the reaction mixture and stirred at room temperature for overnight. The solvents were evaporated in vacuo, and remaining liquid was dissolved with methanol (400 μ l). Sodium methoxide (0.5 M solution in methanol, 100 μ l, 0.033 mmol) was added to the reaction mixture and stirred at room temperature for 2 h. The solvents were evaporated in vacuo, and remaining NaOMe was quenched with 2 N HCl. The remaining liquid was concentrated in vacuo and purified with HPLC to provide GB2-Cy3-S2, VII (4.8 mg).

¹H-NMR (500 MHz, D₂O): δ 8.48 (t, J = 13.45 Hz, 1H), 7.89 (d, J = 0.98 Hz, 2H), 7.83 (ddd, J = 8.31, 4.40, 1.47 Hz, 2H), 7.33 (t, J = 8.07 Hz, 2H), 6.35 (dd, J = 16.63, 13.69 Hz, 2H), 5.01 (d, J = 3.91 Hz, 1H), 4.14–4.01 (m, 6H), 3.92–3.83 (m, 3H), 3.81–3.70 (m, 3H), 3.69–3.60 (m, 3H), 3.59–3.41 (m, 5H), 2.43 (t, J = 7.34 Hz, 2H), 1.87–1.77 (m, 3H), 1.70 (s, 6H), 1.69 (s, 6H), 1.63–1.53 (m, 3H), 1.42–1.30 (m, 5H); LRMS (ESI+) m/z calcd for C₄₃H₆₁N₄O₁₃S₂ [M]⁺ : 905.37 Found : 905.43.